

# UC Santa Barbara

## UC Santa Barbara Electronic Theses and Dissertations

### Title

High Performance InP Photonic Integrated Circuits and Devices for Free Space Communications and Sensing

### Permalink

<https://escholarship.org/uc/item/1sx6502v>

### Author

Isaac, Brandon

### Publication Date

2020

Peer reviewed|Thesis/dissertation

UNIVERSITY OF CALIFORNIA

Santa Barbara

High Performance InP Photonic Integrated Circuits and Devices for Free Space  
Communications and Sensing

A dissertation submitted in partial satisfaction of the  
requirements for the degree Doctor of Philosophy  
in Materials

by

Brandon J. Isaac

Committee in charge:

Professor Larry Coldren, Co-Chair

Professor Jonathan Klamkin, Co-Chair

Professor John Bowers

Professor Art Gossard

March 2020

The dissertation of Brandon J. Isaac is approved.

---

Art Gossard

---

John Bowers

---

Jonathan Klamkin, Committee Co-Chair

---

Larry Coldren, Committee Co-Chair

December 2019

High Performance InP Photonic Integrated Circuits and Devices for Free Space  
Communications and Sensing

Copyright © 2019

by

Brandon J. Isaac

## ACKNOWLEDGEMENTS

Writing the acknowledgements is probably on par with the difficulty of listing out every experiment I tried in grad school. Quite simply, there are too many people to thank for teaching me life skills and useful/useless bits of knowledge, keeping me from making real mistakes, keeping me going, and generally making sure I didn't completely screw up the opportunities I've been afforded. But here I go...

First, my family deserves a big share of the credit. While they might not have been able to keep me in line all the time, or get me to pay attention in school, the foundation that was laid by them was much like the foundation you put down for a house. Without it, nothing can be done. But the house analogy seems rather boring, so let us use campfire instead. They know I have always enjoyed a good fire. For almost two decades, they laid the kindling to set me up for success and while something else provided the spark, I would have dwindled and become billowing cloud of smoke had the foundation not been laid right.

The spark came from senior high school physics under Mr. Ledden, and I have him to thank for starting me on this trajectory. I think this is also where I made my oldest friends Dave, Sam and Erinn. I can go a year without seeing you and still feel like nothing has changed. A fire doesn't last long on foundation alone though, and so the remainder of these acknowledgements will be on the fuel that kept me going.

In college, I stumbled upon the University of Kentucky Solar Car Team, where I met mentors and ruthlessly hard-working people that showed me that there was more to school than coursework. From this group I learned basic hands-on skills, better public speaking, and

people/crisis management skills. And there was the group that made up Tau Beta Pi and my chemical engineering class, and the overlap between the two inspired me, while sharing in the misery that was all aspects of chemical engineering. Between these different groups is where I learned the most about leadership. In particular, Dr. Walcott's leadership and mentoring of students was something to aspire to. And the Leadership class taught by Dr. Lester, with help from Karen and Stan Pigman, and our trip to DC was an experience I will never forget. I also must thank my research mentors, specifically, Raghu and the group that made up Dr. Seo's lab that gave me the opportunity to learn experimental research as an undergrad.

In graduate school my first line of defense was Apt. 1217 and its extension (you know who you are). Between the excitement of our first year, the nightmare of device physics, and way too much FIFA we somehow all made it through. I still think Nathan's banging synthetic rocks together, and Jon's just plotting quartic expressions and making stuff up about stable phonon modes.

While I only spent two years with the Stemmer group, they provided guidance and entertainment. The senior students instilled upon me the importance of understanding the tools the institution provided, and not just pushing the buttons to get my result. And for getting me to wear a helmet when I ride a bike.... Oh, and for letting me stay in the group chat and crash the semi-monthly trip to Flavor of India. And the memories that made up Tallahassee.

Next, I move onto the fuel that got me this degree. What I refer to as the UCSB photonics family tree. Jonathan was advisor I hoped for, giving me the freedom and creativity to solve the problems I encountered, while being present for advice and feedback. And of course, for his patience throughout the process. I was once told that you take on much of your

advisors “research personality” in the future, and considering that, my other committee members: Jon Bowers, Art Gossard, and Larry Coldren deserve thanks for instilling their values and research personalities on Jonathan while he was a student here at UCSB. It was a one-of-a-kind experience working under the guidance and support of them. I learned a small fraction of the knowledge they collectively contain, and yet felt that these four years could not have been better spent. In addition to the committee, the research support I received from the Nanofab team was unrivaled. Without the staff working tirelessly and providing guidance on fabrication most of this work would not have gotten past the simulation stages. This also include Matt Mitos, as he gave many of the Klamkin group students a fighting chance at making of devices that work.

The Klamkin group was made up of a strange mix of characters ranging from all over the world, and it made for an awesome experience. Between the BBQs that Bowen hosted, hiking with Joe, or just bickering during coffee breaks, I could have enjoyed this experience for much longer, but the part of me saying 6 years is long enough won that battle. Sergio deserves a special thanks for the providing the most guidance in making sure my measurements were done properly. With some of his old Italian proverbs sprinkled in, Fabrizio singing in the background, and Joe’s heckling, it made measuring hundreds of IV curves almost pleasant. To my office mates, including the first one Yuan and Fabrizio, and to ones I was with much longer, Takako, Victoria, Joe, Yujie, Fengqiao, Steven and Simone, thanks for putting up with my quirky personality and embracing the cat culture in our office. Between the cat photos and Takako’s googly eyes that she hid on people’s stuff, it was a nice change from the sterile hallways of ESB.

A special thanks goes to the hilarious, fun, and hard-working group that puts on the Beyond Academia conference each year. Working alongside everyone was a particularly rewarding experience. Between David, Lana, Shawn, and Robert, I'm not sure I have ever had such hilarious and yet productive meetings. There are too many other people that I have had the pleasure of meeting during my Ph.D. and I cannot do them all justice. But outside of research was a host of other experiences with people that made this journey more than I imagined when I purchased my one-way flight to SBA. To my Taekwondo class, yoga instructors, cat shelter volunteers, and the random friends I made in Osaka, Santa Fe, OFC, and many other places.

Sometimes in grad school it feels like there is nothing besides the challenges of research that is yours and everyone else's life. But outside of grad school, there is a host of other challenges that we are all facing. I must give a special thanks to David, Dave, and Simone for helping me through perhaps the most challenging parts of the last 6 years. The last year and a half would have been extremely difficult without your moral support, weekend trips to DC, or just hysterical rock band sessions.

I mentioned my family as laying the kindling and foundation that helped me succeed, but all the while they were behind the scenes fueling me with their support. I am especially thankful for their acceptance of all the ways each member sticks out and stands out, and for providing a place I could always escape to when I needed a break. To our little balls of fur that provides us relief from stress and anxiety. And finally, to my three nephews who are probably the only people that can make me laugh and smile regardless of what's going on elsewhere... even if you're trying to run away from me.

VITA OF Brandon J. Isaac  
December 2019

**Education**

- Ph.D. Materials**, University of California Santa Barbara December 2019  
Emphasis: Photonic materials and devices  
GPA: 3.57
- B.S. Chemical Engineering and Physics**, University of Kentucky May 2013  
GPA: 3.89

**PROFESSIONAL EMPLOYMENT**

***Dow Corning Corp.***

*Silane Process Engineering Intern* May 2013 to August 2013

- Performed analysis on chemical detector for limitations in detecting trace carbon impurities in industrial manufacturing of silicon compounds
- Completed solubility study on novel silicon chemical vapor deposition precursor for alternatives synthesis routes

*Solar Applications Intern* May 2012 to August 2012

- Developed method for characterizing rheological properties of materials and understanding the material's recovery after high shear
- Performed a designed experiment to analyze the effects of additives and the pre-processing of substrates on the properties of silicone materials for solar applications
- Created in-depth reports for studies performed on rheology of silicone products and the evaluation of additives on solar application materials

**Awards**

- NSF Graduate Research Fellowship 2015
- National Defense Science and Engineering Graduate Fellowship 2015

**PUBLICATIONS**

1. J. G. Connell, **B. J. Isaac**, G. B. Ekanayake, D. R. Strachan, and S. S. A. Seo, "Preparation of atomically flat SrTiO<sub>3</sub> surfaces using a deionized-water leaching and thermal annealing procedure," *Appl. Phys. Lett.*, vol. 101, no. 25, pp. 98–101, 2012.

2. J. Y. Zhang, J. Hwang, **B. J. Isaac**, and S. Stemmer, “Variable-angle high-angle annular dark-field imaging: Application to three-dimensional dopant atom profiling,” *Sci. Rep.*, vol. 5, 2015.
3. E. Mikheev, C. R. Freeze, **B. J. Isaac**, T. A. Cain, and S. Stemmer, “Separation of transport lifetimes in SrTiO<sub>3</sub>-based two-dimensional electron liquids,” *Phys. Rev. B - Condens. Matter Mater. Phys.*, vol. 91, no. 16, pp. 1–6, 2015.
4. R. F. Need, **B. J. Isaac**, B. J. Kirby, J. A. Borchers, S. Stemmer, and S. D. Wilson, “Interface-Driven Ferromagnetism within the Quantum Wells of a Rare Earth Titanate Superlattice,” *Phys. Rev. Lett.*, vol. 117, no. 3, 2016.
5. Y. Liu, A. Wichman, **B. Isaac**, J. Kalkavage, E. Adles, and J. Klamkin, “Ring Resonator Delay Elements for Integrated Optical Beamforming Networks: Group Delay Ripple Analysis,” *Adv. Photonics Congr.*, p. IW1B.3, 2016.
6. Y. Liu, A. Wichman, **B. Isaac**, J. Kalkavage, E. Adlest, T. Clark, J. Klamkin, “Single ring resonator delays for integrated optical beam forming networks,” in 2016 IEEE International Topical Meeting on Microwave Photonics, 2016.
7. Y. Liu, A. Wichman, **B. Isaac**, J. Kalkavage, E. Adlest, T. Clark, J. Klamkin, “Tuning Optimization of Ring Resonator Delays for Integrated Optical Beam Forming Networks,” *J. Light. Technol.*, vol. 35, no. 22, 2017.
8. H. Zhao, S. Pinna, B. Song, S. T. S. Brunelli, **B. Isaac**, F. Sang, L. Coldren, J. Klamkin, “Widely Tunable Integrated Laser Transmitter for Free Space Optical Communications,” in *Conference Digest - IEEE International Semiconductor Laser Conference*, 2018, vol. 2018-Septe.
9. J. Klamkin, Y. Liu, B. Song, F. Sang, and **B. Isaac**, “Integrated microwave photonic component technologies,” in *CLEO*, 2018, vol. Part F92-C.
10. Y. Liu, **B. Isaac**, J. Kalkavage, E. J. Adles, T. R. Clark, and J. Klamkin, “Low-loss silicon nitride integrated optical beamforming network for wideband communication,” *Proceeding SPIE*, vol. 1053118, no. February 2018, p. 44, 2018.
11. Y. Liu, A. Wichman, **B. Isaac**, J. Kalkavage, E. Adlest, T. Clark, J. Klamkin, “Ultra-Low-Loss Silicon Nitride Optical Beamforming Network for Wideband Wireless Applications,” *IEEE J. Sel. Top. Quantum Electron.*, vol. 24, no. 4, 2018.
12. Y. Liu, F. Sang, **B. Isaac**, J. Kalkavage, E. Adlest, T. Clark, J. Klamkin, “Integrated silicon nitride optical beamforming networks for wideband communications,” *Adv. Photonics Congr.*, pp. 3–4, 2018.

13. J. Klamkin, H. Zhao, B. Song, Y. Liu, **B. Isaac**, S. Pinna, F. Sang, L. Coldren, “Indium Phosphide Photonic Integrated Circuits: Technology and Applications,” in *2018 IEEE BiCMOS and Compound Semiconductor Integrated Circuits and Technology Symposium, BCICTS 2018*, 2018.
14. L. Megalini, S. T. Brunelli, W. O. Charles, A. Taylor, **B. Isaac**, J. E. Bowers, J. Klamkin, “Strain-compensated InGaAsP superlattices for defect reduction of InP grown on exact-oriented (001) patterned Si substrates by metal organic chemical vapor deposition,” *Materials (Basel)*, vol. 9, no. 3, 2018.
15. **B. Isaac**, B. Song, S. Pinna, S. Arafin, L. Coldren, and J. Klamkin, “Indium Phosphide Photonic Integrated Circuit Transmitter with Integrated Linewidth Narrowing for Laser Communications and Sensing,” *Conf. Dig. - IEEE Int. Semicond. Laser Conf.*, vol. 2018-September, no. November, pp. 53–54, 2018.
16. R. F. Need, **B. J. Isaac**, B. J. Kirby, J. A. Borchers, S. Stemmer, and S. D. Wilson, “Octahedral tilt independent magnetism in confined GdTio<sub>3</sub> films,” *Appl. Phys. Lett.*, vol. 112, no. 13, pp. 1–6, 2018.
17. **B. J. Isaac**, B. Song, S. Pinna, L. A. Coldren, and J. Klamkin, “Indium Phosphide Photonic Integrated Circuit Transceiver for FMCW LiDAR,” *IEEE J. Sel. Top. Quantum Electron.*, vol. 25, no. 6, 2019.
18. Y. Liu, **B. Isaac**, J. Kalkavage, E. Adles, T. Clark, and J. Klamkin, “93-GHz Signal Beam Steering with True Time Delayed Integrated Optical Beamforming Network,” in *2019 Optical Fiber Communications Conference and Exhibition, OFC 2019 - Proceedings*, 2019.
19. **B. Isaac**, S. Pinna, Y. Liu, and J. Klamkin, “Efficiency of Waveguide Uni-Traveling-Carrier Photodiodes for Microwave Signal Generation,” in *2019 Optical Fiber Communications Conference and Exhibition, OFC 2019 - Proceedings*, 2019.

## ABSTRACT

### High Performance InP Photonic Integrated Circuits and Devices for Free Space Communications and Sensing

by

Brandon J. Isaac

Communication needs have grown tremendously over the past few decades and will continue to increase in the future. In order to address these needs, 5G mobile communication systems are moving towards higher carrier frequencies in the millimeter wave (mmW) regime (30 – 300 GHz). Unlike traditional microwave frequencies, which have a relatively isotropic radiation pattern, the highly directional free space propagation characteristics of mmWs requires beamsteering and tracking between transmitters and receivers. One technology that is promising for future mobile communication systems is optical beam forming networks (OBFN). This technology uses photonic components to provide wide bandwidth and eliminate beam squint associated with RF methods to drive phased array antennas. The optical signals from the OBFN are down-converted using high speed photodiodes, which require high bandwidth, efficiency and RF output power. Here we present results on waveguide uni-traveling-carrier photodiodes integrated with mode converters for efficient coupling to a silicon nitride OBFN photonic integrated circuit (PIC). We demonstrate greater than 67 GHz

bandwidth and extract efficiency limitations due to the space charge effect of the high carrier density under large optical input power.

In addition to communication, highly directional beams can be used for free space sensors including LIDAR. While various frequency ranges provide benefits for specific applications, by increasing the frequency from the mmW regime to the near infrared ( $\sim 193$  THz), beam size can be further reduced to provide high resolution imaging and sensing. We present an indium phosphide transceiver PIC that incorporates a tunable laser, frequency discriminator, and receiver that can be used for frequency modulated continuous wave (FMCW) LIDAR when integrated with an optical phased array for 2D beamsteering. The transceiver provides wavelength tuning over 40 nm, a method for stabilizing the lasing frequency and imparting frequency modulation, and a balanced receiver for coherent detection. The components of the PIC will be discussed along with experimental verification of the functionality of this transceiver.

# Contents

<b>1. Introduction.....</b>	<b>1</b>
References.....	8
<b>2. Photonic Generation of Millimeter Waves and Optical     Beam Forming Networks for Phased Array Antennas.....</b>	<b>9</b>
2.1. mmW for OBFN.....	12
References.....	15
<b>3. Operating Principles of Frequency Modulated     Continuous Wave LIDAR.....</b>	<b>18</b>
3.1. Transmitter .....	21
3.2. Receiver.....	25
References.....	26
<b>4. Photodiode Device Fundamentals, Design, and Fabrication.....</b>	<b>30</b>
4.1. PN-Junctions.....	31
4.1.1. Forward Bias Operation .....	33
4.1.2. Reverse Bias Operation.....	34
4.2. Uni-Traveling Carrier Photodiodes for mmW Generation.....	34
4.2.1. Device Overview .....	34
4.2.2. Frequency response .....	37
4.2.3. RF Output Power.....	39
4.2.4. Efficiency .....	40
4.3. Challenges of monolithic integration .....	44
4.3.1. Passive Waveguide Design .....	46
4.3.2. Active Photodiode Waveguide Design .....	49
4.3.3. Passive to Active Transition Design .....	50
4.3.4. Electrical Design .....	53
4.4. Fabrication of InP/InGaAsP Devices .....	54
4.4.1. Overview .....	55
4.4.1.1. Masking.....	55
4.4.1.2. Wet Etching.....	60
4.4.1.3. Dry Etching .....	62
4.4.1.4. Metallization and lift-off .....	63

4.5. Photodiode Fabrication.....	64
4.5.1.Active Region Definition .....	64
4.5.2.Passive Waveguide Etch .....	65
4.5.3.Regrowth .....	65
4.5.4.Mode Converter Formation.....	66
4.5.5.N and P Contact Formation.....	66
4.5.6.BCB Encapsulation .....	71
4.5.7.Pad Metal Deposition .....	73
References.....	74
<b>5. Experimental Results on Uni-traveling Carrier Photodiode.....</b>	<b>79</b>
5.1. First Generation .....	79
5.2. Second Generation.....	82
5.3. Third generation .....	87
5.4. Conclusion.....	90
References.....	90
<b>6. Photonic Integrated Circuit Components and Fabrication.....</b>	<b>91</b>
6.1. Photonic Integrated Circuit for FMCW LIDAR .....	91
6.1.1.SGDBR Laser.....	91
6.2. PIC Transceiver Fabrication.....	92
6.2.1.Active/Passive Definition.....	92
6.2.2.Grating.....	93
6.2.3.Regrowth .....	93
6.2.4.Waveguide Definition .....	94
6.2.5.Semi-Self-Align Process .....	98
6.2.6.Pad Metal Deposition and PIC Singulation.....	100
References.....	102
<b>7. Experimental Results on Transceiver PIC for LIDAR.....</b>	<b>104</b>
7.1. SGDBR Laser Performance .....	104
7.2. Frequency Discriminator Response.....	106
7.3. Receiver.....	107
7.4. Conclusion.....	109
References.....	109
<b>8. Conclusion and Future Works .....</b>	<b>110</b>
8.1. Waveguide Uni-Traveling-Carrier Photodiode .....	110

8.1.1.Summary of Accomplishments .....	110
8.1.2.Future Works.....	112
8.2. InP PIC Transceiver. ....	113
8.2.1.Summary of Accomplishments .....	113
8.2.2.Future Works.....	114
References.....	114

# Chapter 1

## Introduction

The field of photonics has been driven strongly by the need for faster digital communications[1], [2]. Fiber optics, which became the back bone of the communication network in the early 1980s, has contributed to the growth of semiconductor laser and optoelectronics development for the last 3 decades. Figure 1 - 1 shows the data demands over the last few decades and expected growth in the near future. This has led to compact, stable, and tunable laser sources, integrated optical transceivers, and high-speed optical detectors and modulators to allow the increasing demand to be met. While fiber optic technology was initially used for long haul data transmission, the fiber back bone has become increasingly prevalent in shorter reaching networks. Nevertheless, alternative technologies such as coaxial or free-space are used for the short-range communication needs.

Free space communications in the context of consumer needs is generally referring to microwave frequency technology, but free space laser communications are also in use for niche applications. While these are both part of the electromagnetic spectrum, as shown in Figure 1 - 2a the wavelength of these two technologies is several orders of magnitude different which leads to vastly different free space propagation and material interaction properties. For traditional radio communications, free space path loss is typically discussed and is given by,

$FSPL = \left(\frac{4\pi d}{\lambda}\right)^2$ , where  $\lambda$  is the wavelength of the carrier wave, and  $d$  is the propagation

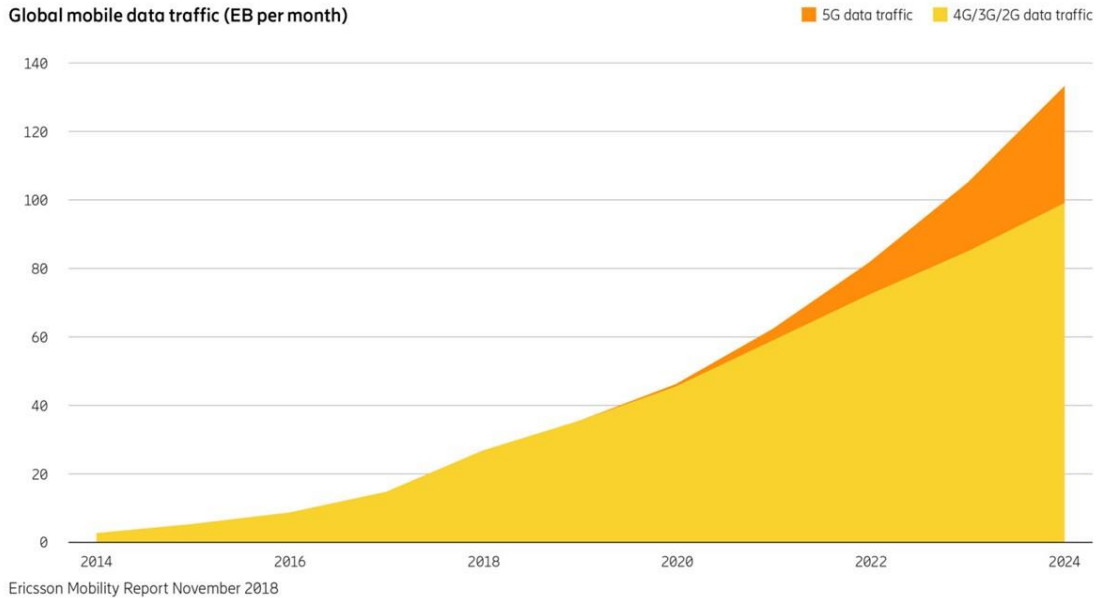
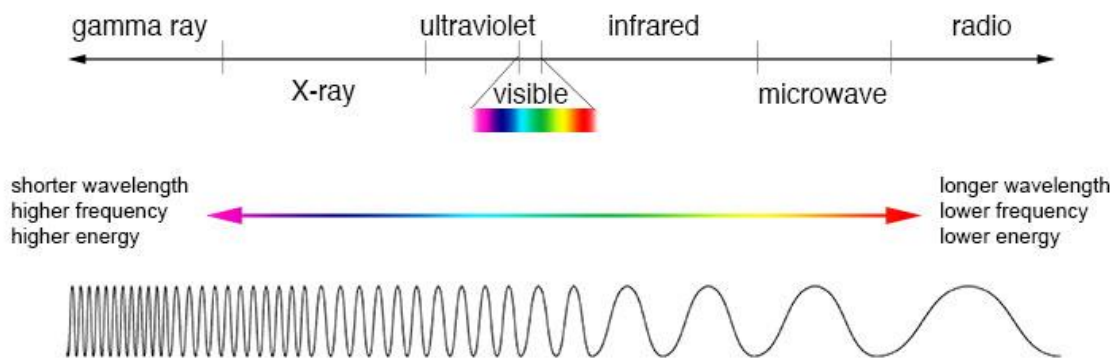
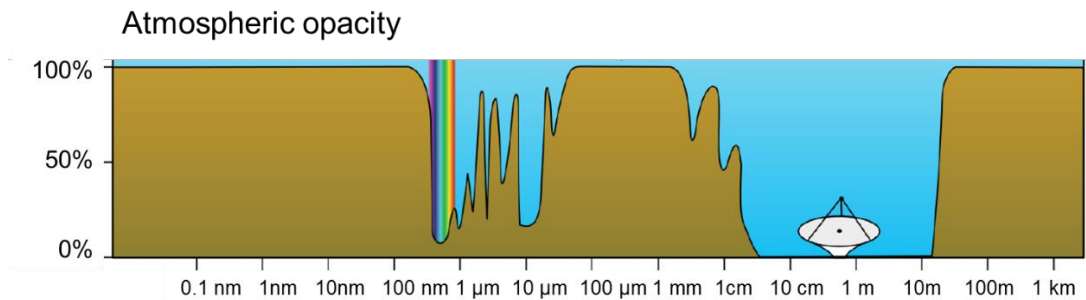


Figure 1 - 1 Global mobile data traffic over time. [3]

distance [4]. The decrease in the loss with increasing wavelength here is due to the increasing beam divergence that results from a radiation source of finite extent. The simplicity of this expression hides the fact that antenna or emitters can have vastly different directivities. For example, a mmW (1 mm wavelength) source compared to a typical radio (1 m wavelength) source from this expression would have six order of magnitude smaller free space loss. However, for the same size antenna aperture, the mmW antenna would have much large directivity, thus it is important to consider the specifics of the configuration to understand which frequency can be used most effectively. While this expression is used for radio and microwave communication systems utilizing antennas as the source of radiation, the underlying idea free space divergence holds at infrared wavelengths. We can write an



(a)



(b)

Figure 1 - 2 (a) Electromagnetic spectrum [5] (b) Atmospheric opacity vs wavelength (adapted from ref. [6]).

expression for the beam divergence angle assuming the beam is roughly gaussian as  $\theta = \frac{\lambda}{\pi n d_0}$ .

Here  $n$  is the index of the material, and  $d_0$  is the minimum beam waist size. The main contrast between radio to mmW sources and infrared (IR) sources is the source of radiation. While antennas are the most important commercial source of radio and mmW waves, in the IR emission is achieved by lasers which can be collimated to give beam waists on the order of the wavelength ( $\sim 1 \mu\text{m}$ ) with very little divergence [7], [8].

The interaction of the waves with matter is also significantly different. At the microwave frequency, interaction with molecules and solids comes predominantly from excitation of spatial degrees of freedom such as molecular rotations and vibrations, or the phonon modes of a solid. These interactions do not lend themselves to each detection and conversion into signals for processing, so antennas are designed using metals to couple the radiation into a transmission line that supports the continued propagation of the signal. At infrared frequencies, the interaction process occurs in the orbital and electronic degrees of freedom to excite bound electrons to higher molecular orbitals or energy band in a solid. In contrast to microwave signals, this allows for easy detection and conversion into electrical signals for processing through photodetectors. Figure 1 - 2b shows the atmospheric attenuation as a function of wavelength. At higher frequencies (shorter wavelength) interaction with gas molecules becomes limiting source of loss that prevents long distance communication, however, as mentioned above, as fiber optics become increasingly used in short reach networks, free space communication and mobile networks can be utilized for the short reach applications. Furthermore, due smaller beam divergence, direct line of sight obstruction becoming more significant as the frequency increases. In the infrared region, the confined optical beam must have a direct line of sight with tight alignment tolerance and suffers significant scattering from fog and rain. These factors and others lead to different frequency bands being chosen for specific applications depending on the demands. Depending on the frequency band chosen, a single isotropic antenna can meet the needs or alternatively, phased array antennas or other acquisition, pointing and timing techniques become important to ensure the receiver and transmitter are in a compatible configuration.

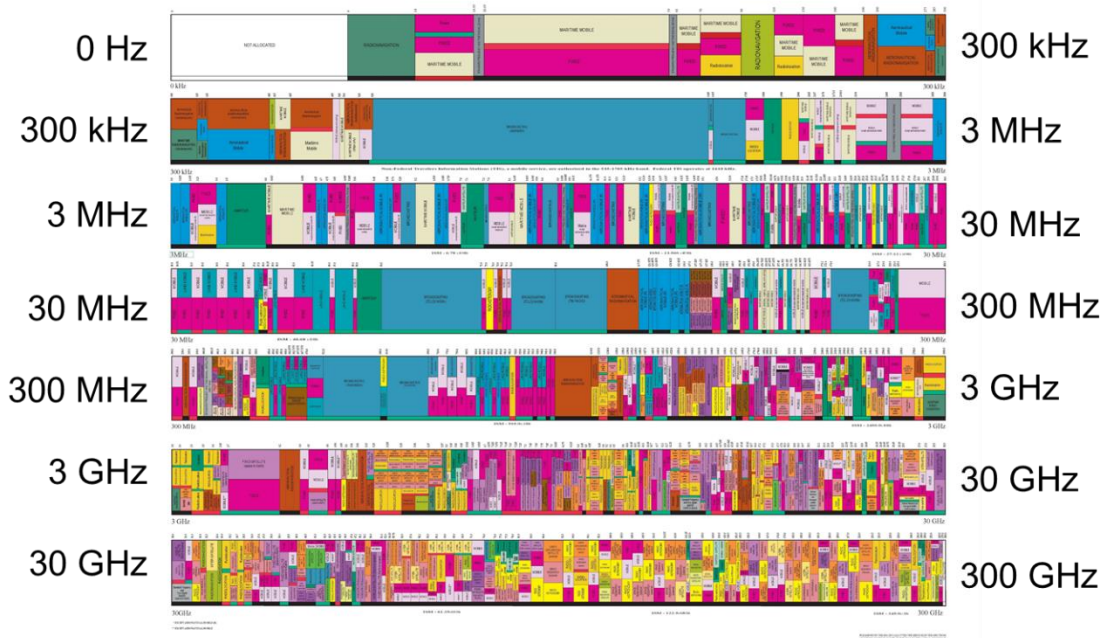


Figure 1 - 3 Frequency allocation between DC and 300 GHz (adapted from ref. [9]).

The discussion above gives the impression that moving to higher frequency signals presents several challenges ranging from increased free space path loss, higher atmospheric attenuation, and tighter alignment criteria. However, moving to higher frequency provides a significant benefit in the available frequency bandwidth for allocation to various applications. Figure 1 - 3 shows the frequency allocations spectrum from DC to 300 GHz. While the discussion has focused on mobile communication, there are many applications that utilize free space signals ranging from inter-satellite communication, radio astronomy, radio navigation, meteorology, and broadcasting. Thus, if we are restriction to the region shown in Figure 1 - 2b with low atmospheric attenuation, the total available bandwidth for all these applications is limited to a few GHz. By moving to higher frequencies, the available bandwidth is increased by orders of magnitude.

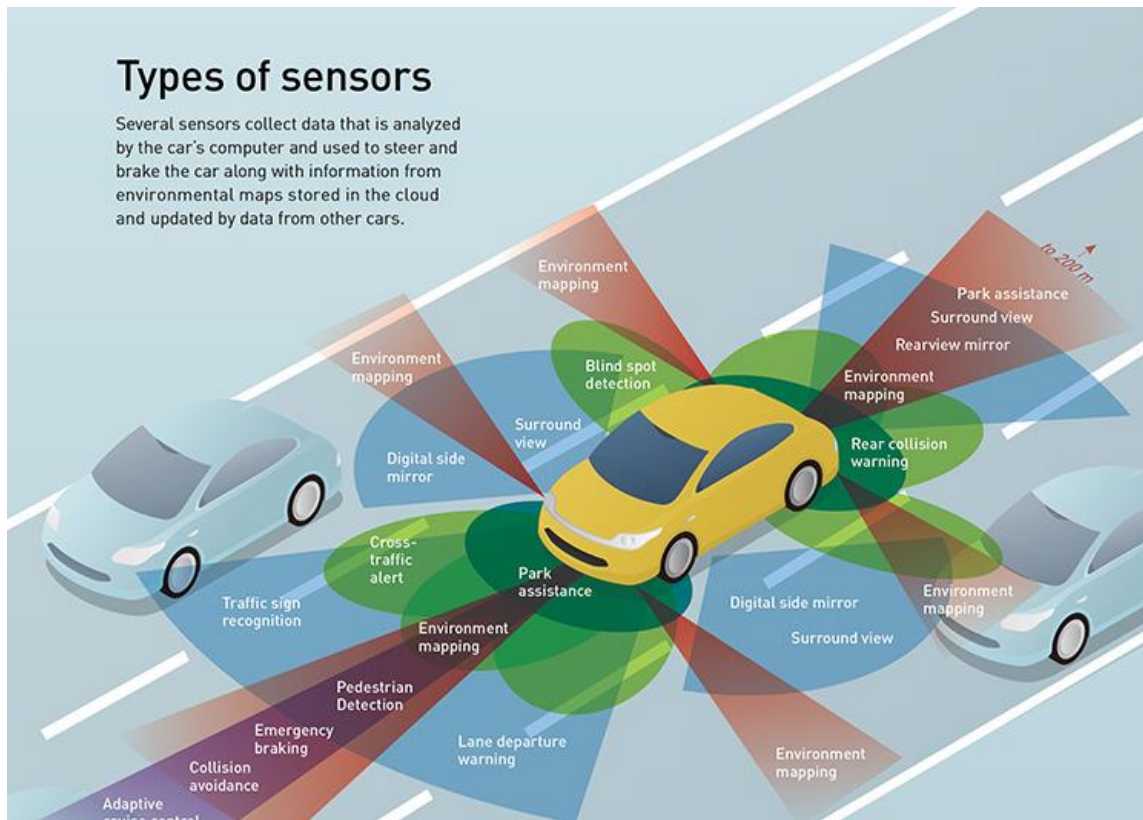


Figure 1 - 4 Sensor suite described to be used in future autonomous vehicles. The suite includes sensors at various frequencies to leverage the benefits of each. [10]

In the same way that various frequency ranges provide benefits for communication needs depending on the conditions and requirements, they also provide different benefits in the context of sensors. Figure 1 - 4 was published in the Optics and Photonics magazine demonstrating the suite of sensors that will likely be required as we move towards fully autonomous vehicles. While low frequencies, in the radio and microwave regime are good for ‘obtaining general information such as presence of an object of structure of large object (cloud patterns for weather), moving towards higher wavelengths gives a more detailed image and

or long-range measurements. Extending to the visible frequencies, images become usable for object recognition and identification.

The remainder of this thesis will be divided to first introduce the specifics of the two systems and applications that are being pursued: high speed uni-traveling-carrier photodiodes (UTC-PD) for generation of mmW and a widely tunable diode laser integrated with components to make a compact transceiver for frequency modulated continuous wave LIDAR. Next, details will be presented on the theory and performance metrics of photodetectors, design, and the fabrication of the devices. Results on the UTC-PDs will then be presented with discussion on performance limiting aspects of the devices. The transceiver PIC will then be presented with a discussion of the components and devices that were used in the design. The characterization of the PIC will be shown demonstrating the components of the circuit. Finally, future works will be discussed on how to improve the technologies and provide further demonstration of the capabilities.

In this thesis, the first waveguide UTC-PD optimized specifically for coupling to the Triplex SiN based planar lightwave circuit. The devices demonstrated greater than 60 GHz bandwidth and 6 dBm RF output power. Furthermore, the power conversion limitation for high speed PDs was extracted and shown to be a parameter that needs further study if photonic generation of mmW is to become a viable technology. Finally, the first compact PIC transceiver integrating a widely tunable laser, frequency discriminator, and receiver was demonstrated for the purpose of frequency modulated continuous wave LIDAR.

## References

- [1] L. a. Coldren, G. a. Fish, Y. Akulova, J. S. Barton, L. Johansson, and C. W. Coldren, “Tunable Semiconductor Lasers: A Tutorial,” *J. Light. Technol.*, vol. 22, no. 1, pp. 193–202, Jan. 2004.
- [2] D. F. (infinera) Welch *et al.*, “The Realization of Large-Scale Photonic Integrated Circuits and the Associated Impact on Fiber-Optic Communication Systems,” *J. Light. Technol.*, vol. 24, no. 12, pp. 4674–4683, 2006.
- [3] S. Bjgin and E. Purtova, “Ericsson Mobility Report (June 2019),” 2019.
- [4] C. A. Balanis, *Antenna theory*. Wiley, 2005.
- [5] A. Davies and A. Davies, “The Electromagnetic Spectrum,” *Digital Ultraviolet and Infrared Photography*, 2018. .
- [6] B. Weeden, “Radio Frequency Spectrum, Interference and satellites fact sheet,” 2013. [Online]. Available: [https://swfound.org/media/108538/swf\\_rfi\\_fact\\_sheet\\_2013.pdf](https://swfound.org/media/108538/swf_rfi_fact_sheet_2013.pdf).
- [7] S. O. Kasap, *Optoelectronics and Photonics*. 2013.
- [8] L. A. Coldren, S. W. Corzine, and M. L. Masanovic, *Diode Lasers and Photonic Integrated Circuits*, vol. 36, no. 2. Wiley, 1997.
- [9] “United States Frequency Allocation.”
- [10] J. Hecht, “Lidar for Self-Driving Cars,” *Optics and Photonics News*, no. January, pp. 26–33, 2018.

## **Chapter 2**

# **Photonic Generation of Millimeter Waves and Optical Beam Forming Networks for Phased Array Antennas**

For both the generation of mmW and IR signals, the starting point is a semiconductor diode laser. However, the subsequent aspects of the system are quite different owing to the several orders of magnitude different in desired frequency output. Here I will summarize the operating principles for mmW systems starting from the shared aspects of both systems.

In a crystalline solid, the energy levels of the atoms form well known bands with forbidden regions of energy called the band gap [1], [2]. In a semiconductor, the energy levels just below the band gap (valence band) are full and the energy levels above (conduction band) the gap are empty. This allows photons of energy greater than the band gap to be absorbed and excite the electrons to the conduction band and leaving a hole in the valence band. Alternatively, injecting free carriers into the material generates excess carriers in the conduction and valence band allows them to recombine and generate photons. In this case, the emission of the photon can be spontaneous or stimulated by the presence of other photons. Spontaneous emission is a result of the baseline transition probability that can be described by vacuum level photons. As the number of photons put into the mode increases, the transition probability increases

which stimulates the emission of additional photons. This a fundamentally a result of photons being spin-1 particles requiring them to follow Bose-Einstein statistics. Unlike fermions, which allow only one particle to occupy a state, an unlimited number of bosons can occupy a state, depending on the temperature of the system and the forces driving transitions. Furthermore, increasing the number of bosons in a state increases the transition probability into that state. Figure 2 - 1a show a schematic of in incoming photon stimulating the emission of second photon into the mode. This process can be exploited and designed to create cavities that sustain a photon density while outputting a coherent source of photons for some application. Much more discussion on these topics can be found in the references is expanded in refs. [1]–[5].

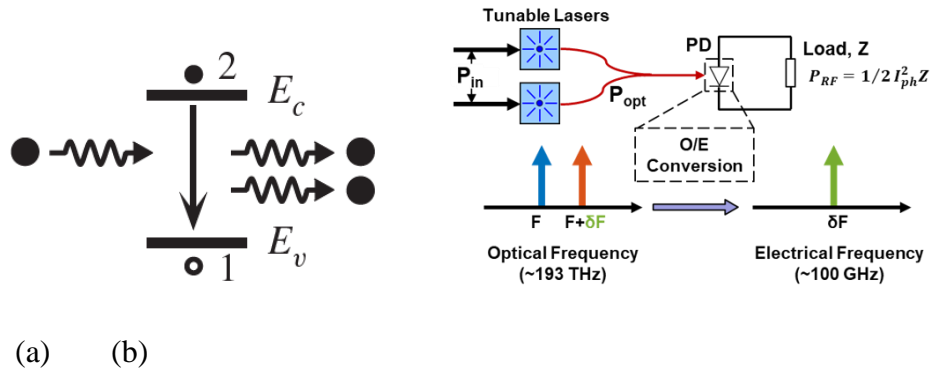


Figure 2 - 1 (a) Schematic of stimulated emission in a diode laser. An incoming photon stimulates the transition of an electron in the conduction band to the valence band, which emits a second photon (adapted from ref. [2]). (b) Schematic of using tunable lasers to generate microwave frequencies. Two lasers are tuned in frequency such that the difference between the lasing wavelength corresponds to the desired microwave frequency. The photodiode acts as a frequency filter to eliminate the optical frequency components leaving only the beat or different frequency between the two lasers. The signal can then be put to an antenna to radiate microwave radiation.

For infrared (IR) based sensing and communication, the emission from a semiconductor can be tailored to be at the frequency of interest usually around  $0.8 \mu\text{m}$  to  $2 \mu\text{m}$ . As a result,

the diode laser is a versatile source of radiation. Furthermore, by leveraging other electro-optic effects in semiconductors, a photonic integrated circuit (PIC) containing multiple components can be tailored such that the other components manipulate the light for the desired application [5], [6]. In the case of millimeter wave (mmW) generation, a similar approach has been demonstrated with gas molecules such as ammonia or hydrogen, however, this approach requires much larger hardware and is not convenient for widespread technology use [7], [8]. Alternative techniques for THz and mmW generation using optical methods started around 1992, using ps laser pulses on bulk LiNiO<sub>3</sub> crystals to generate broadband THz emission [9]. Subsequent papers demonstrated results on bulk InP with surface electrodes to accelerate the photogenerated electrons [10]. Delta doping of GaAs/AlGaAs at the surface and quantum well structures were demonstrated the following year in 1994 [11], [12]. This led towards the advent of using newly invented UTC-PDs for mmW generation with the eventual goal of THz sources [13]. A survey of various techniques for THz generation can be found in Ref. [14], [15].

Using the same IR laser as described above, the generation of mmW can be achieved by mixing two lasers with offset frequencies,  $\omega$  and  $\omega + \delta\omega$ , and coupling to a photodiode, which is called optical heterodyning [16]. Photodiodes convert incident photons into electrons by the stimulated absorption process [3]. The incident optical field of two lasers is described by

$$E = A_1 e^{-i\omega_1 t} + A_2 e^{-i\omega_2 t}$$

The power incident on the photodiode is proportional to the square of this field, and since the current in the diode and the power of the light are both proportional to the number of particles, the current can be written as

$$\begin{aligned}
I \propto P &\propto (A_1 e^{-i\omega_1 t} + A_2 e^{-i\omega_2 t}) \\
&= A_1^2 + A_2^2 + A_1 A_2 \cos(\delta\omega_{12} t) \\
&= \bar{P} + m\bar{P} \cos(\delta\omega_{12} t)
\end{aligned}$$

where  $\bar{P} = A_1^2 + A_2^2$  is the average incident power and  $m = \frac{A_1 A_2}{A_1^2 + A_2^2}$ , is the modulation index.

Thus, the result is an average photocurrent with a modulated photocurrent at the offset frequency of the laser. As shown in Figure 2 - 1b, the RF photocurrent can then feed an antenna (load element) to produce the radiation at the desired frequency [17].

## **mmW for OBFN**

For the application of mmW generation, the focus of this thesis is the optical to electrical conversion process. However, for context I will discuss the chief application that we were interested in, namely, optical beam forming networks (OBFN). An optical beam forming network is a circuit design to route and process optical signal for beam forming applications [18]–[20][21]. In this case, we were interested in combining an OBFN PIC with the UTC-PD to drive a phased array antenna (PAA). A PAA is an antenna that consists of multiple discrete radiators, that are driven by mutual RF signals with an increasing phase delay that is an integer multiple of a given phase delay [22]. The phase offset between radiating elements produces an envelope in the radiation pattern and steers the radiation pattern away from the central direction. This provide mechanical free steering of the radiation and allows a fixed aperture to be sensitive to a wider angle of incoming signals.

A common issue with this technology is the frequency dispersion of the RF phase shifters [23], [24]. The result of this is that at a fixed configuration, different frequencies will

radiate at different directions causing issues with frequency multiplexing [25], [26]. Converting to an optical signal processing platform provides two chief benefits: low loss transmission through fiber and true time delay of the signal. The first benefit leverages low loss optical fiber and allows the optical network and radiation elements to be located at the communication network cell, while the laser and modulation source can be centrally located. Low loss fiber then allows the light to be routed to the PIC for the phase delay processing. The second benefit, true time delay, describes the dispersion-less method of phase shifting the optical signal such that beam squint is eliminated. In our group, this was achieved using two different architectures: optical ring resonators (ORR) and switched delay lines [20], [27]. The ORR architecture has the benefit of continuous tunability but suffers from complex control and calibration. The switched delay path offers a simple ultra-wide band architecture but sacrifices continuous tunability for discrete tuning. A generic block diagram is shown in Figure 2 - 2. First, the laser is modulated, or two phased locked lasers are coupled into a common path. The phase locking is important for achieving a stable, narrow linewidth RF signal. A 50/50 splitter splits the two paths and encodes the data to be transmitted onto one path. Encoding onto only a single path prevents additional harmonics in the RF spectra after OE conversion. The paths are recombined and coupled to the OBFN PIC, where a  $1 \times N$  ( $N = 4$  in Figure 2 - 2)

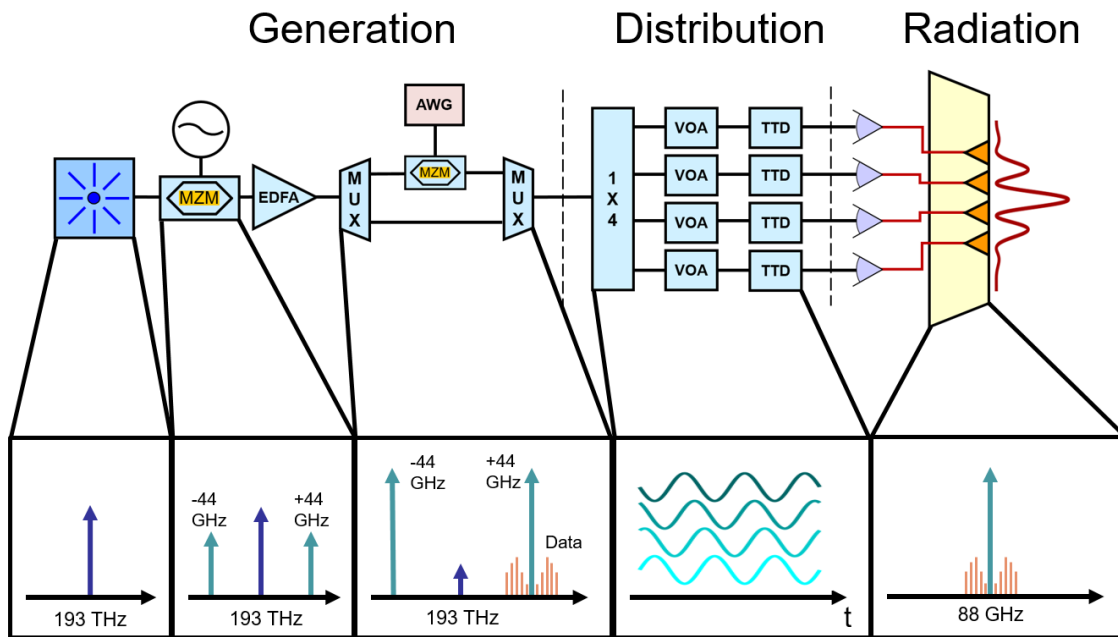


Figure 2 - 2 Schematic of optical components necessary for an optical beam forming network and phased array antenna system. The first component is a laser which emits 193 THz or 1.55  $\mu\text{m}$  radiation. The MZM generates two side bands, each offset one-half of the desired frequency from the main frequency. The signal is amplified and split between two paths, one of which is modulated with data before being recombined with the second path. The signals are then split into four separated paths, where the phase delay can be imparted by true time delay. Each path contains a high speed photodiode to down convert to the microwave signal before being fed to the antennas for emission. (Adapted from ref. [28])

splitter distributes the power between the paths with different time delays. The time delayed signals couple to off chip high speed PDs where the OE conversion happens, and the RF signals from the PDs drive the PAA producing the radiation pattern that can be steered by phase shifters on the OBFN chip. Additional details on the OBFN PIC can be found in Yuan Liu's thesis.

The following chapter will discuss system aspects of an InP PIC transceiver for LIDAR. Subsequent chapters on microwave photonics will focus on the optical to electrical conversion

element, the photodiode, discussing the device details, performance metrics, design, and measurement results.

## References

- [1] A. E. Siegman, *Lasers*, 10th ed., vol. 19, no. 8. University Science Books, 1981.
- [2] L. A. Coldren, S. W. Corzine, and M. L. Masanovic, *Diode Lasers and Photonic Integrated Circuits*, vol. 36, no. 2. Wiley, 1997.
- [3] J. Solyom, *Fundamentals of the Physics of Solids*, 5th ed. New York: Springer, 2002.
- [4] A. Zangwill, *Modern Electrodynamics*. Cambridge University Pres, 2012.
- [5] S. Adachi and K. Oe, “Linear electro-optic effects in zincblende- type semiconductors : Key properties of InGaAsP relevant to device design,” *J. Appl. Phys.*, vol. 56, no. 1, 1984.
- [6] S. O. Kasap, *Optoelectronics and Photonics*. 2013.
- [7] M. J. Reid and J. M. Moran, “Masers,” *Annu. Rev. Astron. Astrophys.*, vol. 19, 1981.
- [8] A. Javan, W. R. Bennett, and D. R. Herriott, “Population inversion and continuous optical maser oscillation in a gas discharge containing a He-Ne mixture,” *Phys. Rev. Lett.*, vol. 6, no. 3, pp. 106–110, 1961.
- [9] L. Xu, X. C. Zhang, and D. H. Auston, “Terahertz beam generation by femtosecond optical pulses in electro-optic materials,” *Appl. Phys. Lett.*, vol. 61, no. 15, pp. 1784–1786, 1992.
- [10] P. K. Benicewicz and A. J. Taylor, “Scaling of terahertz radiation from large-aperture biased InP photoconductors,” *Opt. Lett.*, vol. 18, no. 16, p. 1332, 1993.

- [11] S. L. Chuang, C. Paul, and I. Brener, "Terahertz Electromagnetic Pulses from Quantum-Well Structures," vol. 30, no. 6, pp. 1478–1488, 1994.
- [12] D. Birkedal, O. Hansen, C. B. Sorensen, K. Jarasiunas, S. D. Brorson, and S. R. Keiding, "Terahertz radiation from delta-doped GaAs," *Appl. Phys. Lett.*, vol. 65, no. 1, pp. 79–81, 1994.
- [13] T. Ishibashi, N. Shimizu, S. Kodama, H. Ito, T. Nagatsuma, and T. Furuta, "Uni-Traveling-Carrier Photodiodes," *OSA TOPS Ultrafast Electron. Optoelectron.*, vol. 13, pp. 83–87, 1997.
- [14] R. A. Lewis, "A review of terahertz sources," *J. Phys. D. Appl. Phys.*, vol. 47, no. 37, 2014.
- [15] P. Shumyatsky and R. R. Alfano, "Terahertz sources," *J. Biomed. Opt.*, vol. 16, no. 3, p. 033001, 2011.
- [16] S. Kawanishi and M. Saruwatari, "A Very Wide-Band Frequency Response Measurement System Using Optical Heterodyne Detection," *Trans. IEEE Instrum. Meas.*, vol. 38, no. 2, pp. 1–5, 1989.
- [17] S. Iezekiel, M. Burla, J. Klamkin, D. Marpaung, and J. Capmany, "RF Engineering Meets Optoelectronics: Progress in Integrated Microwave Photonics," *IEEE Microw. Mag.*, vol. 16, no. 8, pp. 28–45, 2015.
- [18] Y. Liu *et al.*, "Tuning Optimization of Ring Resonator Delays for Integrated Optical Beam Forming Networks," *J. Light. Technol.*, vol. 35, no. 22, 2017.
- [19] R. Benjamin and A. Seeds, "Optical beam forming techniques for phased array antennas," *IEE Proc. H (Microwaves, Antennas ...)*, vol. 139, no. 6, 1992.

- [20] Y. Liu *et al.*, “Ultra-Low-Loss Silicon Nitride Optical Beamforming Network for Wideband Wireless Applications,” *IEEE J. Sel. Top. Quantum Electron.*, vol. 24, no. 4, 2018.
- [21] J. A. Nanzer, A. Wichman, J. Klamkin, T. P. McKenna, and T. R. Clark, “Millimeter-Wave Photonics for Communications and Phased Arrays,” *Fiber Integr. Opt.*, vol. 34, no. 4, pp. 159–174, 2015.
- [22] C. A. Balanis, *Antenna theory*. Wiley, 2005.
- [23] D. M. Pozar, *Microwave Engineering*. Wiley, 2012.
- [24] C. G. H. Roeloffzen *et al.*, “Silicon nitride microwave photonic circuits,” *Opt. Express*, vol. 21, no. 19, pp. 22937–22961, 2013.
- [25] S. D. Targonski and D. M. Pozar, “Minimization of Beam Squint in Microstrip Reflectarrays Using an Offset Feed,” in *IEEE Antennas and Propagation Society International Symposium*, 1996.
- [26] S. Keser and M. Mojahedi, “Removal of beam squint in series fed array antennas using abnormal group delay phase shifters,” in *2010 IEEE Antennas and Propagation Society International Symposium*, no. 1.
- [27] Y. Liu *et al.*, “Integrated silicon nitride optical beamforming networks for wideband communications,” *Opt. InfoBase Conf. Pap.*, vol. Part F101-, pp. 3–4, 2018.
- [28] J. A. Nanzer, T. P. McKenna, and T. R. Clark, “A W-band photonic array,” *IEEE Antennas Propag. Soc. AP-S Int. Symp.*, pp. 239–240, 2014.

## Chapter 3

# Operating Principles of Frequency

## Modulated Continuous Wave LIDAR

Tunable lasers and photonic integrated circuits (PIC) have demonstrated performance improvements for several decades in the telecommunication industry enabling over 100 Gbps data rates [1]–[7]. Furthermore, advancements in silicon photonics have increasingly enabled integrated photonic platforms with high component density [4], [6], [7]. Beyond communication application, tunable lasers and PICs are enabling compact solutions for remote sensing, detection, and spectroscopy. Each individual application puts forth specific requirements on the PIC. Laser performance such as power output, linewidth, and tuning range become important parameters to optimize for the specific application. One emerging technology that can benefit from tunable lasers and photonic integration is Light Detection and Ranging, or LiDAR. In contrast to RaDAR, LiDAR utilizes signals at optical frequencies which improves the spatial resolution of the imaging, opening possible solutions to autonomous driving, robotics, and terrain mapping. There are several approaches to LiDAR as discussed in refs. [8]–[10]. Photonic integration opens the possibility to reduce the system size, as a single chip can contain many of the necessary system elements such as acting as both a tunable light source and receiver.

Compared to standard pulsed techniques for LiDAR, frequency modulated continuous wave (FMCW) LiDAR has the benefit of low peak power, which makes it a good candidate to implement in semiconductor waveguides [11]–[14]. In this approach, the laser frequency is modulated with a triangular waveform, and split to serve as both an output signal to an optical phased array (OPA) and a reference for the detection. The OPA can provide 2D beam steering by utilizing phase shifters for steering along one direction, and frequency dispersion of the optical antenna for steering along the orthogonal direction [15]–[17]. The reflected echo signal couples back through the OPA to a receiver where it is mixed with the reference signal to generate the measurement result. The frequency modulation allows the time-of-flight to be determined by the beat frequency generated in the receiver. The echo signal frequency is offset from the reference by  $\delta f = 2 \frac{\Delta F}{T} \delta t$ , where  $\Delta F$  is the total frequency modulation range,  $T$  is the period of the frequency modulation, and  $\delta t$  is the time-of-flight for the echo signal. The object distance can then be determined from  $d = c \cdot \frac{\delta t}{2}$ , where  $c$  is the speed of light. Using a triangular waveform, in contrast to a sawtooth waveform, allows both spatial and velocity information to be obtained as the object movement imparts a doppler shift to the echo signal frequency. The result is that the rising and falling portions of the waveform generate different beat frequencies which causes the peaks in the stationary frequency spectrum to be split by the doppler frequency  $\delta f_D = 2f_0 \cdot \left(\frac{\Delta v}{c}\right)$ .

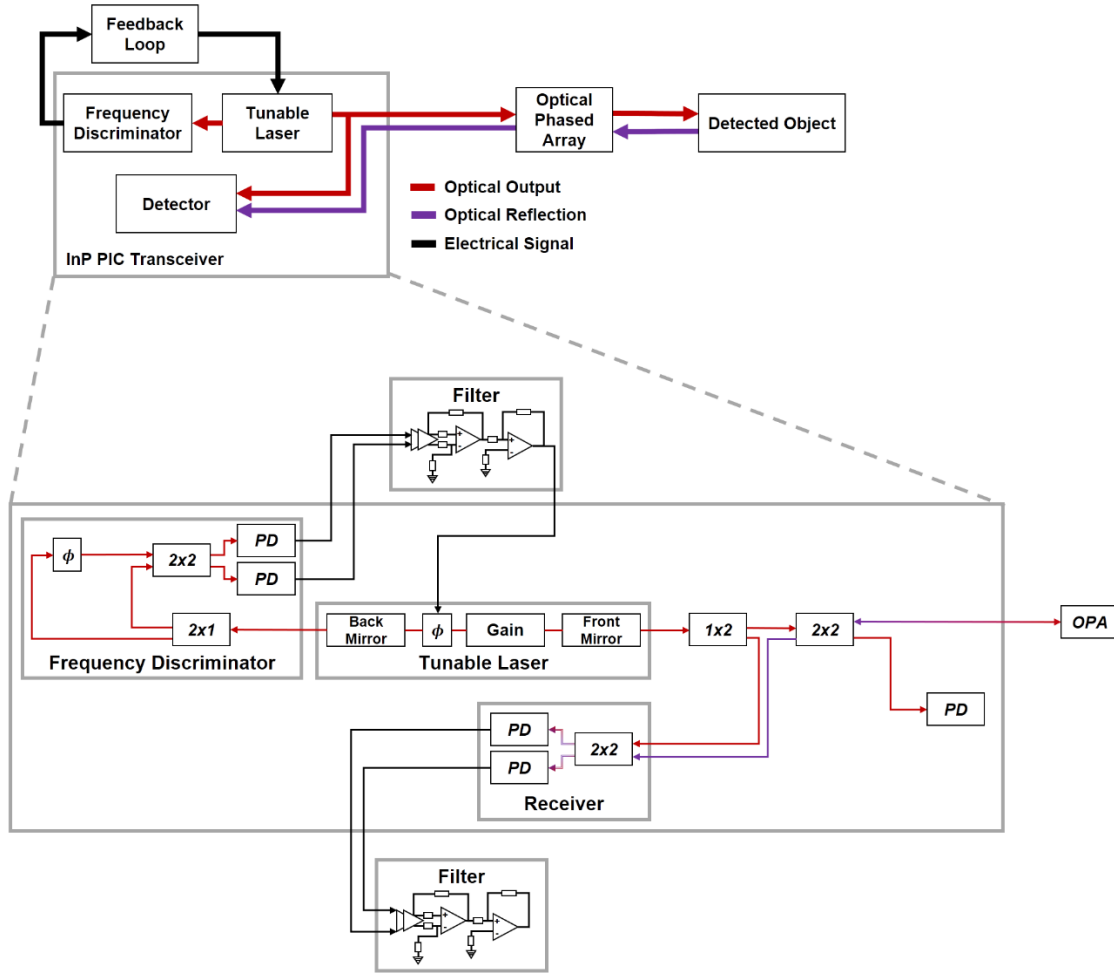


Figure 3 - 3 Block diagram of the transceiver and OPA system (left). The tunable laser provides a signal for the OPA and on-chip frequency discriminator that drives an off-chip feedback circuit for frequency locking the laser. The detector utilizes tapped power from the tunable laser in a self-heterodyne measurement to convert object distance to a beat frequency as the tunable laser is frequency modulated. The expanded region (right) shows the transceiver PIC components including gain, phase, and mirrors of the laser; semiconductor optical amplifier (SOA); 1x2 and 2x2 splitters; phase shifters; and photodetectors (PD).

For the signal generation in a LiDAR system, indium phosphide (InP) provides mature PIC components and ability for active-passive integration to form an integrated transceiver

[[2], [5], [18]–[22]]. A block diagram of the LiDAR system is shown in Figure 3 - 3, along with a more detailed block diagram of the InP transceiver. The InP transceiver PIC can be coupled to an OPA which serves as the emitting and receiving aperture. The transmitter and receiver are discussed in further detail below.

## **Transmitter**

The transmitter consists of a widely tunable laser and a frequency discriminator [23]–[25]. The tunable laser is an SGDBR laser which consists of a DBR laser modified by periodic blanking of the front and back grating mirrors at different sampling periods. This produces a Vernier-like reflection spectra allowing for wide tunability [26]. The SGDBR laser was designed for tuning over the wavelength range of 1530 nm to 1570 nm. Coarse tuning of the wavelength is achieved by differential injection of current into the front and back mirrors of the laser. Fine tuning is achieved by equal current injection into the mirrors, or by current injection in a phase shifter inside the SGDBR cavity which controls the cavity mode locations. The grating design of the SGDBR also considers the front-to-back splitting to obtain the desired LiDAR output power and the sensitivity of the frequency discriminator. For this purpose, the mirror reflections were designed to give a front-to-back power splitting ratio of 7:1 by optimizing the number of sampled grating bursts. Power from the front mirror is guided to two semiconductor optical amplifiers (SOA), and 1x2 and 2x2

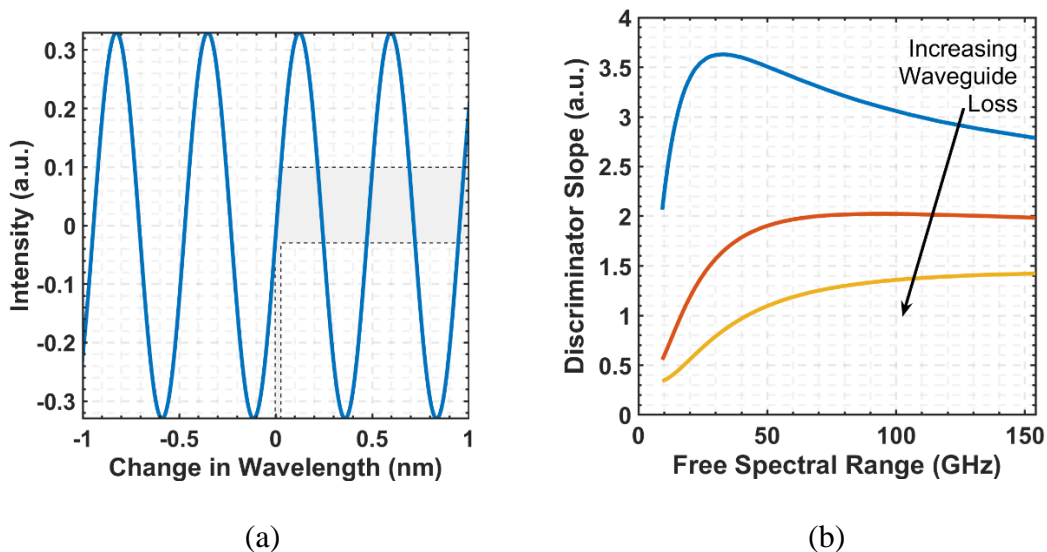


Figure 3 - 4 (a) Output of a-MZI under balanced detection calculated from Eq. 1. The shaded region illustrates the amplitude change due to frequency changes of the laser output. (b) a-MZI based frequency discriminator sensitivity as the FSR varies for different passive waveguide losses. The orange curve uses a loss of  $4 \text{ cm}^{-1}$  typical for deep ridge waveguides in InP [23,24,26].

splitters for the OPA and receiver. The two SOAs use the same gain material as the SGDBR laser but are tapered to increase the mode size to prevent gain saturation. The 1x2 splitter is utilized to tap power for use in the receiver as a reference to the echo signal. A second, 2x2, splitter is utilized for two purposes: first, to couple the reflected signal to the receiver, and second to measure chip temperature through an on-chip PD. The laser, SOAs, couplers, and PDs were all implemented in surface ridge waveguides to minimize passive waveguide loss.

Frequency stabilization is achieved using a tunable a-MZI filter using deep ridge waveguides. The a-MZI converts frequency fluctuations of the laser to amplitude fluctuations of the PD currents. Power from the back mirror of the SGDBR laser is split by a 1x2 multimode interference coupler (MMI) between the two different paths of the a-MZI. The

longer path also contains a phase shifter for tuning the filter quadrature frequency. A 2x2 MMI mixes the output from the two paths to allow balanced photodetection, eliminating common mode noise from the SGDBR laser. The transfer matrix relating the input electric field amplitude to the photocurrents in each PD is shown below:

$$\begin{pmatrix} I_1 \\ I_2 \end{pmatrix} \propto \left| \begin{pmatrix} 1 & j \\ j & 1 \end{pmatrix} \begin{pmatrix} e^{(j\beta-\alpha)L_1} & 0 \\ 0 & e^{\phi} e^{(j\beta-\alpha)(L_1+\delta L)} \end{pmatrix} \begin{pmatrix} 1 & j \\ j & 1 \end{pmatrix} \begin{pmatrix} E_0 \\ 0 \end{pmatrix} \right|^2 \quad \text{Eq. (1)}$$

Here,  $E_0$  is the square root of the laser output power,  $\beta$  is the propagation constant of the waveguide mode,  $\alpha$  is the waveguide loss,  $L_1$  is the length of the shorter path in the a-MZI,  $\delta L$  is the additional path length of the second path,  $\phi$  is the tunable phase shift in the second path, and  $I_{1,2}$  is photocurrent in each PD. The transfer function using balanced photodetection is shown in Figure 3 - 4a. Equation 1 can be used to determine the sensitivity to frequency fluctuations by calculating  $\frac{dI}{d\lambda}$  and taking the maximum value. The sensitivity of the discriminator is determined by the input optical power, waveguide loss, and the free spectral range (FSR) of the a-MZI which is given by  $c \cdot (n_{eff}\Delta L)^{-1}$ . The sensitivity is quantified in terms of the discriminator slope as shown in Fig. 2b. The sensitivity, or slope, increases as the FSR decreases; however, the additional path length required to reduce the FSR increases the total loss. This reduces the sensitivity, as the photocurrent amplitude is proportional to the square of the electric field amplitude at the input. To address this trade-off, an FSR of 60 GHz was selected based on previous loss values of  $4 \text{ cm}^{-1}$  reported for deep ridge waveguides in InP [24], [25], [27]. The photocurrents generated in each PD are input to an off-chip circuit containing a two-stage differential amplifier with an inverting input to create the balanced detection, and a two-stage op-amp filter to drive the difference in PD

photocurrents to zero. The amplifiers and filter act to convert the error to a current and inject it into the phase section of the laser cavity. This tunes the frequency of the laser to the quadrature point of the a-MZI where the power is equally split between the two photodiodes and the error is zero.

The a-MZI also contains a phase shifter in one path to shift the output interference independent of the frequency of the laser. This control is referred to as the “chirp” to reduce confusion with phase shifter in the SGDBR cavity. Injecting current into the chirp section tunes the quadrature frequency where the a-MZI equally splits the power between the two PDs. When the laser is frequency locked by the external circuit, tuning the quadrature frequency allows control over the laser frequency. By applying a modulated current to the chirp, the PIC can be used to realize FMCW LiDAR.

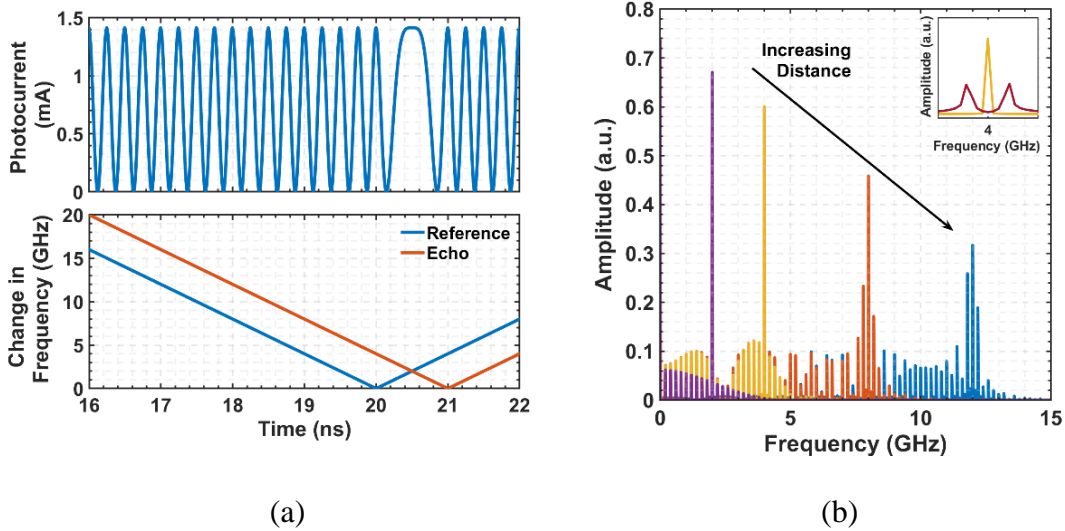


Figure 3 - 5 (a) Receiver operation principle. Bottom graph shows the instantaneous frequency of the reference and echo signal as a function of time. The top graph shows the measured photocurrent as the reference and echo signals beat together on the receiver PDs. (b) Frequency spectrum of the receiver photocurrent for reflections at different distances. The inset shows peak splitting due to the doppler effect for moving objects.

## Receiver

The receiver consists of a 2x2 splitter and two PDs, which act to self-heterodyne the laser output with the received echo. Utilizing a 2x2 splitter allows for balanced photodetection in the receiver circuit to reject common mode noise and signal. The echo signal is coupled back into the transceiver PIC through the same port that coupled the output into the OPA. As shown in Figure 3 - 5a, the reference and echo signal differ in frequency due to the additional travel time of the echo signal. The bottom graph shows the instantaneous frequency of the reference and echo signal at the receiver. The top graph shows the current measured by the receiver PDs that contains the beat frequency of the two signals. Figure 3 - 5b shows the calculated frequency spectrum of the PD current for measurements on objects at different distances to illustrate the change in the peak frequency of the photocurrent. The inset shows the peak splitting imparted by a moving object due to doppler frequency shifts as discussed previously. Also visible in the spectrums of Figure 3 - 5b are satellite peaks arising from the beat frequency transient as the modulation changes direction (seen around 20 ns in Fig. 2c). This transient region sets the maximum range of the FMCW LiDAR system barring laser coherence length considerations. As the objects distance approaches one-half of the chirp period, the receiver photocurrent undergoes a constant frequency modulation and the spectrum is not peaked around a single value. Additionally, due to finite laser linewidth, there is a minimum detectable frequency shift, which affects the distance resolution as there will be some broadening in the frequency spectrum. The modulation period and rate must be selected to address desired range which is ultimately limited by the laser linewidth and frequency

modulation bandwidth. The frequency locking technique described previously has demonstrated a linewidth of 570 kHz, which gives a maximum range of 160 m [25].

An important note on integration of the transmit and receive circuits for FMCW LiDAR, is the impact of the echo signal on the stability of the tunable laser. This can be broken down into three regimes: short-range (on-chip), medium-range, and long-range reflections. For the first case, all on-chip optical interfaces are angled to minimize reflections. Furthermore, it is well established that laser stability is not strongly influenced for very short external cavities [28], [29]. In the case of medium-range reflections, where the reflected power may be significant, the frequency modulation detunes the instantaneous emitting frequency from the reflection such that the influence of the reflections is strongly reduced[30]. For long range reflections, in addition to frequency detuning, the power will be below the limit to influence stability.

Significant discussion on the frequency locking is found in Ref. XX including discussion on linewidth reduction, feedback circuit details, and performance. Subsequent chapters on the InP PIC will discuss device details, fabrication, characterization of the components.

## References

- [1] L. a. Coldren, “Monolithic tunable diode lasers,” *IEEE J. Sel. Top. Quantum Electron.*, vol. 6, no. 6, pp. 988–999, Nov. 2000.
- [2] S. Arafin and L. A. Coldren, “Advanced InP Photonic Integrated Circuits for Communication and Sensing,” *IEEE J. Sel. Top. Quantum Electron.*, vol. 24, no. 1, 2018.

- [3] D. F. (infinera) Welch *et al.*, “The Realization of Large-Scale Photonic Integrated Circuits and the Associated Impact on Fiber-Optic Communication Systems,” *J. Light. Technol.*, vol. 24, no. 12, pp. 4674–4683, 2006.
- [4] R. A. Soref, “The Past, Present, and Future of Silicon Photonics,” *IEEE J. Sel. Top. Quantum Electron.*, vol. 12, no. 6, pp. 87–94, 2006.
- [5] J. Klamkin *et al.*, “Indium Phosphide Photonic Integrated Circuits: Technology and Applications,” in *2018 IEEE BiCMOS and Compound Semiconductor Integrated Circuits and Technology Symposium, BCICTS 2018*, 2018.
- [6] R. Nagarajan, M. Filer, Y. Fu, M. Kato, T. Rope, and J. Stewart, “Silicon photonics-based 100 Gbit/s, PAM4, DWDM data center interconnects,” *J. Opt. Commun. Netw.*, vol. 10, no. 7, pp. B25–B36, 2018.
- [7] T. Pinguet *et al.*, “High-Volume Manufacturing Platform for Silicon Photonics,” *Proc. IEEE*, vol. 106, no. 12, pp. 2281–2290, 2018.
- [8] T. Bosch, “Laser ranging: a critical review of usual techniques for distance measurement,” *Opt. Eng.*, vol. 40, no. 1, p. 10, 2001.
- [9] B. Schwarz, “Mapping the world in 3D,” *Nat. Photonics*, vol. 4, no. 7, pp. 429–430, 2010.
- [10] M. Flood, “Laser Altimetry: From Science to Commercial Lidar Mapping,” *Photogramm. Eng. Remote Sensing*, vol. 67, no. 11, pp. 1209–1218, 2001.
- [11] H. K. Tsang *et al.*, “Optical dispersion, two-photon absorption and self-phase modulation in silicon waveguides at 1.5 $\mu$ m wavelength,” *Appl. Phys. Lett.*, vol. 80, no. 3, pp. 416–418, 2002.
- [12] L. Yin and G. P. Agrawal, “Impact of two-photon absorption on self-phase modulation in silicon waveguides,” *Opt. Lett.*, vol. 32, no. 14, p. 2031, 2007.
- [13] W. I. H. *et al.*, “Two-photon absorption and self-phase modulation in InGaAsP InP multi-quantum-well waveguides,” *J. Appl. Phys.*, vol. 70, no. 3992, 1991.
- [14] C. C. Lee and H. Y. Fan, “Two-photon absorption and photoconductivity in GaAs and InP,” *Appl. Phys. Lett.*, vol. 20, no. 1, pp. 18–20, 1972.
- [15] S. Pinna, B. Song, L. A. Coldren, and J. Klamkin, “Vernier Transceiver Architecture for Side-Lobe-Free and High-Entendue LiDAR,” *2018 Conf. Lasers Electro-Optics, CLEO 2018 - Proc.*, no. 1, pp. 3–4, 2018.

- [16] J. C. Hulme *et al.*, “Fully integrated hybrid silicon two dimensional beam scanner,” *Opt. Express*, vol. 23, no. 5, p. 5861, 2015.
- [17] J. K. Doyle, M. J. R. Heck, J. T. Bovington, J. D. Peters, L. A. Coldren, and J. E. Bowers, “Two-dimensional free-space beam steering with an optical phased array on silicon-on-insulator,” *Opt. Express*, vol. 19, no. 22, p. 21595, 2011.
- [18] B. Isaac, B. Song, S. Pinna, S. Arafin, L. Coldren, and J. Klamkin, “Indium Phosphide Photonic Integrated Circuit Transmitter with Integrated Linewidth Narrowing for Laser Communications and Sensing,” *Conf. Dig. - IEEE Int. Semicond. Laser Conf.*, vol. 2018-Septe, no. November, pp. 53–54, 2018.
- [19] P. R. A. Binetti *et al.*, “Indium phosphide photonic integrated circuits for coherent optical links,” *IEEE J. Quantum Electron.*, vol. 48, no. 2, pp. 279–291, 2012.
- [20] Y. A. Akulova *et al.*, “Widely tunable electroabsorption-modulated sampled-grating DBR laser transmitter,” *IEEE J. Sel. Top. Quantum Electron.*, vol. 8, no. 6, pp. 1349–1357, 2002.
- [21] J. W. Raring *et al.*, “Single-chip 40Gb/s widely-tunable transceivers with integrated SG-DBR laser, QW EAM, UTC photodiode, and low confinement SOA,” *Conf. Dig. - IEEE Int. Semicond. Laser Conf.*, no. c, pp. 7–8, 2006.
- [22] H. Zhao *et al.*, “Indium Phosphide Photonic Integrated Circuits for Free Space Optical Links,” *IEEE J. Sel. Top. Quantum Electron.*, vol. 24, no. 6, pp. 1–6, 2018.
- [23] B. Isaac, B. Song, S. Pinna, S. Arafin, L. Coldren, and J. Klamkin, “Indium Phosphide Photonic Integrated Circuit Transmitter with Integrated Linewidth Narrowing for Laser Communications and Sensing,” in *Conference Digest - IEEE International Semiconductor Laser Conference*, 2018, vol. 2018-Septe.
- [24] A. Sivananthan *et al.*, “Monolithic Linewidth narrowing of a tunable SG-DBR laser,” *Opt. Fiber Commun. Conf. OFC 2013*, pp. 1–3, 2013.
- [25] A. Sivananthan *et al.*, “Integrated linewidth reduction of a tunable SG-DBR laser,” *2013 Conf. Lasers Electro-Optics, CLEO 2013*, vol. 4, no. 12, pp. 1–2, 2013.
- [26] V. Jayaraman, Z.-M. Chuang, and L. a. Coldren, “Theory, design, and performance of extended tuning range semiconductor lasers with sampled gratings,” *IEEE J. Quantum Electron.*, vol. 29, no. 6, pp. 1824–1834, Jun. 1993.
- [27] J. S. Parker, E. J. Norberg, R. S. Guzzon, S. C. Nicholes, and L. A. Coldren, “High verticality InP/InGaAsP etching in Cl<sub>2</sub>/H<sub>2</sub>/Ar inductively coupled plasma for photonic

- integrated circuits,” *J. Vac. Sci. Technol. B, Nanotechnol. Microelectron. Mater. Process. Meas. Phenom.*, vol. 29, no. 1, p. 011016, 2011.
- [28] L. A. Coldren, S. W. Corzine, and M. L. Masanovic, *Diode Lasers and Photonic Integrated Circuits*, vol. 36, no. 2. Wiley, 1997.
- [29] K. Petermann, *Laser Diode Modulation and Noise*. Kluwer Academic Publishers, 1988.
- [30] L. A. Johansson and L. A. Coldren, “Wavelength-tunable receiver channel selection and filtering using sg-dbr laser injection-locking,” in *Optical Fiber Communication Conference and Exposition and The National Fiber Optic Engineers Conference*, 2005, pp. 2–4.

# Chapter 4

## Photodiode Device Fundamentals, Design, and Fabrication

Photonic integration can be achieved in various platforms each having its own strengths and weaknesses. Table 1 summarizes common platforms and their advantages and disadvantages [1]–[3]. The devices described here are exclusively based on the InP-InGaAsP material system. Figure 4 - 1 shows a commonly used plot of III/V bandgap vs. lattice constant. One of the main strengths of InP, is the ability to lattice match InGaAsP alloys of varying compositions to achieve devices with bandgap wavelengths between 1.7  $\mu\text{m}$  and 0.98  $\mu\text{m}$ . This allows high performance active and passive components to be integrated on a single wafer without the challenges of lattice mismatched growths. For lasers and SOAs, slight strain can be introduced to enhance TE/TM emission probability within the material system. Here we summarize fundamentals of the various devices used for this work.

**Table 1 Comparison of different platforms for photonics**

<b>System</b>	<b>Strengths</b>	<b>Weaknesses</b>
InP	Active devices, compact	Relatively high loss
Silicon Photonics	Low loss, some active devices, compact	No gain medium
Lithium Niobate	High performance modulators	Large devices due to low confinement, no gain medium
Planar Lightwave Circuits	Very low loss	No active components

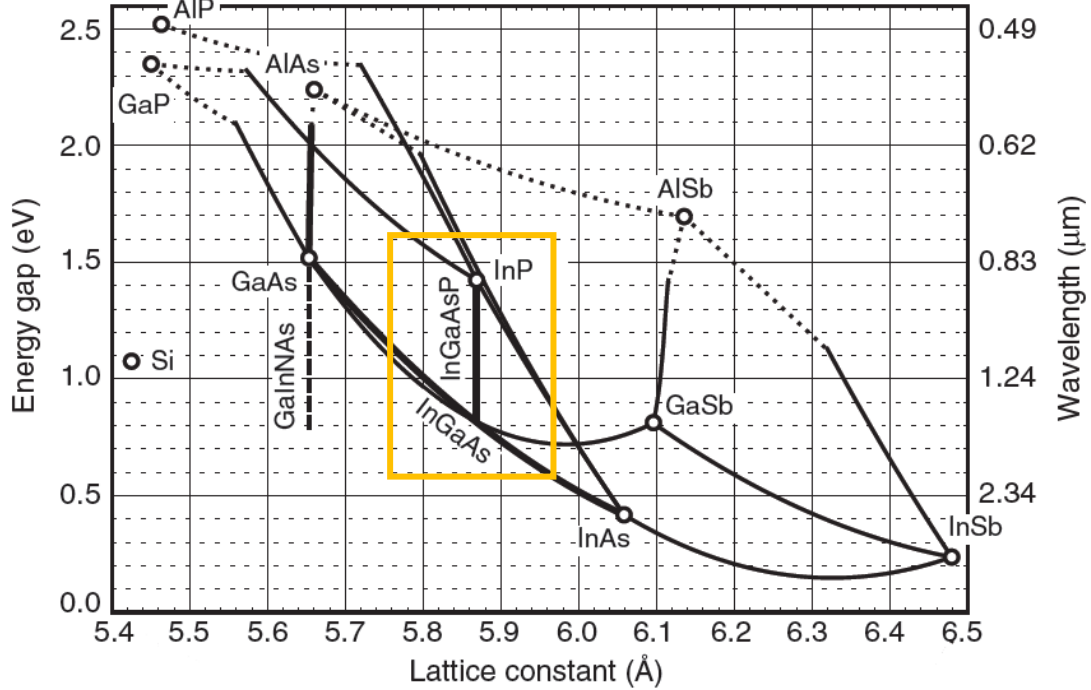


Figure 4 - 1 Bandgap vs. lattice constant diagram of various semiconductor material systems. This thesis is largely confined to the regions boxed in yellow consisting of InP, alloys of InGaAsP that are closely lattice matched to InP, and the InGaAs alloy that is lattice matched in InP. Figure adapted from [4]

## PN-Junctions

Photonics devices are almost exclusively based on PN junctions or diodes, so it is critical to understand the physics that governs their behavior. Reference [5] provides a detailed analysis of diode physics. Here, I will give an overview of their behavior. When an n-type semiconductor is in intimate contact with a p-type, the free carriers diffuse due to the concentration gradient and after recombining with each other, form a built-in electric field that eventually balances the driving force of diffusion. As shown in Figure 4 - 2a, when there is no externally applied bias, the built-in electric field of the junction sweeps carrier out of the

depletion region according to their charge. This is balanced by the thermal emission of carriers across the depletion region for a net current of zero. Under forward and reverse bias, the balance is altered as discussed below.

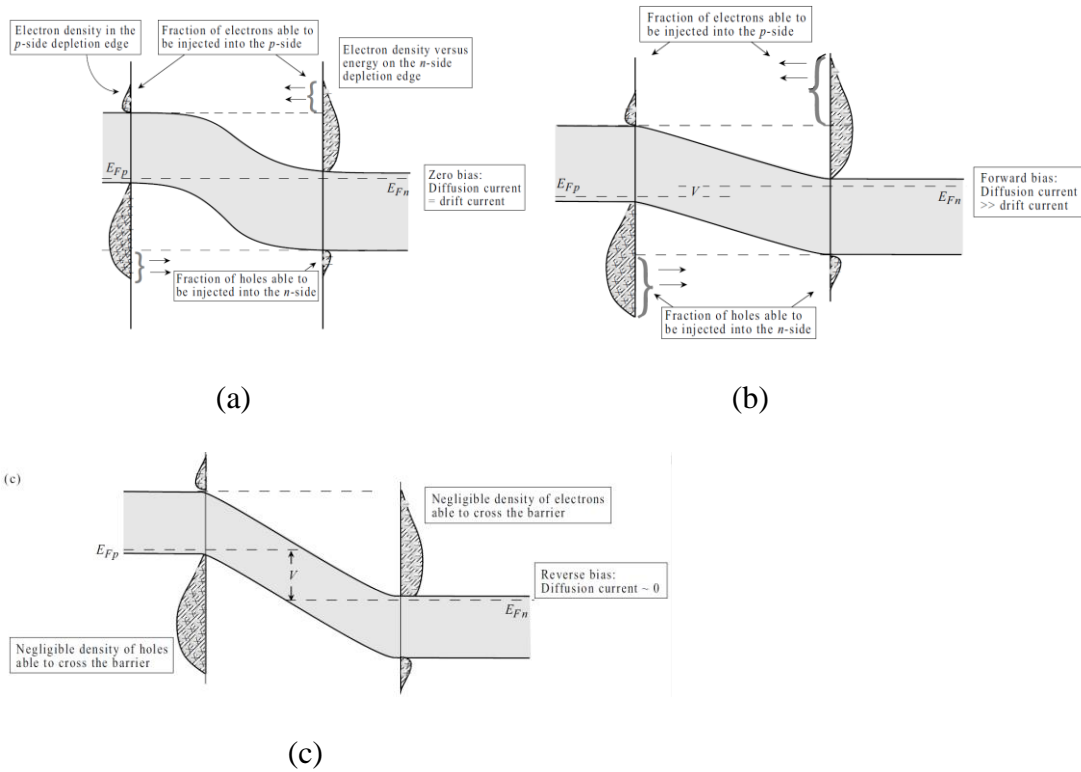


Figure 4 - 2 (a) Diagram of PN-junction under zero applied bias. The equilibrium distribution of electrons and holes on each side of the PN-junction is such that the thermal emission of carriers across the barrier (diffusion current) is balanced by the drift current that results from the electric field in the depletion region. (b) Under forward bias the equilibrium is disturbed by the increase carrier with enough kinetic energy to overcome the reduced barrier. (c) Under reverse bias, the barrier is increased. As a result, there are almost no carriers with enough kinetic energy to get across the barrier, and the number of minority carriers on each side of the PN-junction is reduced leading to a very small drift current. Figure adapted from [5].

### **Forward Bias Operation**

In the case of a positive applied bias, the electric field is reduced, and the thermally injected carriers are drastically increased, and a net current flow as shown in Figure 4 - 2b. The current-voltage relations are given by

$$I = I_0 \left( e^{\frac{\beta}{n}(V_{bias} - V_{\phi})} - 1 \right)$$

where  $I_0$  is a constant dependent on material properties,  $\beta = \frac{1}{k_B T}$ ,  $V_{\phi}$  and  $V_{bias}$  being the junction built in voltage, and  $n$  being the diode ideality factor. The diode ideality factor depends largely on whether the current within the junction is primarily from diffusion or from recombination of the carriers in the active region. In the case of a simple PN or PIN structure like those shown in Figure 4 - 2, there is a transition from recombination current to diffusion dominated current as the bias voltage is increased. In either case, because this sort of structure does not include gain material, or quantum wells, the effect is the change the effective index through a combination of effects [6]. It is intuitive to describe the change in refractive index in the context of changing the absorption coefficient, or the imaginary part of the index, which changes the real part of the index by the Kramers-Kronig relation. The first effect is the filling of the conduction and valence bands, which reduces the index at the wavelengths of interest. The second comes from the free carriers producing a screening effect that reduces the bandgap and increases the refractive index at the wavelengths of interest. The final effect is the free carrier interaction with the optical field which reduces the index. The net effect depends on the total carrier concentration.

In the presence of gain material, or quantum wells, the junction is typically designed such that the QWs are embedded within a double heterojunction to trap the carriers and increase recombination current in the junction. From the perspective of generating net positive optical gain in the laser cavity, the double heterojunction provides confinement of the carriers that helps achieve population inversion where there are more carriers in the higher energy state of interest compared the lower energy state of interest.

### ***Reverse Bias Operation***

When a negative bias is applied to a PN junction, the barrier to thermally injected carriers is increased leading to minimal current. In practice, current is dominated by imperfections of the device sidewall passivation. If photons with energy greater than the bandgap the junction, they produce electron hole pairs that are swept out of the junction by the built-in and applied electric field. This provides a mechanism for detection of optical signals from both external sources in the case of discrete diodes and on-chip sources in the case of PICs. In this thesis, discrete diodes specifically designed for high optical absorption and fast removal of optically generated carriers are discussed for the generation of mmW signals.

## **Uni-Traveling Carrier Photodiodes for mmW Generation**

### ***Device Overview***

Illuminating a PN-junction with photons that have energy that is greater than the bandgap energy generates excess carriers in the junction which are swept out by the electric field. This generates a net current and is the basis for detecting an optical signal. The PN junction can be

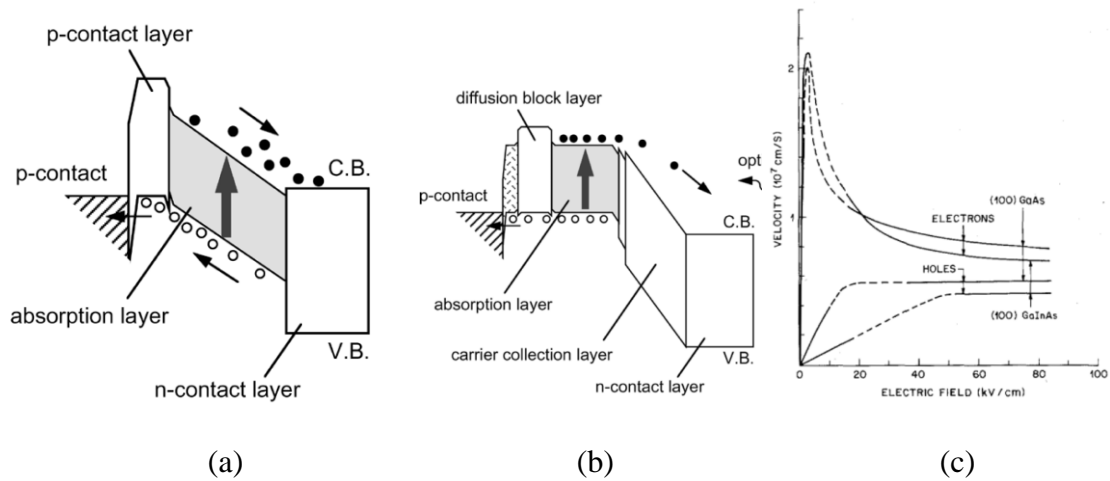


Figure 4 - 3 (a) Band diagram of PIN PD. The absorption region is the full depletion region. Thus both photogenerated holes and electrons are transiting the depletion region and both contributed to the transit-time limited bandwidth. (b) Band diagram of the UTC-PD where the absorption region is fully p-type. Since the photogenerated holes are majority carriers, they respond within the dielectric relaxation time, which is negligible compared to the transit time of the electrons through the depletion region. (a) and (b) adapted from ref. [7] (c) Carrier velocity of electrons and holes in InGaAs and GaAs as a function of electric field. This illustrates that electrons have a higher saturation velocity in these materials and that under low electric fields there is an overshoot velocity that can be exploited by grading the bandgap or grading the doping the absorption layer. Adapted from ref. [8]

engineered such that different sections are made from materials with different bandgap wavelengths to control where light is absorbed. Figure 4 - 3a shows an example of a PIN diode where the undoped, intrinsic region, is made from InGaAs, which as shown in Figure 4 - 1, has the smallest bandgap of the InGaAsP alloy that is lattice matched to InP. This generates the carriers selectively inside the depletion region so that carriers are separated and detected faster than the recombination process happens to maximize the absorption efficiency. A detailed analysis of this shows that the electrons and holes transit at the minority carrier velocity of the material. A typical curve of these velocities vs. field strength is shown in Figure 4 - 3. The electrons velocity is faster than the hole velocity, and the hole will ultimately limit

the frequency response of the device. An alternative approach is to instead, place the InGaAs layer directly adjacent to the depletion region as shown in Figure 4 - 3. In this case, recombination can occur, lowering the efficiency, however when designed properly this can be mitigated. This type of detector is termed the uni-traveling-carrier photodiode as on a single carrier type transits the depletion region. The benefit of this design comes from the difference in the effective mass of the n-type and p-type carriers with the p-type carriers being heavier. This results in different carrier velocities due to the high mobility calculated as  $\mu_n = \frac{e\tau}{m_e^{eff}}$ . The carrier velocity is directly proportional to the mobility. As shown in Figure 4 - 3, the carrier velocity can be much higher for the electrons. The p-type carrier saturation velocity is ~30% lower than the n-type saturation velocity [8]. Thus, by using this UTC design, the p-type photogenerated carriers are majority carriers and do not transit the depletion region. This eliminates a potential bandwidth limiting component and the reduced charge density in the depletion region allows for photocurrents at the same applied bias voltage [9], [10].

There are three important metrics to assess when discussing PD performance: 3-dB bandwidth, efficiency, and maximum power output. The 3-dB bandwidth is a measure of how the power output from the device is reduced as the output frequency is increased. The efficiency of the device is often taken to be the optical absorption efficiency, what fraction of the input light generates photocurrent. From a measurement standpoint, this is the responsivity or current per input power. The two quantities are related by  $R = \frac{e\lambda}{hc}\eta$ , where  $\eta$  is the absorption efficiency. As will be shown, a more important quantity, the power conversion efficiency, is another important quantification of the efficiency [11], [12]. This quantity

includes the electrical power dissipated by the device during operation and is defined by

$$\eta_{PCE} = \frac{P_{RF}}{P_{opt} + P_{Bias}}$$

achieved, defined by  $P_{RF} = \frac{1}{2} R_L I_{RF}^2$ . Here  $R_L$  is the load impedance which is usually 50 ohm and  $I_{RF}$  is the RF photocurrent.

### **Frequency response**

The current at the load that results from the optical generated carriers comes from the displacement field that results at the metal contacts. The generated carriers do not produce a delta function like current, but rather a broadened pulse that integrates to the total charge injection. The width of this pulse is related to the frequency response of the diode and how quickly the carrier moves from the absorption region through the depletion region. This is often discussed as two separate components: the RC limited and transit time limited bandwidth [8], [13].

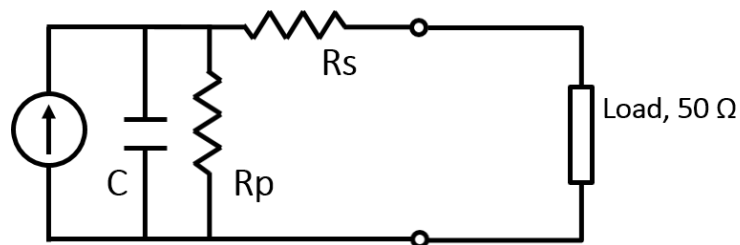


Figure 4 - 4 Standard circuit model for a diode under reverse bias.

The RC limited bandwidth is explained from view the PD as a simple circuit. The circuit model for an ideal reverse biased diode is shown in Figure 4 - 4. The inclusion of the AC

current source accounts for the optical generation of carriers and thus allows a simple expression to be made for the power delivered to the load as a function of frequency. The transfer function for this circuit is

$$H(\omega) = \frac{I_{RF}(\omega)}{I_{ph}(\omega)} = \left[ 1 + j\omega C_j(R_s + R_L) + \frac{R_s + R_L}{R_p} \right]^{-1}$$

Under the assumption that  $R_p \gg R_s + R_L$ , this is simplified to

$$H(\omega) = \frac{1}{1 + j\omega C_j(R_s + R_L)}$$

This is justified by noting that typical values for  $R_s$  and  $R_L$  are around  $10^1$  to  $10^2$ , while values for  $R_p$  are around  $10^5$ . This model works quite well for devices that are designed to operate around 10 GHz to 50 GHz, however, as devices move toward the high end of the mmW spectrum, parasitic components play a dominant role in the frequency response and become difficult to model. The transit time limited bandwidth is more complicated and can be understood by applying the drift-diffusion equation and is discussed in detail in Ref. [13]

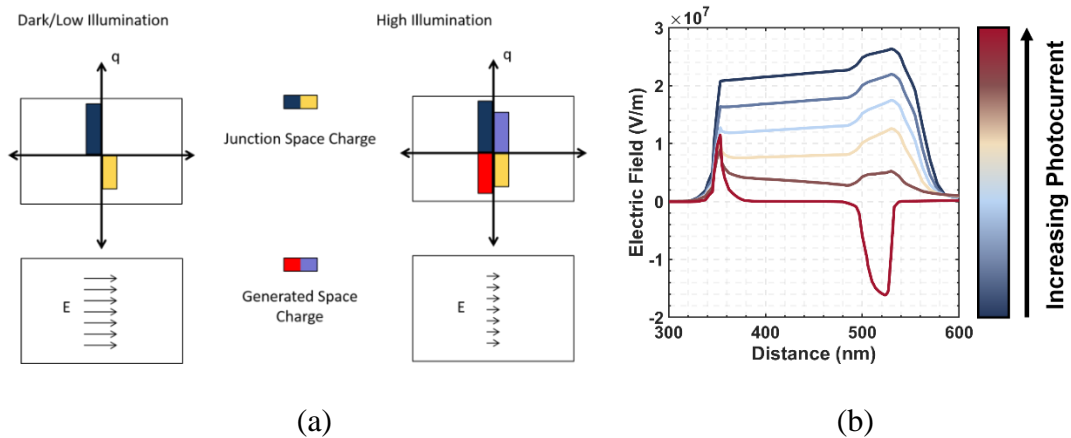


Figure 4 - 5 (a) Schematic of the ion distribution and electric field within a PN-junction under equilibrium (left) and when a large photocurrent is generated (right). The net electric field is reduced as a result of the electric field due to the free carriers. (b) Simulation in Lumerical DEVICE showing this effect in a UTC-PD as the photocurrent generation rate is increased.

### ***RF Output Power***

In the application of generating mmW signals, the desired output is high RF power. As mentioned above, the RF power is proportional to the square of the RF photocurrent. Using a simple analysis from Ch. 2, we can assume that the total photocurrent is

$$I_{ph} = \overline{I_{ph}} + m\overline{I_{ph}}H(\omega) \cos(\omega t)$$

where  $H(\omega)$  accounts for the frequency response of the device. This expression is valid if the output power is below the onset of compression. Compression occurs when the device output power no longer follows the scales quadratically with input optical power. Instead higher order harmonics are generated, and the fundamental frequency rolls off. This generally happens when optically generated carrier builds up in the depletion region and reduce the electric field below the threshold value for operation as shown in Figure 4 - 5. This is referred to as the space-charge effect. A simple model for this is given in the following section where the bias voltage expressed as a function of the photocurrent and effective resistance that reduce the effective bias voltage of the junction.

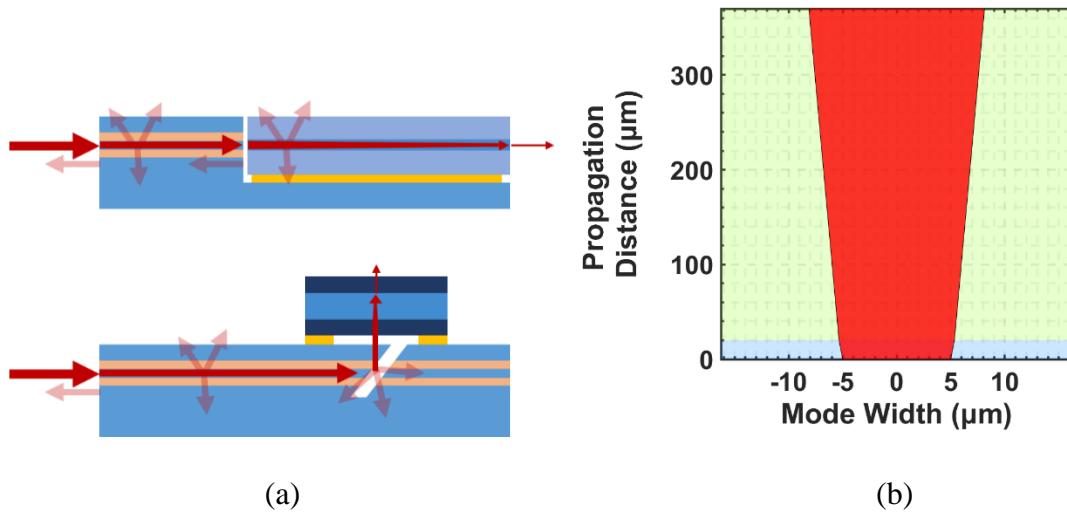


Figure 4 - 6 (a) Diagram of two different kinds of hybrid integrated between different photonic platforms. In the top case, butt coupling is used, which has reflections from the interface in addition to the passive waveguide loss. In the bottom case, a total internal reflection turning mirror is used and the PD is bonded on top of the turning mirror. This has scattering loss at the mirror and well as diffraction loss as the mode propagates toward the absorption layer. (b) Example of mode diffraction as it propagates through the InP epitaxial layers. The calculation assumes the first 20 um are Si cladding form a SiPh chip while the remaining material has the index near InP ( $n = 3.16$ ).

### ***Efficiency***

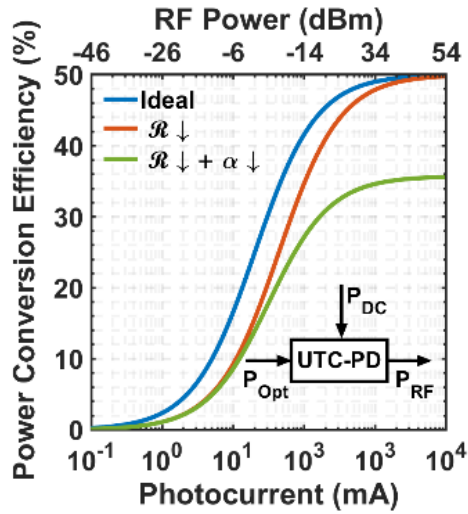
The efficiency of a photodiode can be discussed in two parts: first the optical absorption efficiency and second, the power conversion efficiency. The optical absorption efficiency is simply the percentage of light incident on the PD that contributes to photocurrent. Figure 4 - 6 illustrates sources loss that reduce the optical absorption efficiency for both surface illuminated and waveguide input photodiodes. For surface illuminated devices, the light propagates perpendicular to the material growth direction, and so the absorption efficiency is tied to the thickness of the absorbing layer by

$$\eta \propto 1 - e^{-\Gamma\alpha L}$$

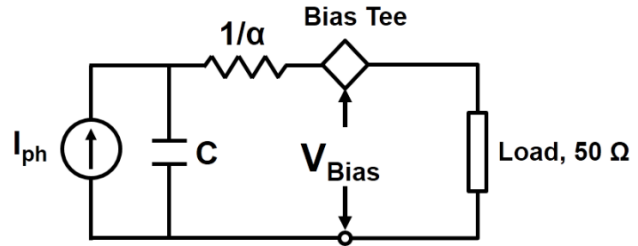
where  $\Gamma$  is the overlap of the free space mode with the diode active area,  $\alpha$  is the absorption coefficient, and  $L$  is the absorption region thickness. The proportionality constant depends on reflections at the interfaces and recombination of photogenerated carriers before they are swept out of the absorbing layer. For waveguide-based devices, the efficiency expression is the same, however, the confinement factor is the overlap of the waveguide mode with the absorbing layer and  $L$  is the propagation length. Compared to surface illuminated devices, the confinement factor is much smaller, and dependent on the waveguide cross section geometry. Furthermore, the propagation length and the absorbing layer thickness are independent which gives additional design optimization to decouple absorption efficiency from the bandwidth.

The power conversion efficiency is calculated from optical and electrical energy balance as illustrated in inset of Figure 4 - 7a, where the efficiency is defined as  $\eta = \frac{P_{RF}}{P_{DC} + P_{opt}}$  [14], [15]. The power input into the device is both the modulated optical signal power and the DC electrical power necessary to maintain the voltage drop across the p-n junction at a given photocurrent. As described in reference [14], the simple circuit model of a photodiode, shown in Figure 4 - 7b, can be used to express the bias voltage for maximum efficiency as

$$V_{Bias} = V_{th} + \left( \frac{1}{\alpha} + R_L \right) \max(I_{ph}^{RF}) + \frac{I_{ph}^{DC}}{\alpha}$$



(a)



(b)

Figure 4 - 7 (a) Plot showing the net power conversion efficiency of photodiodes for generation of RF power as a function of input photocurrent. The blue curve shows an ideal device with 100% absorption efficiency (responsivity of 1.24 A/W at 1550 nm wavelength) and no series resistance. The orange curve is for a device with reduce absorption efficiency of 50% and the green curve is for a device with 50% absorption efficiency and a series resistance of 20 ohm. The inset shows the block (b) Effective circuit model used to incorporate the required increase in bias voltage calculate with increasing optical power in the power conversion efficiency.

where  $V_{th}$  is a minimum voltage intrinsic to the device that must be maintained across the junction for high frequency operation,  $\frac{1}{\alpha}$  is an effective series resistance which will be discussed in more detail in section III,  $I_{ph}$  is the DC/RF generated photocurrent, and  $R_L$  is the load impedance. This bias corresponds to the voltage needed to operate just below the onset of RF output compression for a given average photocurrent. This is the most efficient bias point for that photocurrent. The DC power input into the device is  $P_{DC} = I_{DC} \cdot V_{Bias}$ , which is

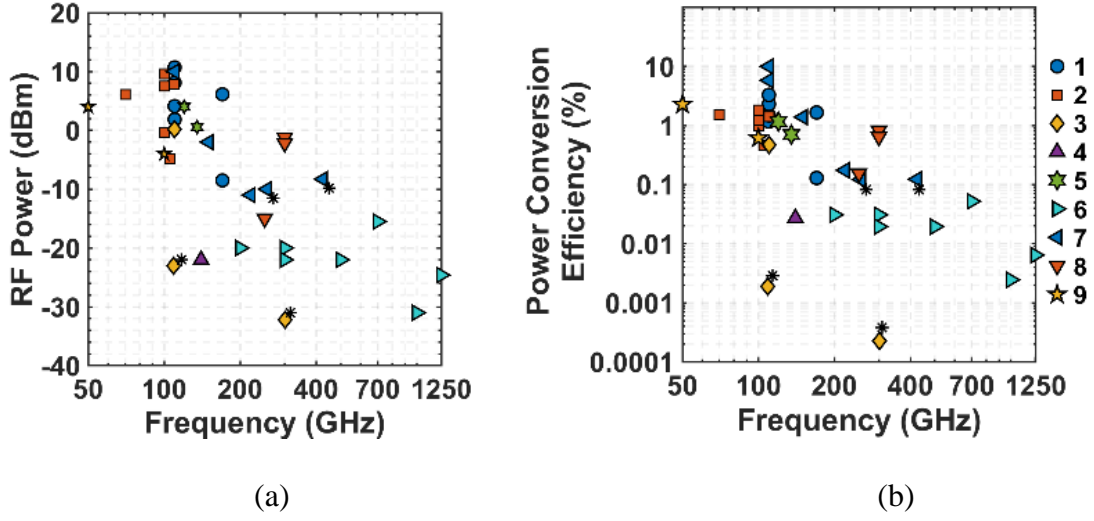


Figure 4 - 8 (a) Plot of results in the literature showing maximum RF output powers demonstrated for a frequency in the mmW and sub-THz regime. (b) Calculated power conversion efficiency from data in (a). References are as follows: Set 1: [16]–[18] Set 2: [19], [20] Set 3: [21], [22] Set 4: [23] Set 5: [24] Set 6: [25], [26] Set 7: [27]–[29] Set 8: [30], [31] Set 9: [32]

proportional to the square of the generated photocurrent. Similarly, the RF power is given by:

$$P_{RF} = \frac{1}{2} R_L (\overline{I_{ph}^{RF}})^2, \text{ where } \overline{I_{ph}^{RF}} \text{ is the RF current amplitude. These two terms contrast the}$$

optical input power  $P_{opt} = \frac{I_{DC}}{R}$ , which is linearly proportional to the photocurrent. This mixed

dependence on photocurrent leads to a nonlinear efficiency curve as a function of photocurrent

as illustrated in Figure 4 - 7a. Following references [12] and [15],  $V_{Bias}$  can be simplified by

assuming  $I_{ph}^{RF} = m I_{DC} \sin(\omega t)$ . The resulting efficiency expression in terms of the power

delivered to the load is:

$$\eta_{RF} = \left( \frac{2}{m} + \frac{2(m+1)}{\alpha m^2 R_L} + \frac{1}{m} \sqrt{\frac{2}{P_{RF} R_L} \left( \frac{1}{R} + V_{th} \right)} \right)^{-1}$$

The limiting value for this expression when the RF power is large is given by  $\eta_{RF} \approx \left(\frac{2}{m} + \frac{2(m+1)}{\alpha m^2 R_L}\right)^{-1}$ . For low values of series resistance, or large  $\alpha$ , the efficiency is simply the modulation index over two. Thus, the most efficient operating condition using a two-laser heterodyne approach is 50% efficiency. As discussed in Ref. [15], higher efficiencies can be achieved using Mach-Zehnder Modulators (MZM) to shape the optical waveform, however, current MZMs are inefficient for frequencies above 100 GHz and this method introduces distortion because of higher efficiency. It is important to note that if the series resistance is low, and the modulation index is  $\sim 1$ , this 50% efficiency point can be achieved regardless of the device responsivity, since the term accounting for the optical efficiency becomes negligible at large photocurrents. This is shown in Figure 4 - 7, along with the effect of increased series resistance and reduced responsivity. In Figure 4 - 7, the blue curve demonstrates the RF power conversion efficiency of an ideal photodiode with zero series resistance ( $\alpha \rightarrow \infty$ ) and responsivity of 1.24 A/W (100% absorption at 1550 nm). The orange curve shows the effect of reduced responsivity,  $\sim 0.5$  A/W. As mentioned previously, the required load power to obtain high efficiency is increased relative to the first case, however, the conversion process can still obtain 50% efficiency at photocurrents. The green curve shows the effects of finite device series resistance relative to the orange curve demonstrating a reduction in the maximum efficiency that can be achieved.

## **Challenges of monolithic integration**

The challenge of integrating multiple devices on a single platform arises from the different optical and electrical requirements. For example, including a semiconductor optical amplifier

(SOA), laser gain element, or a photodiode (PD) requires the material to provide the proper energy levels for the emission or absorption of photons that are of interest. However, any passive element will suffer as the unpumped material will absorb any light that is guided through it. In addition, the interface between different device types can cause optical reflections or loss due to the sudden change in the index seen by the optical mode. Several approaches to this are summarized by others at UCSB [33]–[36].

In designing our UTC-PD with the intent of coupling to a SiN platform, we had to design for the performance requirements of the device and furthermore, the epitaxial layers had to be compatible with a passive waveguide that couples well to the optical mode of the SiN platform from Lionix [37]. Thus, the design process required an iterative approach to balance the requirements.

As shown in Figure 4 - 8, a large body of literature is available on high speed photodiodes which acts a starting point to device design. The design used in this thesis includes a passive waveguide layer consisting of InGaAsP with a bandgap wavelength of 1.26  $\mu\text{m}$ . Above this layer is the InP collector, followed by a grading from InP to InGaAs which is used as the absorbing layer. The InGaAs is then graded back to InP which acts to block diffusion of n-type photogenerated carriers towards the p-contact. Finally, an InGaAs layer is used as a p-contact.

Optical simulations were used to choose the thickness of these layers along with results from literature to act as a guide. Based on results in the literature, the total thickness of the InP collector and InGaAs absorbing layer were constrained to be around 250 nm. The tradeoff between the layers determines the absorption efficiency and RC limited capacitance as the InP

collector thickness determines the junction thickness. Implementing the passive waveguide below with a thickness around 300 nm and waveguide width in the range of 1  $\mu\text{m}$  to 3  $\mu\text{m}$ , gives a starting point around which to optimize the geometry. The general epitaxial structure is shown in Figure 4 - 9 with the layer labels used in the following discussion.

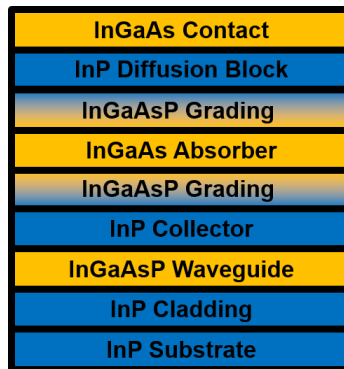


Figure 4 - 9 General epitaxial structure of the photodiode in this work. The structure is grown on a semi-insulating InP substrate starting with a 2  $\mu\text{m}$  n-type InP cladding layer which is also used as the n-contact. Next is a 325 nm n-type InGaAsP waveguide layer followed by an UID 180 nm InP layer that serves as the depletion region or collector. The InP is graded to the 340 nm InGaAs absorbing layer which has p-type doping grade. The InGaAs is graded back to a 1  $\mu\text{m}$  p-type InP layer to block diffusion of photogenerated electrons towards the InGaAs p-contact that terminates the structure.

### ***Passive Waveguide Design***

The designs of the active and passive sections are strongly dependent on one another, and while the simulation and design were iterative, we present first the passive waveguide design. The general geometry chosen is a buried InGaAsP waveguide to match the roughly elliptic mode of the SiN OBFN PIC, which is shown in Figure 4 - 10a. In order to match this mode for efficient butt coupling between the two chips, a similar mode in InP is desired. To achieve this, a buried InGaAsP waveguide geometry is used as shown in Figure 4 - 10b. The passive

waveguide is designed to achieve high coupling efficiency between both the SiN PIC and the active waveguide UTC-PD. The composition was set during the design of the active section to give a bandgap wavelength of  $1.26\ \mu\text{m}$ .

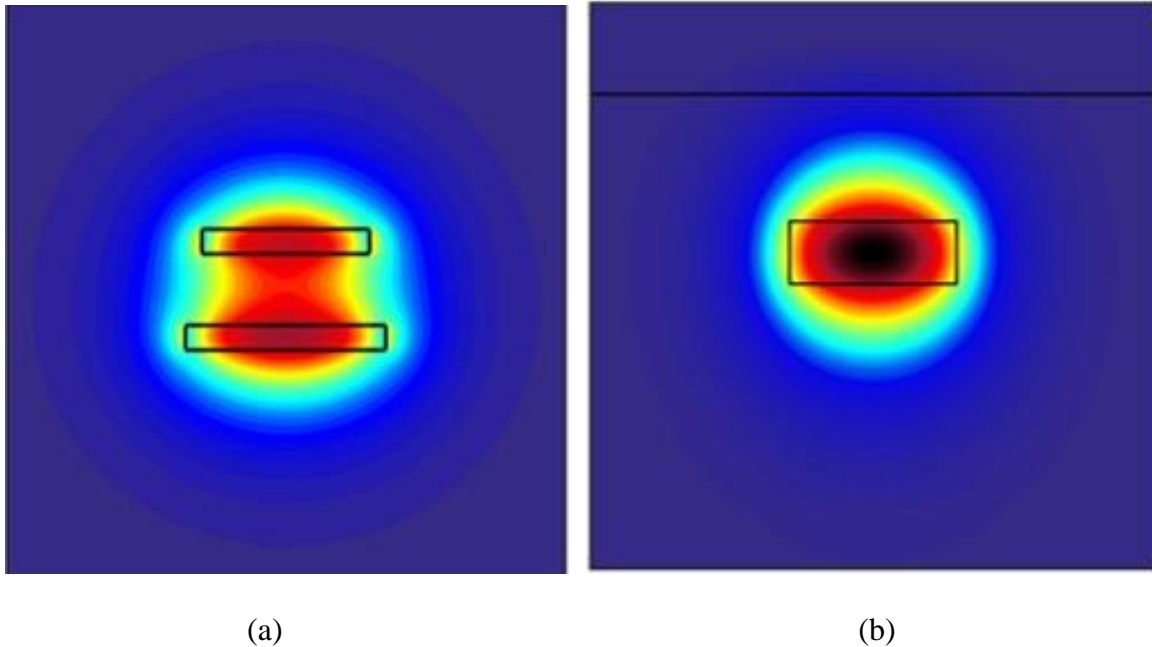


Figure 4 - 10 (a) Mode simulation of the SiN platform that the OBFN PIC used from Lionix. The two waveguide layers are  $120\ \text{nm}$  thick with  $1\ \mu\text{m}$  spacer between them. The top waveguide is  $1\ \mu\text{m}$  wide while the bottom is  $1.2\ \mu\text{m}$  wide. (b) Mode simulation of the InP/InGaAsP buried waveguide structure used for efficient coupling between the SiN platform and the WG-UTC-PD. The final structure is  $325\ \text{nm}$  thick and  $1\ \mu\text{m}$  wide.

There are three design parameters for the passive waveguide: waveguide width, waveguide thickness, and cladding thickness. The cladding thickness affects the overlap very little, but the effective index of the mode is sensitive to the thickness below  $1\ \mu\text{m}$  as shown in Figure 4 - 11a so the thickness was chosen to be  $1\ \mu\text{m}$ . Figure 4 - 11b shows the mode overlap with the SiN waveguide as a function of waveguide width and thickness. As shown, the overlap, and hence coupling efficiency, is best for around  $200\ \text{nm}$  waveguide thickness and  $1$

um width. However, the transition between the passive and active sections of the PD set a limit on the minimum waveguide thickness of 300 nm due to the cutoff wavelength at certain points in the transition.

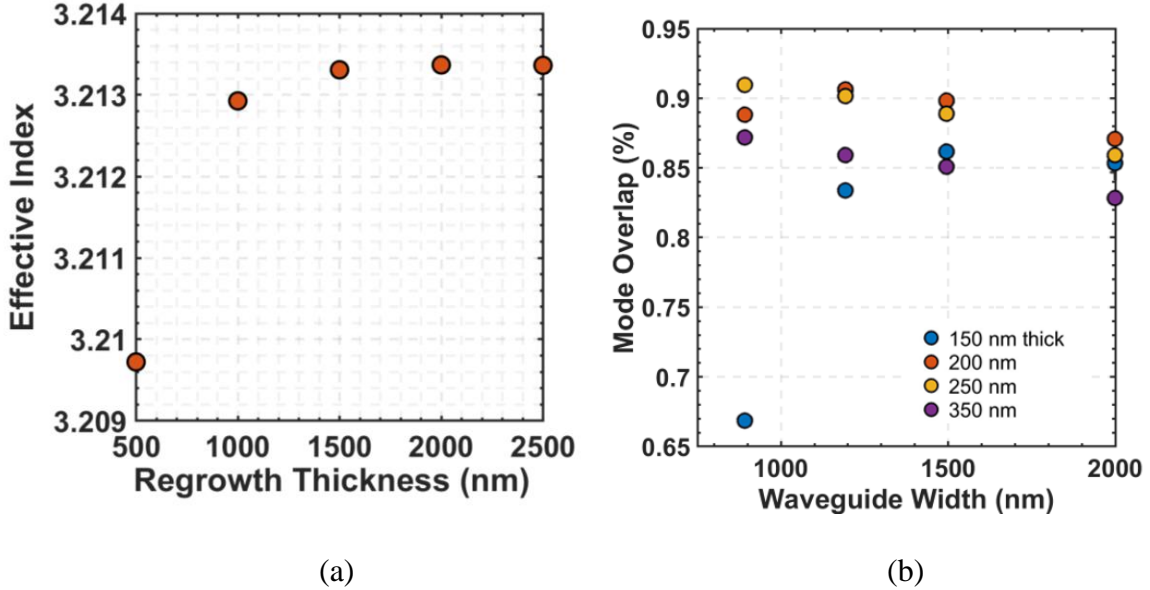


Figure 4 - 11 (a) Simulations of the effective index vs. the regrowth thickness. The effective index becomes insensitive to cladding thickness above 1000 nm. (b) Mode overlap between the SiN waveguide buried passive waveguide and the buried passive waveguide shown in Fig. XX as a function of the buried waveguide width and thickness parameters.

Another metric used to guide the design, is the sensitivity of the coupling to misalignment of the two waveguides. Alignment sensitivity is greatly improved by expanding the modes of both waveguides. However, this was not possible for the SiN PIC due to foundry constraints. Figure 4 - 12 shows coupling as a function of the offset in both the x and y directions. Figure 4 - 10b shows the mode simulation of the final design using a 325 nm thick waveguide layer with a 1  $\mu\text{m}$  width at the input facet.

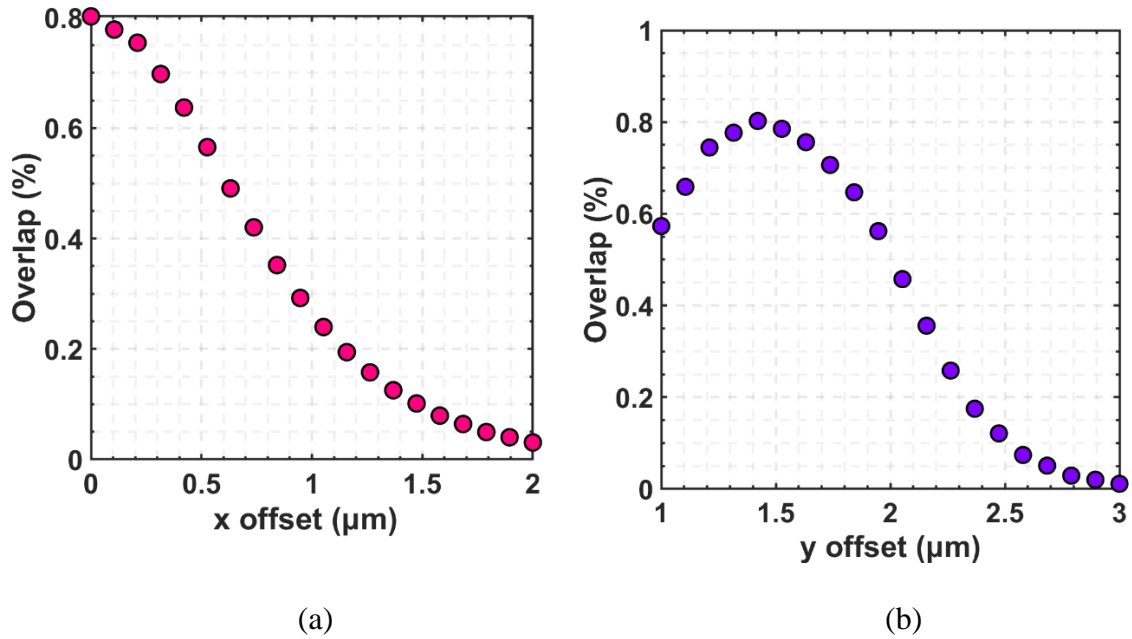


Figure 4 - 12 (a) Mode overlap between the buried waveguide with the SiN waveguide as a function of the offset in the x direction. (b) Mode overlap between the buried waveguide with the SiN waveguide as a function of the offset in the y direction. The buried waveguide has a width of 1  $\mu\text{m}$ , a thickness of 325 nm, and a cladding thickness of 1  $\mu\text{m}$ .

### ***Active Photodiode Waveguide Design***

Optimization of the active sections of the waveguide included varying the collector thickness, absorber thickness, and waveguide ridge width. The responsivity of the device is a function of the mode overlap with the absorber and the propagation length of the device. Given the constraint of the waveguide layer thickness of 325 nm, and the absorber and collector thickness, the overlap is in the range of 5% to 20% depending on the ridge width and absorber thickness. Using an absorption coefficient of  $6500 \text{ cm}^{-1}$ , the length required for 90% absorption of the light is 70  $\mu\text{m}$  for an overlap of 5% and 17  $\mu\text{m}$  for an overlap of 20%. The collector thickness was set to 150 nm and the absorber thickness to 160 nm with a 30 nm

InGaAsP grade on both side of the absorber. The absorber overlap as a function of ridge width is shown in Figure 4 - 13a with mode shown in Figure 4 - 13b for a ridge width of 2  $\mu\text{m}$ .

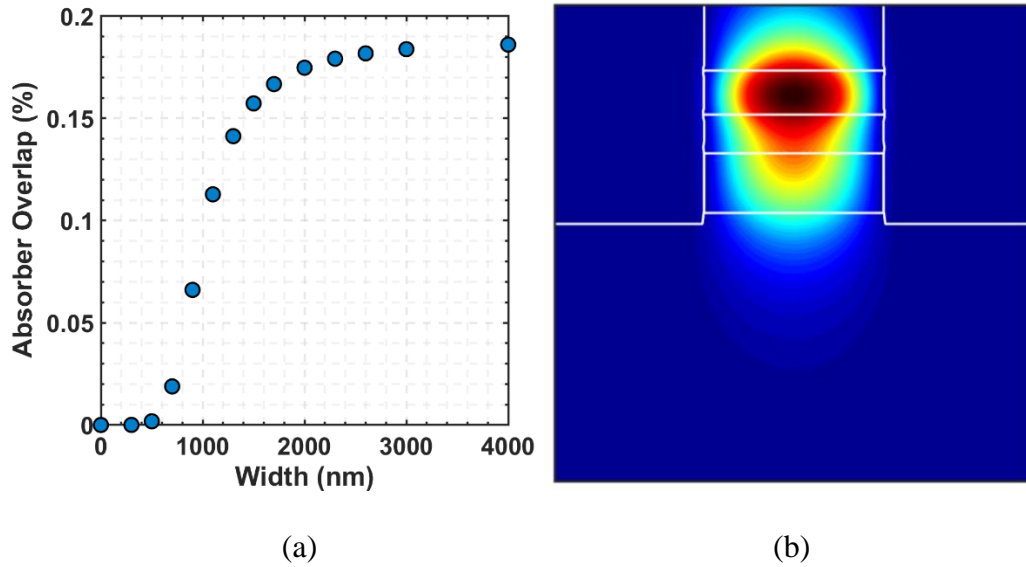


Figure 4 - 13 (a) Overlap of the mode with the absorbing region as a function of the ridge width. (b) Mode simulation for a ridge width of 2  $\mu\text{m}$ .

### ***Passive to Active Transition Design***

The mode conversion from the buried waveguide to the deep ridge WGPD used a multi-taper geometry with the cross sections shown in Figure 4 - 14. Minimizing reflection between the two geometries is achieved by first pushing the mode into the substrate with the InGaAsP layer acting as a waveguide as shown in Figure 4 - 14a-c. This is achieved by simultaneously tapering the buried waveguide width from 1  $\mu\text{m}$  to 5  $\mu\text{m}$  and tapering the top cladding layer taper from 2  $\mu\text{m}$  to 500 nm. Once the mode is confined primarily in the substrate, the active region can be introduced without significant reflection. The active layers are tapered from 500 nm to the desired final width.

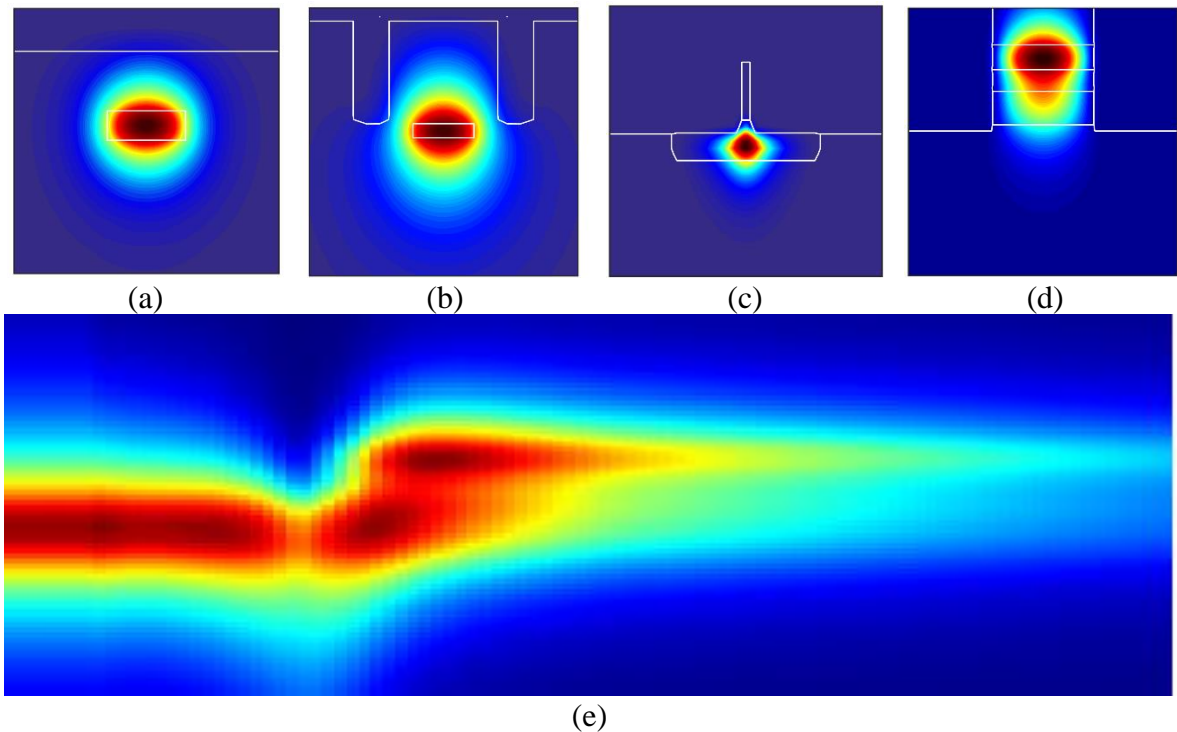


Figure 4 - 14 Mode simulations of transition from the buried waveguide to the WG-UTC-PD. The buried waveguide (a), is gradually converted to a surface ridge waveguide by simultaneously etching a double trench over the waveguide and making the waveguide layer wider (b) until there is only a narrow ridge  $< 1 \mu\text{m}$  and the waveguide is around  $5 \mu\text{m}$  wide (c). The UTC-PD layers are then added on top of the waveguide, and the ridge is tapered out to the desired width (d). (e) Cut through the plane of symmetry of the spot size converter and UTC-PD showing the mode being pushed into the substrate before being brought up into the active layers where the intensity is reduced as the power is absorbed.

Simulation were completed to assess the transmission efficiency as a function of length. As shown in Figure 4 - 15, the transmission can vary significantly depending on the length of the taper. This is due to the excitation of higher order modes as the waveguide geometry changes. Figure 4 - 16 shows a plot of the number of guided modes for different cladding and waveguide widths along the taper. Using these values to choose the starting and ending widths of the taper gives an efficient transmission value that does not vary significantly with taper length.

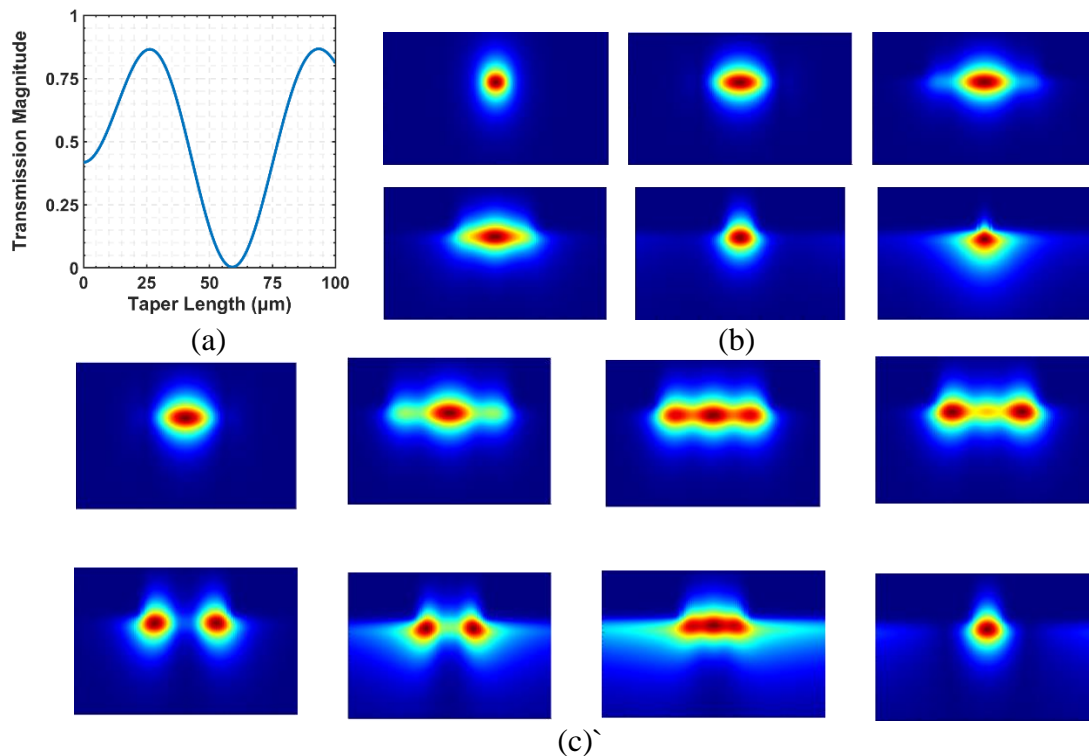


Figure 4 - 15 (a) Plot showing the transmission efficiency as a function of the length of the passive taper. The cause of the large variation in the transmission is shown in (b) and (c). (b) Snapshot of the optical mode for the 25- $\mu\text{m}$  long taper at various positions along the taper illustrating that the light stays in the fundamental mode the entire taper. (c) Snapshot of the optical mode for the 60- $\mu\text{m}$  long taper illustrating that higher order modes are excited throughout the taper reducing the transmission efficiency.

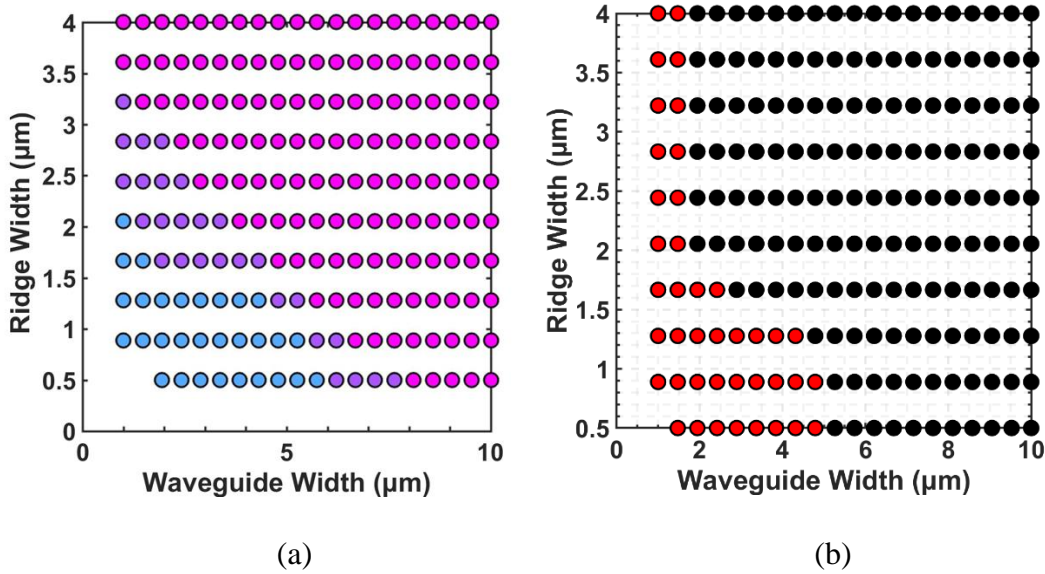


Figure 4 - 16 (a) Number of optical modes supported by the structure as a function of the ridge width and waveguide width for the passive waveguide taper. The light blue signifies only a single supported mode, the purple illustrating two supported modes, and pink supporting three or more modes. (b) Number of optical modes supported by the structure as a function of the ridge width and waveguide width for the active waveguide taper. Red signifies a single supported mode, while black signifies two or more supported modes.

### ***Electrical Design***

The doping within the structure were optimized to increase RF output power and transit time limited bandwidth. For RF output power output, a common approach is to include a highly doped InP layer adjacent to the p-type absorbing region. This increases the electric field of the depletion region close to where carriers are generated as shown in Figure 4 - 17a. This allows for a higher generation rate before the space-charge effect causes saturation of the RF output power. In addition, the band structure of InP/InGaAsP is such that the electron velocity is non-monotonic with regard to the electric field. As shown in Figure 4 - 3, the velocity of the carrier

reaches a maximum around 10 kV/cm, and saturates at a value 50% lower than the maximum value. While the absorbing layer is not depleted and p-type, a grading of the doping can provide a residual electric field that is around the maximum velocity as shown in Figure 4 - 17. This overshoot velocity then provides the carriers with a lower transit time and increases the maximum achievable bandwidth. The final design is shown in in Fig. XX with the composition and doping levels of each layer.

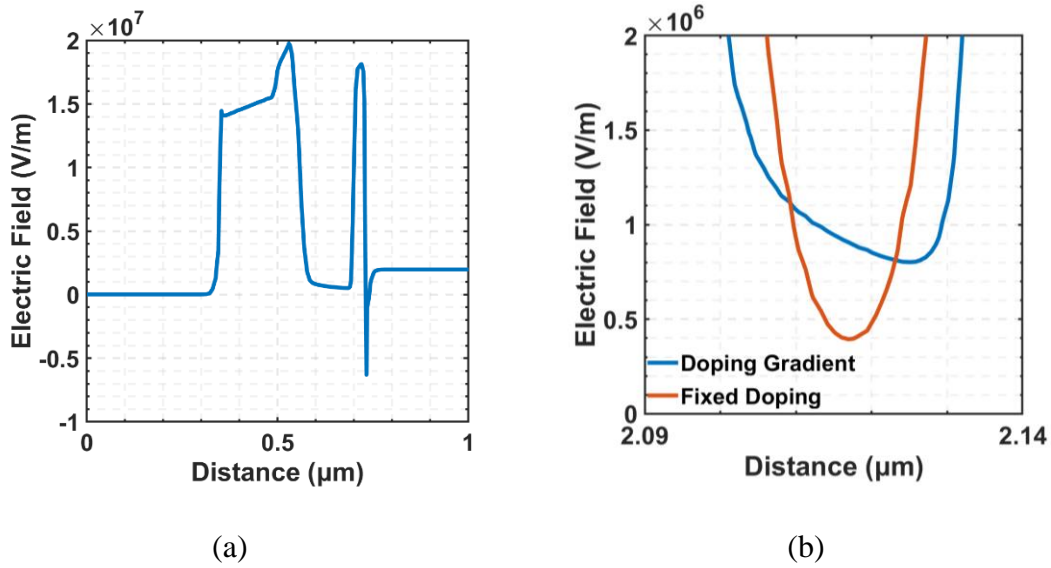


Figure 4 - 17 (a) Simulation of the electric field in the device. The regions of high electric field are the collector and the between the InGaAs/InP interface. (b) The electric field in the absorber with and without the doping gradient showing the increase in the electric field which put the electric field in the overshoot regime.

## Fabrication of InP/InGaAsP Devices

Fabrication of semiconductor devices constitutes the most challenging aspects of implementing designs for high speed transceivers. While optimization of the optical and electrical properties can be achieved during the modeling and design phase, practical

limitations in fabrication and layout can make realization very difficult. In the following section, I will summarize the basics of InP processing and fabrication, as well as, key challenges that were encountered and overcome while making the UTC-PDs that have been discussed.

## **Overview**

Fabrication can be broken down into essentially three components: depositions, patterning, and etching. During deposition steps material is added to the wafer, such as the epitaxial stack for the device operation, dielectrics for masking etches or surface passivation, or metals for contacting the devices. The patterning steps imprint a 2D image onto the surface which are used to create the desired 3D geometry. Lastly, etching removes material to transfer the 2D pattern into the wafer. When fabricating photonic devices, selection of the materials deposited and etches chemistries used will ultimately determine if the fabrication is successful and if device performs properly. Therefore, I will take some time to lay out the decision-making process for achieving certain design parameters.

### ***Masking***

The first topic to be discussed is masking, which falls under the deposition category. The first step in many of our processes is deposition of a dielectric etch mask. This is most commonly PECVD SiN or SiO<sub>2</sub>, each of which has benefits and drawbacks depending on the etching to be used. Table 2 illustrates the key differences between these two materials when used in semiconductor processing. For InP, surface preparation is important to ensure a smooth film is deposited. The standard process followed for deposition of SiN or SiO<sub>2</sub> in

PECVD 1 is first a standard clean of acetone and iso-propyl alcohol. The sample is dried with pressurized N<sub>2</sub> and baked at >100C to further remove any solvents. Next, an O<sub>2</sub> cleaning step is used, either PE-2 100 W plasma clean for 30" or a UV-O<sub>3</sub> clean for 5'. This step depends if the exposed surface will be used for metal contacts or regrowth of additional semiconductor material. In the case of either a surface for metal contact or regrowth, UV-O<sub>3</sub> is preferred due to the damage caused to the surface by the O<sub>2</sub> plasma which increases contact resistance for metal contacts and reduces film quality for regrowth. Following the O<sub>2</sub> surface clean, the wafer is submerged in buffered hydrofluoric acid (BHF) for 30" then rinsed in DI water for 2' and dried in N<sub>2</sub>. The sample should then be immediately loaded into the deposition chamber to ensure a clean surface. The purpose of the O<sub>2</sub> cleaning steps is to ensure that the polarity of the surface of the semiconductor wafer is matched to the polarity of BHF. Figure 4 - 18 illustrates the film quality of SiN on InP with and without the O<sub>2</sub> cleaning step. As shown, without an O<sub>2</sub> clean, the deposition generates particle growth on the surface of the dielectric. This is due to incomplete wetting of the surface while submerged in BHF, leaving unpredictable residual oxides on the surface of the wafer. This effect is not as pronounced with SiO<sub>2</sub> films, but it is recommended to follow the procedure regardless.

Following the dielectric deposition, the surface is coated with a photoresist (PR) that when exposed to UV light either becoming soluble or insoluble in a developer. Using a mask to selectively block the UV light generates the 2D image that is formed after developing the photoresist. The photoresist then acts as an etch mask or deposition mask for the next step.

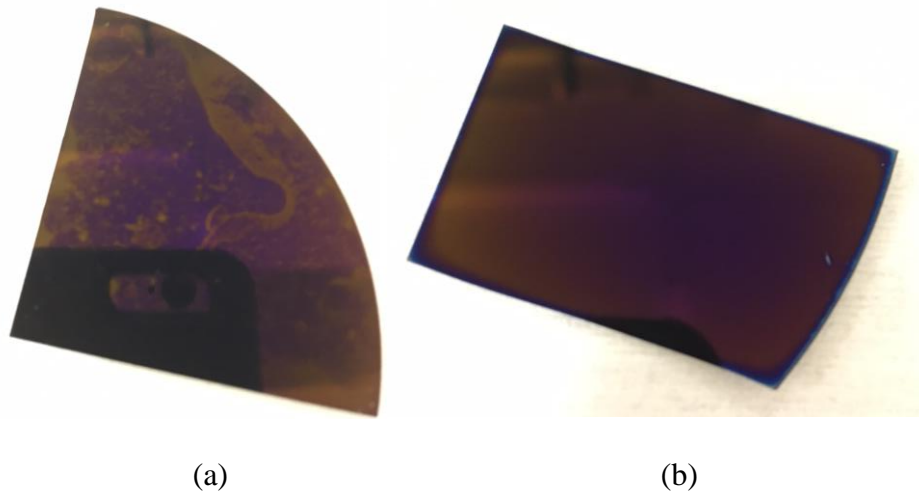


Figure 4 - 18 (a) Optical image of Si pieces after deposition of 200 nm of SiN using PECVD 1 with only a 30s BHF dip prior to deposition. (b) Si piece with a 30s PE-II O<sub>2</sub> plasma etch followed by 30 BHF dip prior to SiN deposition in PECVD 1.

**Table 2 Comparison of dielectric etch masks**

Processing Aspect	SiN	SiO <sub>2</sub>
Strain	Tensile	Compression
Sidewall passivation	Better	OK
Metal adhesion	Best	OK
Wet Etching	Best	Poor due to compressive strain causing delamination
ICP 2 Etch Rate	~ 200 nm/min	~80 nm/min
RIE 2 Etch Rate	~ 0 nm/min	~0 nm/min
Unaxis ICP Etch Rate	~500 nm/min	~100 nm/min

Selection of the photoresist is critical to achieving the desired resolution and properly masking all the features that are not part of the next deposition or etch step. In general, for higher resolution of smaller features, thinner photoresists are needed. However, the photoresist thickness needs to be larger than the tallest feature that exists of the wafer, otherwise the edges of the features will contain a thinner layer of photoresist and may not

properly mask the material from the next step. This is shown in Figure 4 - 19. The thickness of the photoresist is controlled by picking the proper formulation and using the spin speed-thickness curve from the data sheet to achieve the desired thickness. During the fabrication of the devices discussed in this thesis, thickness and resolution became competing requirements, and a bi-layer process was developed to achieve good resolution on a non-planar surface. This will be discussed in a later section.

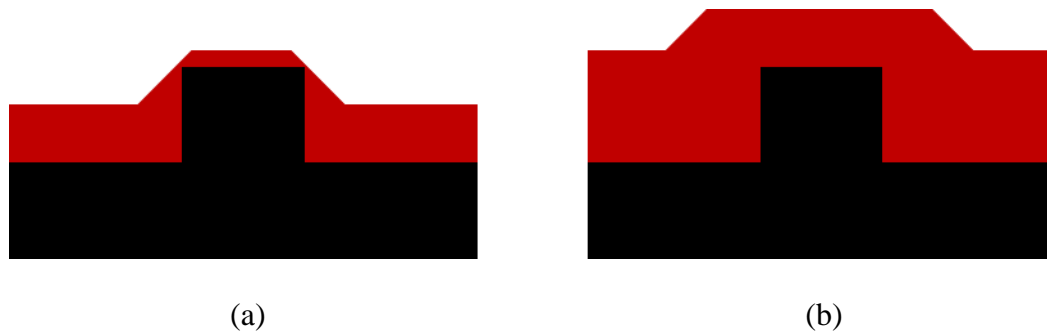


Figure 4 - 19 (a) Diagram showing how photoresist covers a mesa when the mesa is taller than the nominal thickness of the photoresist illustrating the thin coverage at the etch of the mesa. (b) Photoresist coverage when the nominal thickness is greater than the height of the mesa, illustrating complete coverage of the mesa.

The PR is exposed using one of the lithography systems in the cleanroom. While the PR and thickness of the PR ultimately limit the resolution of the pattern, the exposure dose (time) needs to be optimized to achieve this resolution. Depending on whether the features are openings in an otherwise unexposed field or mesas in a field that was completely exposed, the exposure time needs to be adjusted. This means that while a PR formulation can achieve certain resolution, it is unlikely it for it to achieve that resolution for both mesas and holes at the same time. This needs to be accounted for during the layout and mask design phase.

Generally, holes in unexposed regions need longer exposure times than mesas in exposed regions for positive photoresists.

If the photoresist is going to be used to lift-off metal, either a bi-layer process or a negative resist needs to be used. During exposure, the top of the PR gets a larger dose of light, causing slight over-exposure. For a positive PR, this makes the sidewall slightly slanted away from the exposed region, while for a negative PR, this makes the sidewall slant toward the exposed region, undercutting the unexposed regions. Thus, when a metal is deposited on a positive PR, the sidewall gets covered as well and it will be difficult for the stripping agent to remove the PR. On the other hand, for a negative PR, the sidewall is shadowed by the top surface leaving a gap in the metal which allows the stripping agent to dissolve the PR relatively easily. Using a bi-layer process, or lift-off layer, allows one to do metal lift-off with a positive PR. The lift-off layer is essentially a second PR layer underneath the first that develops faster than the top layer. This creates a gap in the sidewall where the metal deposition will not connect allowing for the stripping agent to dissolve the PR. The thickness of the lift-off layer must be chosen so that the metal deposited does not bridge the gap which is typically 1.2x to 1.5x the desired metal thickness. The degree of undercut depends on the formulation of the underlayer and the baking temperature of the lift-off layer.

After exposure the wafer is baked and submerged in a developer that selectively dissolves the exposed region of the PR (for negative PR it dissolves the unexposed region). This generates the mask pattern on the surface of the wafer and completes the masking of the surface. From this point, the regions of the surface that are not covered by PR can be etched or additional materials can be deposited on them.

## Wet Etching

The first type of etching used in semiconductor processing is wet chemical etches. This is typically an acid or base mixture. Table 3 highlights the common wet etches used for the devices described in this thesis.

**Table 3 List of wet chemical etches**

Etch Formula	Description
HCl:H <sub>3</sub> PO <sub>4</sub> ::1:3	Used for selectively etching InP (does not etch As containing alloys). Preferentially etches 011 crystal surfaces leaving smooth sidewalls.
H <sub>2</sub> SO <sub>4</sub> :H <sub>2</sub> O <sub>2</sub> :H <sub>2</sub> O::1:1:10	Used to selectively etch InGaAs(P) (etch rate reduces with increasing P content). Etches isotropically
BHF	Etches SiO <sub>2</sub> and SiN dielectrics. Also used for surface cleaning of InP epi material
HCl:H <sub>2</sub> O::1:10	Removes surface oxides from InP epi material
NH <sub>4</sub> OH:H <sub>2</sub> O::1:2-10	Removes surface oxides from InP epi material

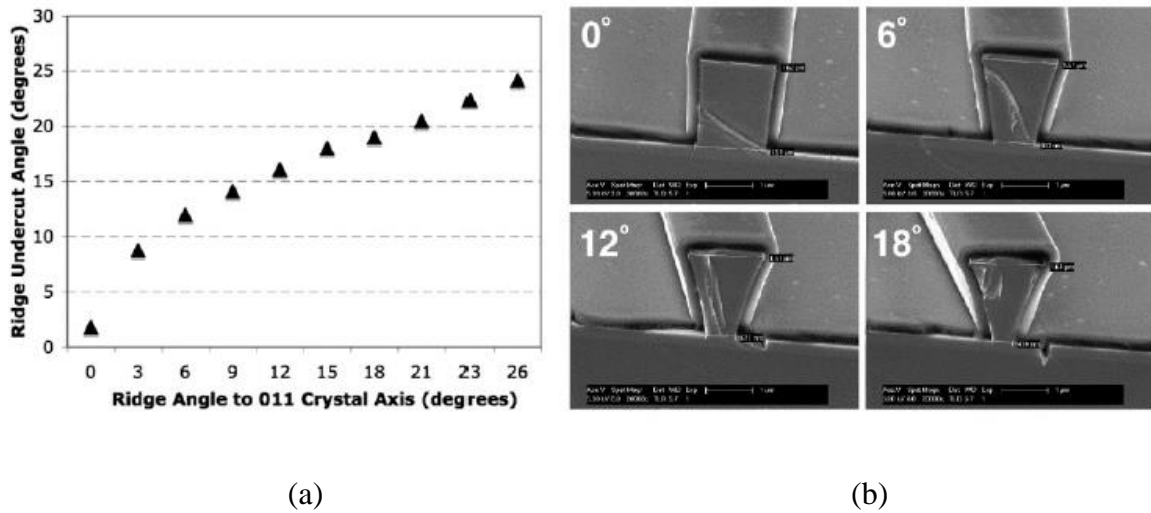


Figure 4 - 20 (a) Ridge undercut for HCl:H<sub>3</sub>PO<sub>4</sub> when etching InP as a function of the ridge angle to the 011 crystal axis. (b) Cross section SEM of the ridges etched at different angles. Adapted from Ref [38].

As shown in Table 3, the benefit of using wet etches for the InP/InGaAsP material system is that InP and InGaAsP alloys can be selectively etched in the case of the HCl:H<sub>3</sub>PO<sub>4</sub> etch, the smooth sidewalls. As these are chemically achieved, they do not depend on the ability of the masking process to have smooth sidewalls. The sidewall smoothness is important for PICs with long propagation distances as this sidewall roughness contributes to passive optical loss. However, as this is crystallographic, the waveguide must be aligned the 110 direction. As shown in Figure 4 - 20, waveguides aligned away from this direction show undercut and roughening of the sidewall, and at 45° from this direction the ridge will be completely undercut. For wet etches, the mask can be SiN, SiO<sub>2</sub>, or PR. In the case of PR masks, some amount of undercut is commonly observed, and so this should only be used for non-critical features with high tolerance for fabrication variation. In the case of SiN and SiO<sub>2</sub>, as mentioned in Table 2, SiO<sub>2</sub> often has adhesion issues due to the compressive strain. This is more important for long narrow features such as long passive waveguides. As shown in Figure 4 - 21, the SiO<sub>2</sub> mask layer can “buckle” from the strain so that the underlying semiconductor is exposed and etched. SiN does not suffer from this problem as the tensile strain does not favor buckling to alleviate the strain.

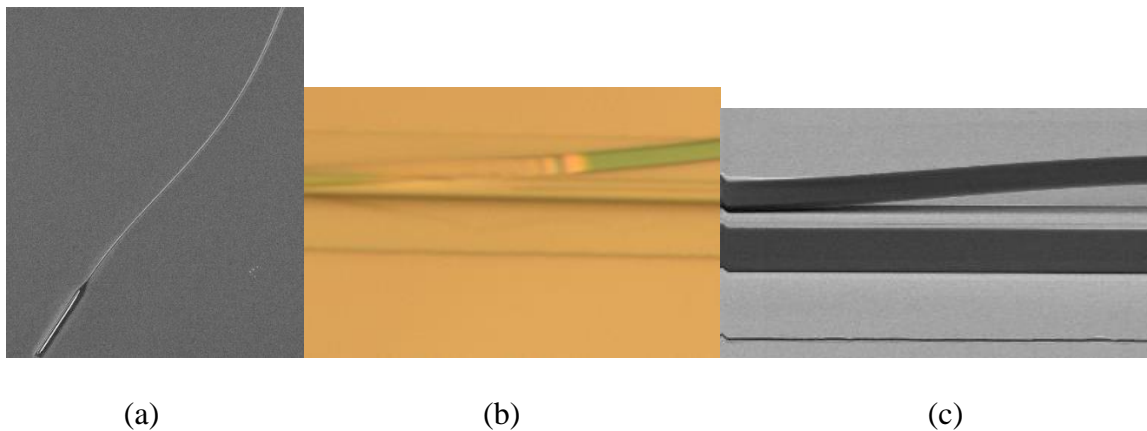


Figure 4 - 21 (a) SEM image showing the SiO<sub>2</sub> hard mask delaminating from InP wafer. The pattern is > 200 μm long and 1 μm wide. (b) Optical and (c) SEM image of similar delamination of SiO<sub>2</sub> masks from InP devices.

### ***Dry Etching***

Dry etching combines gas phase chemicals with plasmas to create an isotropic etch that follows the masking layer.

**Table 4** highlights the commonly used dry etches. Dry etching allows for deeper etching without risk of undercutting small features or faceting caused by some wet etches. The choice of the mask for dry etching depends on the temperature of the etch tool and the selectivity between the etch mask and material being etched. One of the most critical parameters to optimize is the ratio of the chemical component (gas flows and ratios) to the physical component (RF plasma power and bias) of the etch. As shown in Figure 4 - 22, is the case of too high a chemical component, the result is often a “grassy” surface texture. One drawback of dry etches is the potential for loading effects to occur, where the amount of etch surface changes the etch quality, or the etch quality changes over the surface of the wafer.

**Table 4 List of dry etches and their properties**

<b>Etch Formula</b>	<b>Description</b>
CHF <sub>3</sub> :CF <sub>4</sub> :O <sub>2</sub>	ICP-2: Varying ratio of three chemicals allows this to be used for etching SiN, SiO <sub>2</sub> , and BCB
CH <sub>4</sub> :H <sub>2</sub> :Ar	RIE-2: Etch for InGaAsP materials. Etch rate between 90 nm/min and 30 nm/min, with higher etch rate for InP and lower for InGaAsP
Cl <sub>2</sub> :H <sub>2</sub> :Ar	Unaxis-ICP: Etch for InGaAsP materials. Etch rate around 1 μm/min

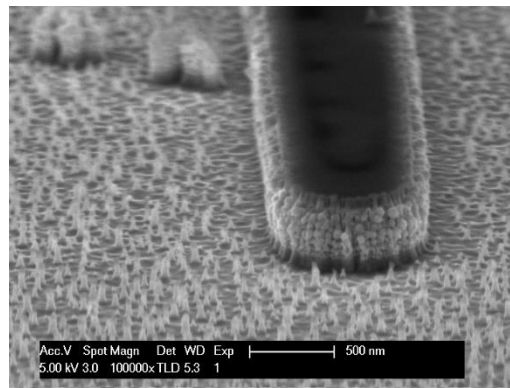


Figure 4 - 22 Example of dry etch when the physical to chemical etch components are unbalanced and the chemical etch component dominates.

### ***Metallization and lift-off***

The process of metallization requires selective deposition of metal over specific regions. While it is possible to deposit metal over the entire surface and dry or wet etch the unwanted regions, this is usually too aggressive and undesired. The process used here is the bilayer process described above, where the an underlayer is included under the photoresist to create a break in the deposited metal. The break in the metal allows strippers to reach the photoresist and lift-off the metal that is deposited on top, leaving metal on the sample where the photoresist was developed away. It is critical for device reliability that the metal is continuous

on mesa sidewalls. This is achieved by angled deposition with continuous rotation of the sample.

## Photodiode Fabrication

### *Active Region Definition*

The active layers of the photodiode include the InGaAs absorbing layer and the InGaAsP bandgap grading layers. These layers had to be selectively removed from most of the wafer to eliminate excess loss of the passive waveguides. Initially, this was done using a combination of dry and wet etching. However, as shown in Figure 4 - 23 the small area of the active regions led to significant undercutting of the mesas in some cases, complete removal of the mesas. Even in the as case where the mesa is not completely removed, the undercut contributes to excess series resistance which will ultimately limit the bandwidth of the devices. In the second and subsequent generations only a dry etch in RIE-2 was used, which resulted in some etch depth variation between samples.

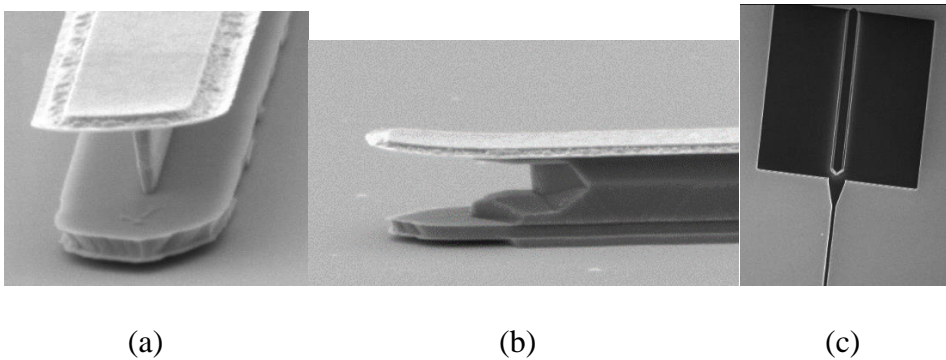


Figure 4 - 23 (a) and (b) SEM of narrow mesas formed by wet etching using HCl:H<sub>3</sub>PO<sub>4</sub> showing the formation of facets at the start and end of the mesas leading to severe undercut of the mesa. (c) Plan view SEM of the active mesa and passive waveguide etch.

### ***Passive Waveguide Etch***

The second step in the fabrication was etching of the passive waveguide. The waveguide layer is a quaternary alloy with an InP cap layer. The InP cap layer, which also serves as the collector, prevent As and P outgassing during regrowth. The waveguide layer etches well with H<sub>2</sub>SO<sub>4</sub>:HO:DI mixture from Table 3, while the InP cap layer can be quickly etched with the HCl:H<sub>3</sub>PO<sub>4</sub> mixture. A dry etch can be used initially, however, the issues with undercut were not as pronounced in this step. Due to the high aspect ratio of the passive waveguide (~1 um x 500 um) it is critical to use a SiN hardmask to eliminate the delamination problem described earlier. A microscope image the sample post wet etch is shown in Figure 4 - 23c.

### ***Regrowth***

The next step in the fabrication process is regrowth of a 1 μm InP cladding layer which forms the buried passive waveguide. The two previous processing steps finish with wet chemical etches which prevents plasma damage at the surface. The plasma damage has been correlated with polycrystalline growth and defects at the growth interface, which can lead to additional scattering loss or non-radiative recombination sites. Prior to regrowth the sample is completely stripped of any dielectric using BHF. The sample is placed in a UV-O<sub>3</sub> reactor for 1 hour to create a thin oxidation layer. Immediately before loading the sample into the MOCVD reactor, at 30 second BHF etch is completed and the sample is dried in N<sub>2</sub> before being loaded for growth.

Regrowth has generally been completed successfully in the past over 100 nm to 200 nm mesas for active passive integration on photonic integrated circuits. In the case of the active

passive integration for the UTC-PD, the mesa height is approximately 2  $\mu\text{m}$ . This caused unforeseen issues with facet formation during growth. Figure 4 - 24b shows an SEM image of the mesa regions after regrowth. One problem encountered was alignment to the global marks post-regrowth. Figure 4 - 24a shows the alignment mark. In the second generation, a mask was made to blanket etch the regrowth surface over the alignment mark to re-expose the original mark. This was only partially successful as can be seen in Figure 4 - 24c where the application of the HCl:HPO etch causes additional faceting near the edges of the mesas. This was a bigger issue for the active regions of the WGPD as can be seen Figure 4 - 24d. In the second generation of the UTC-PD fabrication design, the initial active mesas were uniformly patterned to by 5  $\mu\text{m}$  wide to push this faceting farther from the final device region.

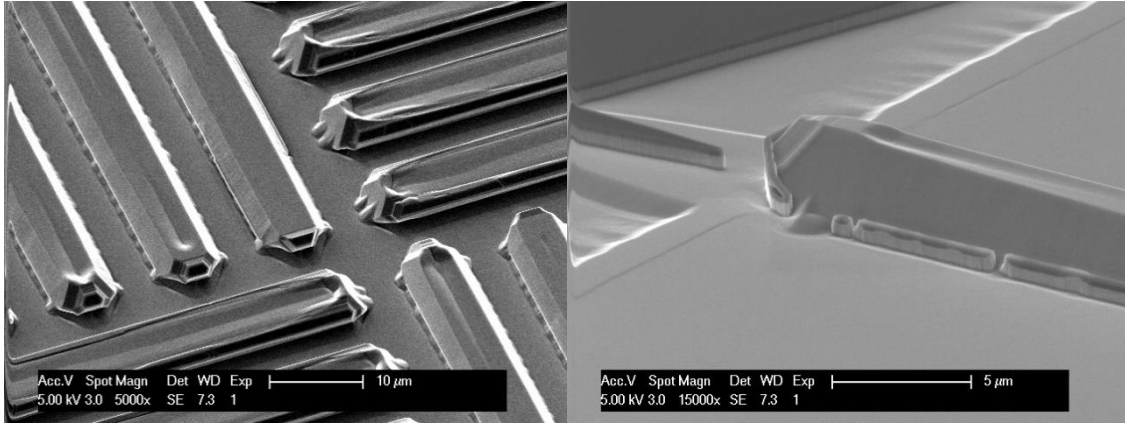
### ***Mode Converter Formation***

The next step in the fabrication process is the formation of the spot size or mode converter. This is completed using a first a dry etch or  $\text{Cl}_2:\text{H}_2:\text{Ar}$  or  $\text{CH}_4:\text{H}_2:\text{Ar}$ . A comparison between the two etch is shown in the SEM images of Figure 4 - 25 . The step is finished with a wet etch using  $\text{HCl}:\text{H}_3\text{PO}_4$ , to stop on the passive waveguide layer and the etch stop layer on the active mesa. An SEM image of the mode converter is shown in Figure 4 - 26.

### ***N and P Contact Formation***

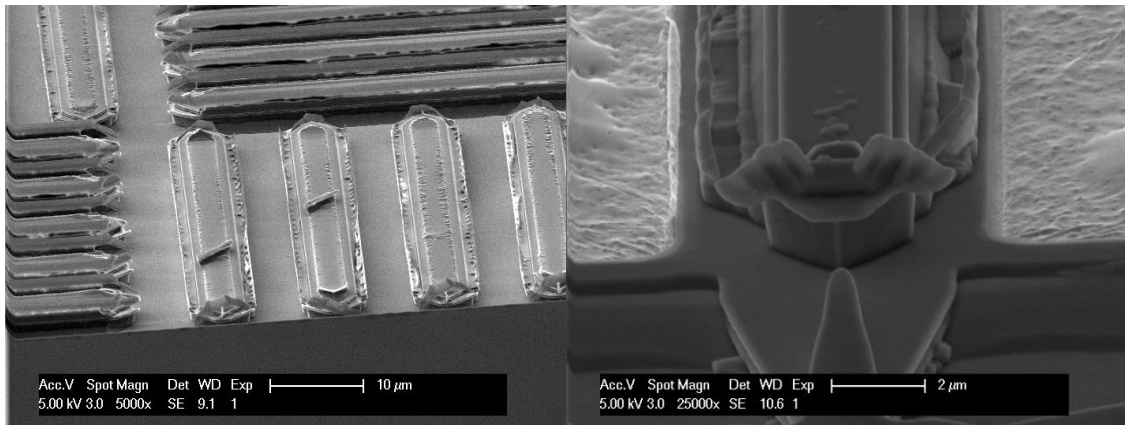
The next step is to form the contacts to the device. The N Contact is formed to a highly doped InP layer just below the InGaAsP waveguide layer. The passive waveguide layer that is capping the N-contact is first removed by a  $\text{H}_2\text{SO}_4:\text{H}_2\text{O}_2:\text{DI}$  etch. After etching the passive waveguide layer, the sample is cleaned in BHF just before loading to deposit a

Ni/AuGe/Ni/Au metal stack that forms the N-Contact. An anneal is done at 400°C to diffuse the AuGe layer partially into the semiconductor, while the Ni layers act as diffusion barriers for both the diffusion between AuGe and Au, and, diffusion too deeply into the InP layer. One commonly encountered problem in this step was residual etch products on the surface after



(a)

(b)



(c)

(d)

Figure 4 - 24 (a) Plan view SEM of local alignment marker after 1 μm InP regrowth showing the crystal facet formation due to the large mesas present. (b) Active mesa after dry etching the InP regrowth. (c) Local alignment marker after a dry etch followed by wet etch (HCl:H<sub>3</sub>PO<sub>4</sub>) showing the faceting of various regions. (d) Active mesa following the wet etch.

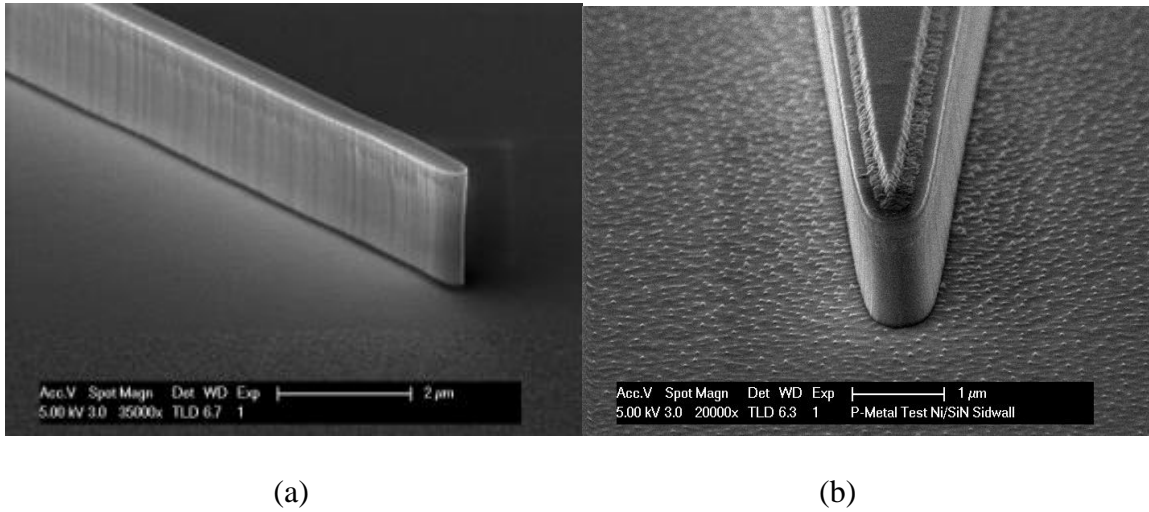


Figure 4 - 25 SEM of (a) unaxis (Cl:H:Ar) dry etch vs (b) RIE 2 (MHA) dry etch.

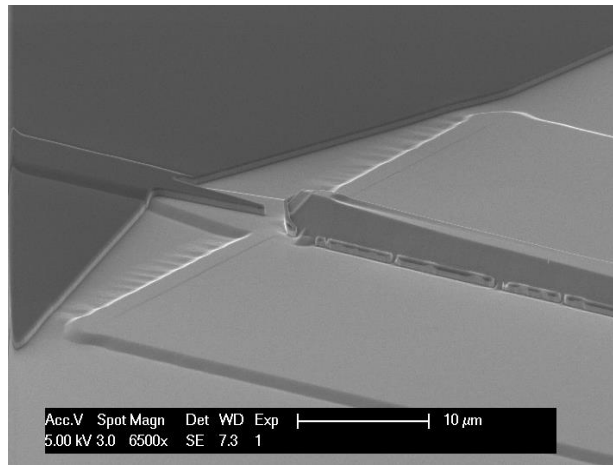


Figure 4 - 26 Plan view SEM showing the double tapered waveguide that forms the spot size converter. The optical power comes from the left. As the cladding is tapered down, the passive waveguide layer is simultaneously tapered from 1 μm to 5 μm.

removing the passive waveguide. O<sub>2</sub> plasma was found to be most reliable in removing this layer and making the alloying process more reliable. Figure 4 - 27 shows a comparison between N-contacts that alloy correctly and those that has significant residue at the interface.

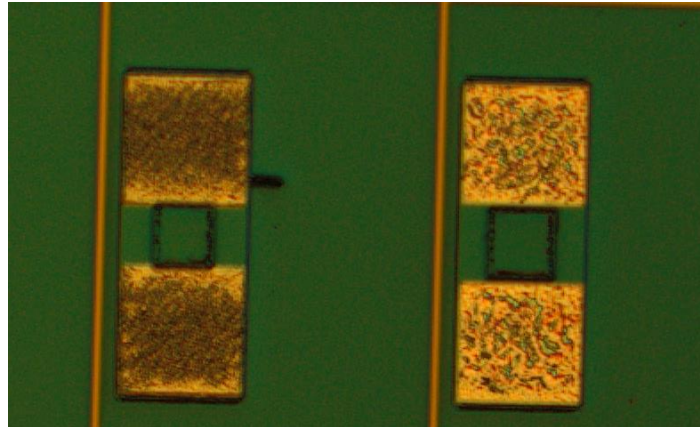


Figure 4 - 27 Optical image of two adjacent n-contact pads after annealing showing varying reaction and diffusion in to the InP layer. Without an O<sub>2</sub> plasma etch after wet etching the InGaAsP layer, residual etch byproducts cause the anneal to be unreproducible across the surface.

**Table 5 List of photoresist formulations used for device fabrication**

Photoresist Formulation	Thickness Range (μm)	Resolution Limit (nm)
SPR955CM-0.9	0.75 – 1.5	500
SPR220-3.0	2.5 - 4.5	1000
SPR220-7.0	5.5 – 10	1000

Formation of the P-contact present a more significant challenge, as the metal needs to be deposited on the narrow active mesa formed in the first step. In order to achieve the resolution required for this step, a process was developed to allow use of SPR955CM-0.9 photoresist. Table 5 shows a summary of the different photoresists used in this processing. Mesas with 2 μm height typically require photoresists thickness at least 2 μm in order to ensure the edges of the mesas are completely masked. Figure 4 - 19 shows a schematic of what photoresist coating looks like when using the appropriate thickness compared to using a photoresist that is too thin. This presents a tradeoff, as thinner photoresists generally achieve better resolution. For processing steps after etching of the mesa, SPR220-3.0 was used to achieve good coverage of the mesa, however, this resist is unable to achieve a resolution below 1 μm. In order to achieve

this resolution, a bilayer process was developed using PMGI SF-15 and SPR955CM-0.9 [39]. The PMGI serves as a planarization layer so that the SPR955CM-0.9 photoresist can achieve more uniform thickness. Figure 4 - 28a shows the effect of a high temperature bake (275°C) from the manufacturer demonstrating a more planar surface. This was confirmed using the DEKTAK profilometer to measure the maximum angle of the PMGI next to a mesa before and after baking. This initial measurement is limited by the geometrical shape of the profilometer head, however, as shown in Figure 4 - 28b, the angle was reduced from 30deg to approximately 2deg. The developed process is summarized in Figure 4 - 29 with the final panel showing the etched active region after the process, demonstrating that the 500 nm tapers were achieved despite the significant topographic variation over the surface of the wafer.

The P-contact is deposited after cycling through a UV-O<sub>3</sub> treatment for 10 minutes followed by 30 seconds of HCl:DI::1:10 etching. This process is repeated a second time, followed by a 30 second BHF dip and drying in N<sub>2</sub> before loading in the electron beam evaporator. For the first-generation devices and the second-generation devices without the mode converter, a Ti/Pt/Au metal stack was used. This metal stacks gives sufficiently low contact resistance for most devices; however, it was found that for the reduced size the specific contact resistance is too high. For the second generation with mode converters, a Pd/Ti/Pd/Au/Ti metal stack was used to form the P-Contact. This combination alloys with the highly doped InGaAs layer to reduce the contact resistance.

In the second generation of devices, where the initial mesa was oversized to reduce the regrowth faceting effects on the device, the top Ti layer of the P-contact was used as an etch mask to form the active region. Both Ni and Ti were tested as etch mask for the MHA etch in

RIE #2. It as found that Ti provided more resistance against the dry etch process, which can be seen in the microscope image of Figure 4 - 30. The device region after metal deposition and after etching using the metal hardmask is shown in Figure 4 - 31.

## BCB Encapsulation

Following formation of the contacts, the active device is encapsulation in BCB to minimize parasitic capacitance between the final pad metal and the semiconductor layers that lie below it. Photosensitive BCB was used to cover the active mesa and provide a large pad for probing the device. After exposing and developing the BCB, the sample was loaded into the Blue M oven and baked at 250°C for 2 hours with a slow ramp and cool down to make the total process about 6 hours. The thickness before and after baking was measured and found to reduce by about 20%.

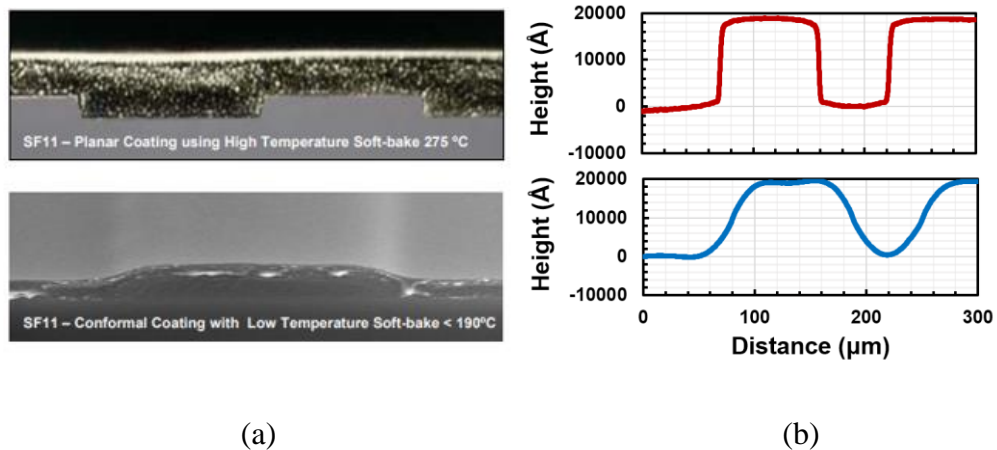


Figure 4 - 28 (a) Illustration of the coating morphology of PMGI SF11 different baking procedures as noted in the images. (Adapted from [40]) (b) Dektak profilometer measurements of the PMGI SF11 spin coated over 2 μm mesas after 115C bake (top) and 275C bake (bottom) showing the reduction in surface topography contrast.

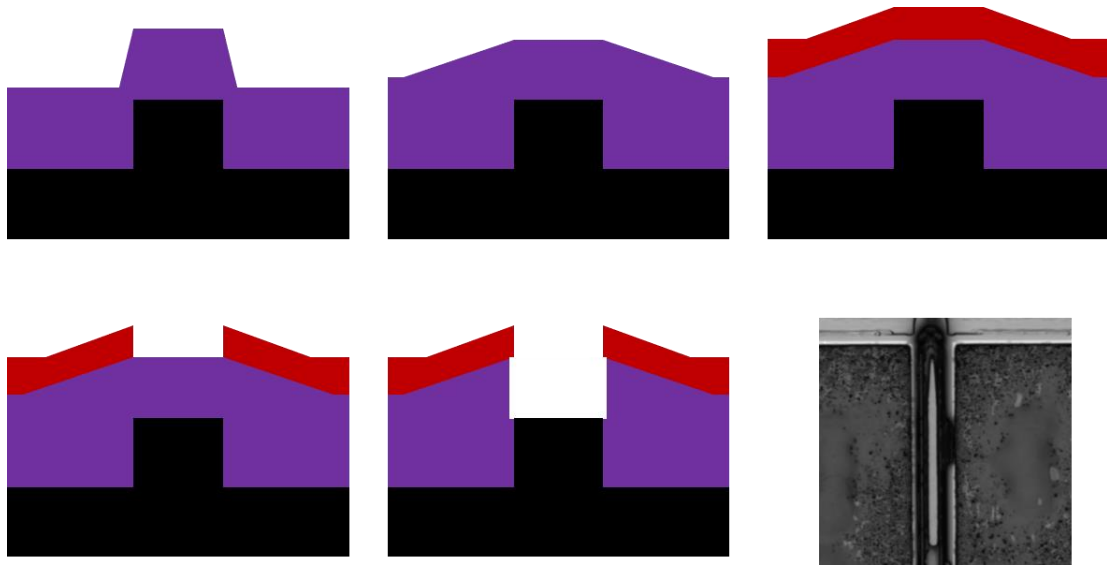
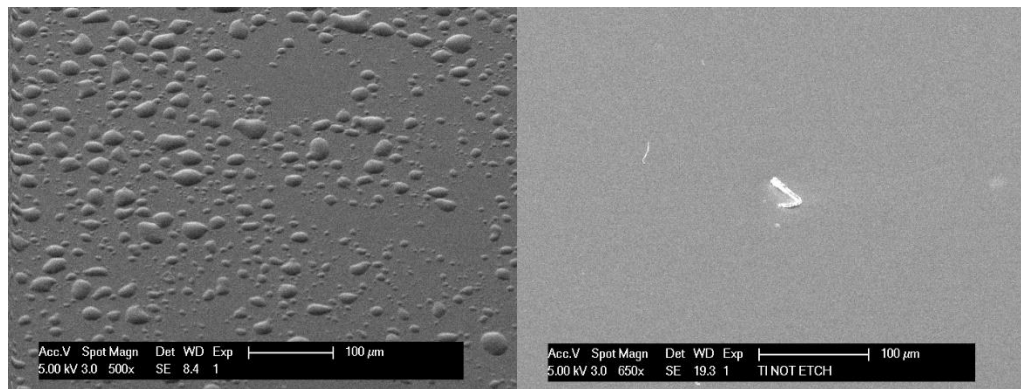


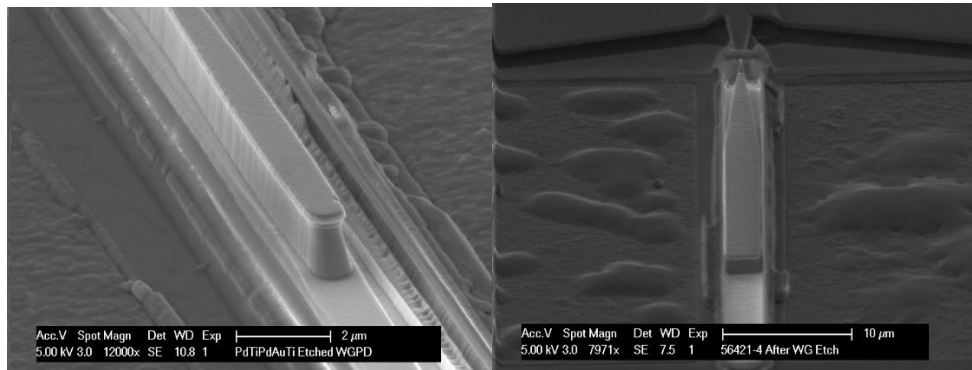
Figure 4 - 29 Illustration of the process developed to open narrow vias on high surface morphology samples. The process proceeds as follows. First PMGI SF15 is spin coated on the sample to a thickness around 2  $\mu\text{m}$  (top left) and then baked at 275C for 5 minutes to improve surface planarity (top middle). Next, SPR955CM-0.9 is spin coated to a thickness of  $\sim 900$  nm (top right) and the standard lithography process is followed to expose and develop the photoresist (bottom left). A deep-UV flood expose and selective development with 101A (TEAH) is used to develop the PMGI to the top of the mesa. The bottom right panel shows the final WGPD mesa after using this process to dry etch the mesa demonstrating the ability to make high resolution features on a non-planar surface.



(a)

(b)

Figure 4 - 30 Plan view SEM images showing Ni (a) and Ti (b) after dry etching in RIE 2 for 10 minutes under 450 V.



(a)

(b)

Figure 4 - 31 Plan view SEM image of 1  $\mu\text{m}$  wide mesa (a) and 2.5  $\mu\text{m}$  wide mesa (b) after using the PMGI process to deposit the p-contact and use the top Ti layer as an etch mask in RIE 2.

### Pad Metal Deposition

After encapsulating the active region in BCB, an opening in the BCB is created to allow the pad metal to connect to the initial P-contact metal. The bilayer process was used to planarize the surface and allow the use of SPR955CM-0.9 photoresist. ICP 2 was used to etch the BCB and SiN layers that encapsulated the BCB for adhesion reasons. For etching of SiN the standard recipe of  $\text{CHF}_3:\text{CF}_4:\text{O}_2$  was used, while for BCB the recipe used  $\text{O}_2:\text{CF}_4$  to etch. Due to the BCB being used to eliminate parasitic capacitance, it is critical to stop this etch just after exposing the P-metal. The BCB etch was completed by etching then loading the sample into the SEM to inspect the opening as the optical microscopes did not provide enough zoom to see the opening. Figure 4 - 32 shows the progression of the BCB etching with the final image showing the exposed P-metal. After recoating the BCB in SiN and creating an opening in the SiN to the P-metal, a pad metal stack of Ti/Au is deposited. The Au thickness is around 1  $\mu\text{m}$  to accommodate the mesa heights and ensure continuity of the pad metal.

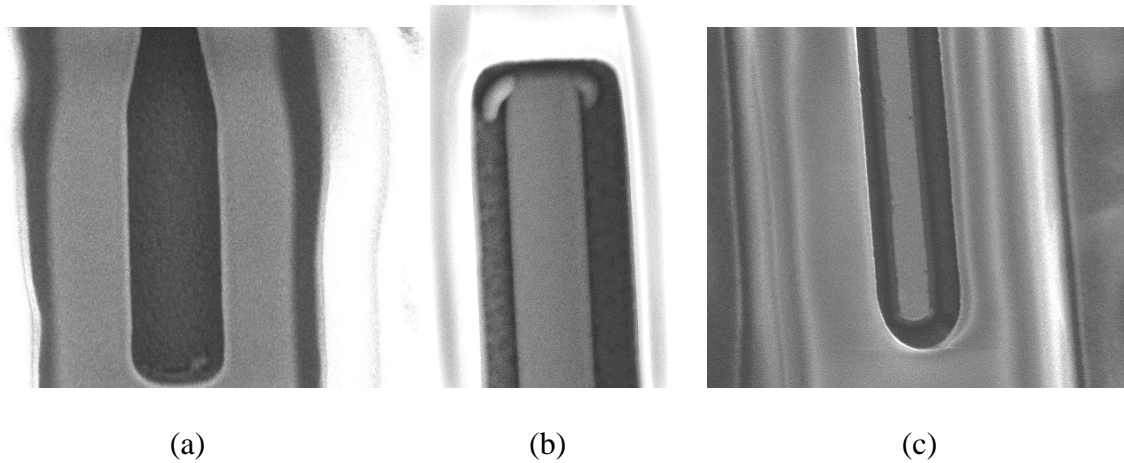


Figure 4 - 32 Plan view SEM images of the BCB etch after 2 min (a), 5 min (b), and 6 min (c) showing the progression of the mesa from being unexposed (a) to partly (b) and fully exposed (c).

## References

- [1] S. Arafin and L. A. Coldren, “Advanced InP Photonic Integrated Circuits for Communication and Sensing,” *IEEE J. Sel. Top. Quantum Electron.*, vol. 24, no. 1, 2018.
- [2] J. Klamkin *et al.*, “Indium Phosphide Photonic Integrated Circuits: Technology and Applications,” in *2018 IEEE BiCMOS and Compound Semiconductor Integrated Circuits and Technology Symposium, BCICTS 2018*, 2018.
- [3] C. G. H. Roeloffzen *et al.*, “Silicon nitride microwave photonic circuits,” *Opt. Express*, vol. 21, no. 19, pp. 22937–22961, 2013.
- [4] L. A. Coldren, S. W. Corzine, and M. L. Masanovic, *Diode Lasers and Photonic Integrated Circuits*, vol. 36, no. 2. Wiley, 1997.
- [5] U. K. Mishra and J. Singh, “Semiconductor device physics and design,” *Semicond.*

- Device Phys. Des.*, pp. 1–559, 2008.
- [6] S. Adachi and K. Oe, “Linear electro-optic effects in zincblende-type semiconductors : Key properties of InGaAsP relevant to device design,” *J. Appl. Phys.*, vol. 56, no. 1, 1984.
- [7] H. Ito, S. Kodama, Y. Muramoto, T. Furuta, T. Nagatsuma, and T. Ishibashi, “High-Speed and High-Output InP–InGaAs Unitraveling-Carrier Photodiodes,” *IEEE J. Sel. Top. Quantum Electron.*, vol. 10, no. 4, pp. 709–727, 2004.
- [8] J. E. Bowers and C. A. Burrus, “Ultrawide-Band Long-Wavelength p-i-n Photodetectors,” *J. Light. Technol.*, vol. LT-5, no. 10, 1987.
- [9] T. Ishibashi, N. Shimizu, S. Kodama, H. Ito, T. Nagatsuma, and T. Furuta, “Unitraveling-Carrier Photodiodes,” in *OSA TOPS on Ultrafast Electronics and Optoelectronics*, 1997, vol. 13, pp. 83–87.
- [10] K. Kato, “Ultrawide-band/high-frequency photodetectors,” *IEEE Trans. Microw. Theory Tech.*, vol. 47, no. 7, pp. 1265–1281, 1999.
- [11] K. J. Williams, R. D. Esman, and M. Dagenais, “Nonlinearities in p-i-n microwave photodetectors,” *J. Light. Technol.*, vol. 14, no. 1, pp. 84–96, 1996.
- [12] K. J. Williams, R. D. Esman, and S. Member, “Design Considerations for High-Current Photodetectors,” vol. 17, no. 8, pp. 1443–1454, 1999.
- [13] G. Lucovsky, R. F. Schwarz, and R. B. Emmons, “Transit-Time Considerations in p—i—n Diodes,” *J. Appl. Phys.*, vol. 35, no. 3, p. 622, 1964.
- [14] V. J. Urick, J. D. McKinney, and K. J. Williams, *Fundamentals of Microwave Photonics*. Wiley, 2015.

- [15] U. Gliese, K. Colladay, A. S. Hastings, D. A. Tulchinsky, V. J. Urick, and K. J. Williams, "RF power conversion efficiency of photodiodes driven by MachZehnder modulators," *IEEE Trans. Microw. Theory Tech.*, vol. 58, no. 11 PART 2, pp. 3359–3371, 2010.
- [16] J. W. Shi *et al.*, "Extremely high saturation current-bandwidth product performance of a near-ballistic uni-traveling-carrier photodiode with a flip-chip bonding structure," *IEEE J. Quantum Electron.*, vol. 46, no. 1, pp. 80–86, 2010.
- [17] J. W. Shi, F. M. Kuo, and J. E. Bowers, "Design and analysis of ultra-high-speed near-ballistic uni-traveling-carrier photodiodes under a 50- $\Omega$  load for high-power performance," *IEEE Photonics Technol. Lett.*, vol. 24, no. 7, pp. 533–535, 2012.
- [18] J. M. Wun, R. L. Chao, Y. W. Wang, Y. H. Chen, and J. W. Shi, "Type-II GaAs<sub>0.5</sub>Sb<sub>0.5</sub>/InP Uni-Traveling Carrier Photodiodes with Sub-Terahertz Bandwidth and High-Power Performance under Zero-Bias Operation," *J. Light. Technol.*, vol. 35, no. 4, pp. 711–716, 2017.
- [19] Q. Li *et al.*, "High-Power Flip-Chip Bonded Photodiode with 110 GHz bandwidth," vol. 1, pp. 450–451, 2015.
- [20] Q. Li *et al.*, "High-Power Evanescently Coupled Waveguide MUTC Photodiode with >105-GHz Bandwidth," *J. Light. Technol.*, vol. 35, no. 21, pp. 4752–4757, 2017.
- [21] V. Rymanov, P. Lu, S. Dülme, and A. Stöhr, "Lens-assisted quasi-optical THz transmitter employing antenna-integrated triple transit region photodiodes," *MWP 2017 - 2017 Int. Top. Meet. Microw. Photonics*, vol. 2017-December, pp. 1–4, 2017.
- [22] V. Rymanov, A. Stöhr, S. Dülme, and T. Tekin, "Triple transit region photodiodes

- (TTR-PDs) providing high millimeter wave output power.,” *Opt. Express*, vol. 22, no. 10, pp. 7550–8, 2014.
- [23] E. Lacombe, F. Giancesello, C. Durand, G. Ducournau, C. Luxey, and D. Gloria, “Sub-THz source integrated in industrial silicon Photonic technology targeting high data rate wireless applications,” *SiRF 2017 - 2017 IEEE 17th Top. Meet. Silicon Monolith. Integr. Circuits RF Syst.*, pp. 26–29, 2017.
- [24] G. Zhou and P. Runge, “Nonlinearities of High-Speed p-i-n Photodiodes and MUTC Photodiodes,” *IEEE Trans. Microw. Theory Tech.*, vol. 65, no. 6, pp. 2063–2072, 2017.
- [25] H. Ito and T. Ishibashi, “Photonic terahertz-wave generation using slot-antenna-integrated uni-traveling-carrier photodiodes,” *IEEE J. Sel. Top. Quantum Electron.*, vol. 23, no. 4, 2017.
- [26] T. Ishibashi, Y. Muramoto, T. Yoshimatsu, and H. Ito, “Continuous THz wave generation by photodiodes up to 2.5 THz,” *Int. Conf. Infrared, Millimeter, Terahertz Waves, IRMMW-THz*, pp. 1–2, 2013.
- [27] A. J. Seeds, H. Shams, M. J. Fice, and C. C. Renaud, “TeraHertz photonics for wireless communications,” *J. Light. Technol.*, vol. 33, no. 3, pp. 579–587, 2015.
- [28] E. Rouvalis *et al.*, “170 GHz Photodiodes for InP-based photonic integrated circuits,” *2012 IEEE Photonics Conf. IPC 2012*, vol. 20, no. 18, pp. 88–89, 2012.
- [29] E. Rouvalis, C. C. Renaud, D. G. Moodie, M. J. Robertson, and A. J. Seeds, “Traveling-wave Uni-Traveling Carrier photodiodes for continuous wave THz generation.,” *Opt. Express*, vol. 18, no. 11, pp. 11105–11110, 2010.
- [30] P. Latzel *et al.*, “High efficiency UTC photodiodes as photonic emitters for 300 GHz

- high spectral efficiency wireless communications,” *2017 11th Eur. Conf. Antennas Propagation, EUCAP 2017*, pp. 1639–1641, 2017.
- [31] P. Latzel *et al.*, “Generation of mW Level in the 300-GHz Band Using Resonant-Cavity-Enhanced Unitraveling Carrier Photodiodes,” *IEEE Trans. Terahertz Sci. Technol.*, vol. 7, no. 6, pp. 800–807, 2017.
- [32] M. Anagnosti *et al.*, “Optimized High Speed UTC Photodiode for 100 Gbit/s Applications,” *IEEE J. Sel. Top. Quantum Electron.*, vol. 20, no. 6, pp. 29–35, 2014.
- [33] J. Klamkin, “Coherent Integrated Receiver for Highly Linear Microwave Photonic Links,” University of California Santa Barbara, 2008.
- [34] A. M. T. Pedretti, “Monolithic Separate Absorption and Modulation Mach-Zehnder Wavelength Converters,” University of California Santa Barbara, 2007.
- [35] A. Sivananthan, “Integrated Linewidth Reduction of Rapidly Tunable Semiconductor Lasers,” 2013.
- [36] J. S. Parker, “Santa Barbara Integrated Photonic Comb Generation : Applications in Coherent Communication and Sensing,” University of California Santa Barbara, 2012.
- [37] C. G. H. Roeloffzen *et al.*, “Low-loss  $\text{Si}_3\text{N}_4$  triplex optical waveguides: Technology and applications overview,” *IEEE J. Sel. Top. Quantum Electron.*, vol. 24, no. 4, 2018.
- [38] J. A. Summers, “Monolithic Multi-Stage Wavelength Converters for Wavelength-Agile Photonic Integration,” University of California Santa Barbara, 2007.
- [39] MicroChem, “NANO PMGI Resists <sup>TM</sup> Datasheet.” 2002.
- [40] Microchem Corp, “LOR and PMGI Resists,” 2015.

## Chapter 5

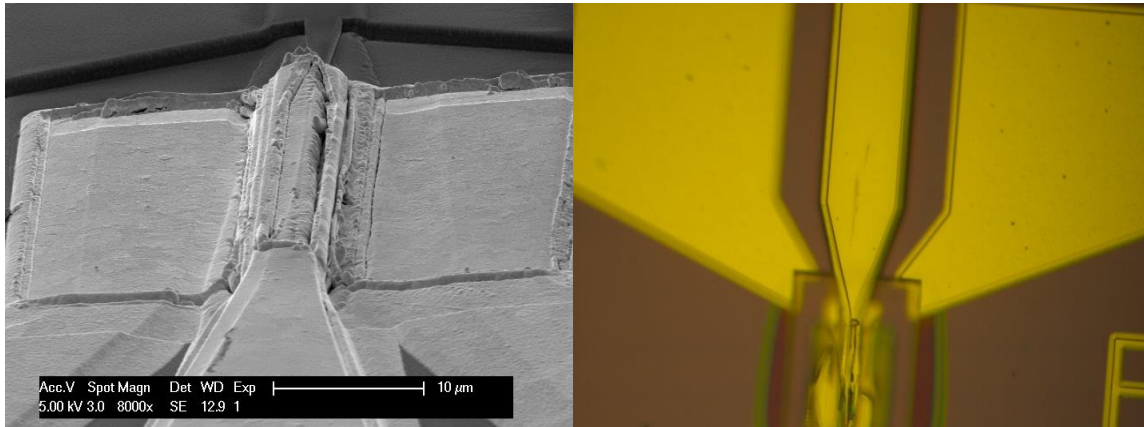
# Experimental Results on Uni-traveling

## Carrier Photodiode

Successful fabrication requires anticipating where problems may arise in the fabrication and understanding the limitations of the systems that will be used. The results from the UTC-PD can be broken down into three generations: the initial “attempt” to create the full structure, the second run that eliminated the mode converter and regrowth step to simplify the fabrication process, and the final run that incorporated the mode converter.

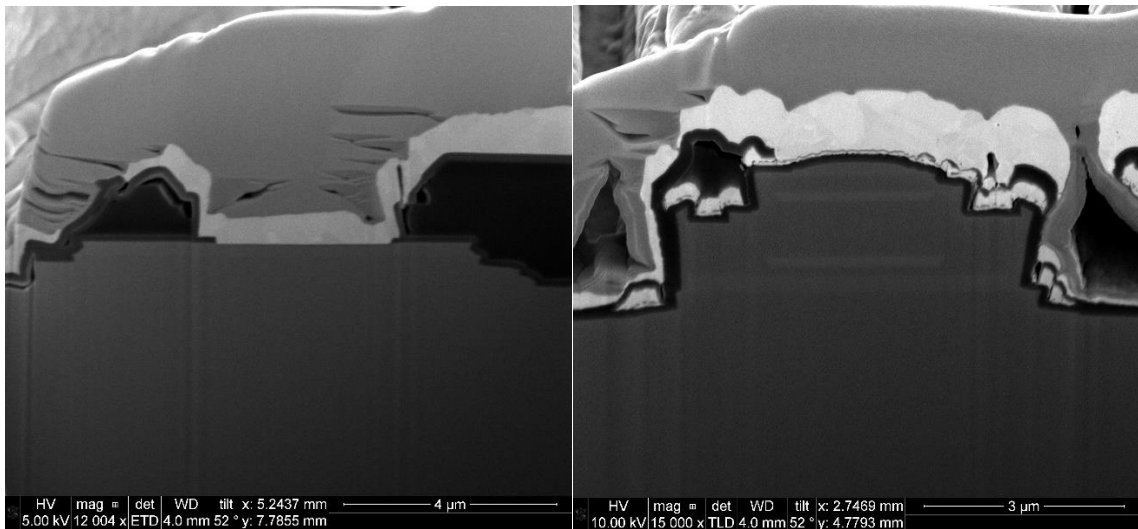
### First Generation

The first generation of devices was an exercise in the proper layout of the mask and understanding the capabilities of fabrication equipment. This provided the groundwork to generate a layout that could be successful. The most critical issues that led to the failure of the devices included the inability to resolve the narrow waveguide photodiodes, improper bilayer photoresist processes, and over/under etching of BCB. Figure 5 - 1 shows a composite of SEM and microscope images showing the failure process just mentioned. Several working devices were found despite the issues, with the results shown in Figure 5 - 2. The working devices suffered from poor isolation and high parasitic capacitance which led to large dark current and low bandwidth on the order of 100  $\mu$ A and 7 GHz.



(a)

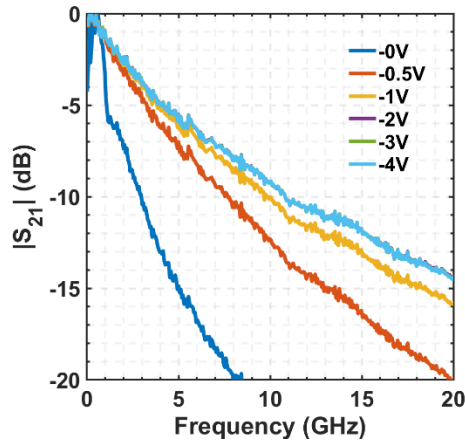
(b)



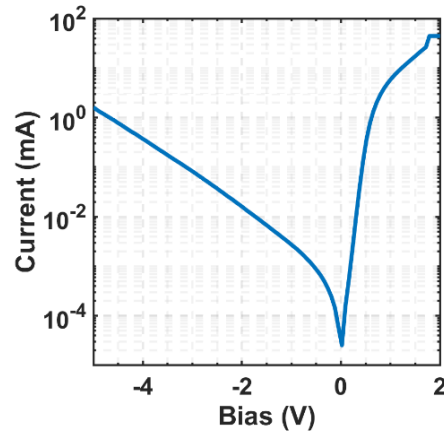
(c)

(d)

Figure 5 - 1 (a) SEM of metal pad metal deposited on device. Due to lithography resolution issues from the surface topography, the gap between the p and n metal was not defined leading to a short circuit on many devices. (b) Optical image of devices where lift off layer was not fully developed away leading to open circuit devices. (c) FIB-SEM image of device cross section showing a section where the PN-junction was completely removed during processing leading to short circuit behavior. (d) FIB-SEM of device cross section showing device layers with dielectric layer isolating the p-contact from the metal leading to an open circuit behaviour.



(a)



(b)

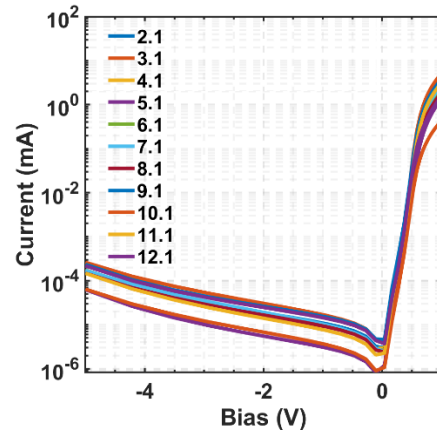
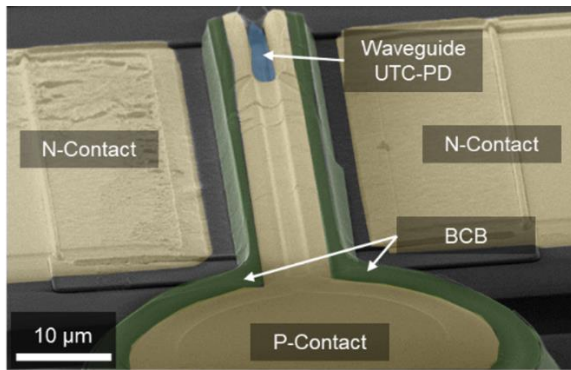
Figure 5 - 2 (a) Frequency response measurements for working device from the first fabrication run showing 3-dB bandwidths around 3 GHz. (b) IV measurement of device showing diode behavior with poor isolation of around  $2000 \Omega$  under reverse bias.

The failure analysis performed on the first generation of devices led to decision to first create a simplified process that eliminated process difficulties by not including the mode converter. Additionally, a planarization process was developed in order to solve the issue of high resolution on the non-planar surface.

**Table 6 Photodiode variations**

Bar	Width ( $\mu\text{m}$ )	Taper Variations	Length ( $\mu\text{m}$ )
1	1	5, 10, 20 $\mu\text{m}$ length	20, 40, 60
2	Various widths	Various taper lengths and number of tapers	30, 40, 50, 60
3	1.5	5, 10, 20 $\mu\text{m}$ length	15, 30, 45
4	Various widths	No Taper	10, 20, 30
5	2	5, 10, 20 $\mu\text{m}$ length	15, 30, 45
6	3	5, 10, 20 $\mu\text{m}$ length	15, 30, 45

## Second Generation



(a)

(b)

Figure 5 - 3 (a) SEM image of 2<sup>nd</sup> generation device without spot size converter after completed fabrication. (b) IV measurement for multiple devices showing significant improvement in reverse bias leakage current. Resistance under reverse bias is around 20 k $\Omega$ .

Table 6 summarizes the waveguide geometry variations used in the second and third fabrication runs. The second generation of devices were completed without the mode converter and no regrowth step. While this simplified the fabrication, this led to variable responsivity depending on the location of the cleaved facet from the active region. Figure 5-4 shows a simple schematic of the cleave location for the second-generation devices. For initial bars that were cleaved at the red arrow, the responsivity was too low to allow sufficient signal for RF measurements using the Lightwave Component Analyzer (LCA). However, by moving the cleave location closer to the start of the active mesa, shown as the black arrow, orders of magnitude increase in the responsivity were observed. Eliminating the mode converter and regrowth demonstrated the design potential to reach greater than 67 GHz bandwidth as shown in Figure 5 -5a, which was limited by the measurement setup. Devices impedances were also

measured using the LCA which allows for fitting the circuit model shown in Figure 4 – 4 to extract the device capacitance and series resistance. Figure 5 – 5b shows the device impedance on a smith chart along with a fit to the data giving a series resistance and capacitance of 35  $\Omega$  and 20 fF respectively. Figure 5 – 5c and d show fitting results for various devices of the different waveguide geometries listed in Table 6 showing the decrease and increase respectively in the capacitance and resistance as a function of the active mesa area.

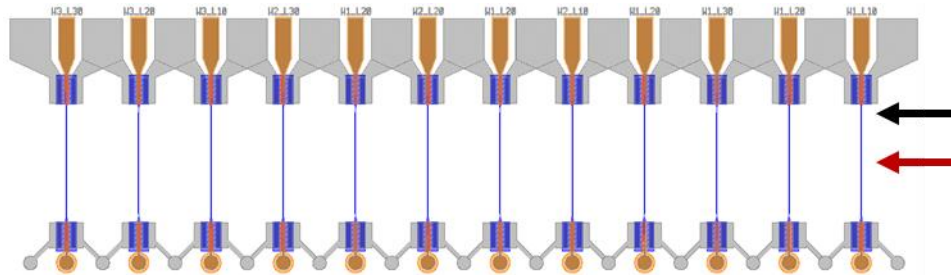


Figure 5 - 4 Cleaving diagram for cleaving between bars. The bars were cleaved at the black arrow close to the start of the active mesa due to the high waveguide loss without the regrowth step. Bars with the cleave at the red arrow did not have sufficient coupling to obtain signal in RF measurements.

Figure 5 -6 shows a comparison between the measured 3-dB bandwidth and the calculated 3-dB bandwidth from the fitted resistance and capacitance data shown in Fig 5- 5c and d using

the expression  $f_{3dB} = \frac{1}{2\pi(R_s+R_L)C_j}$ . As shown, the calculation from the overestimates the

bandwidth in some cases by a significant amount. As outlined in Ref. [1], series resistance can more reliably be obtained by using the forward bias device impedance. For devices with very low junction capacitance it was found that this method could give a series resistance value several times high as shown in Table 2. The series resistance is most likely what is the current

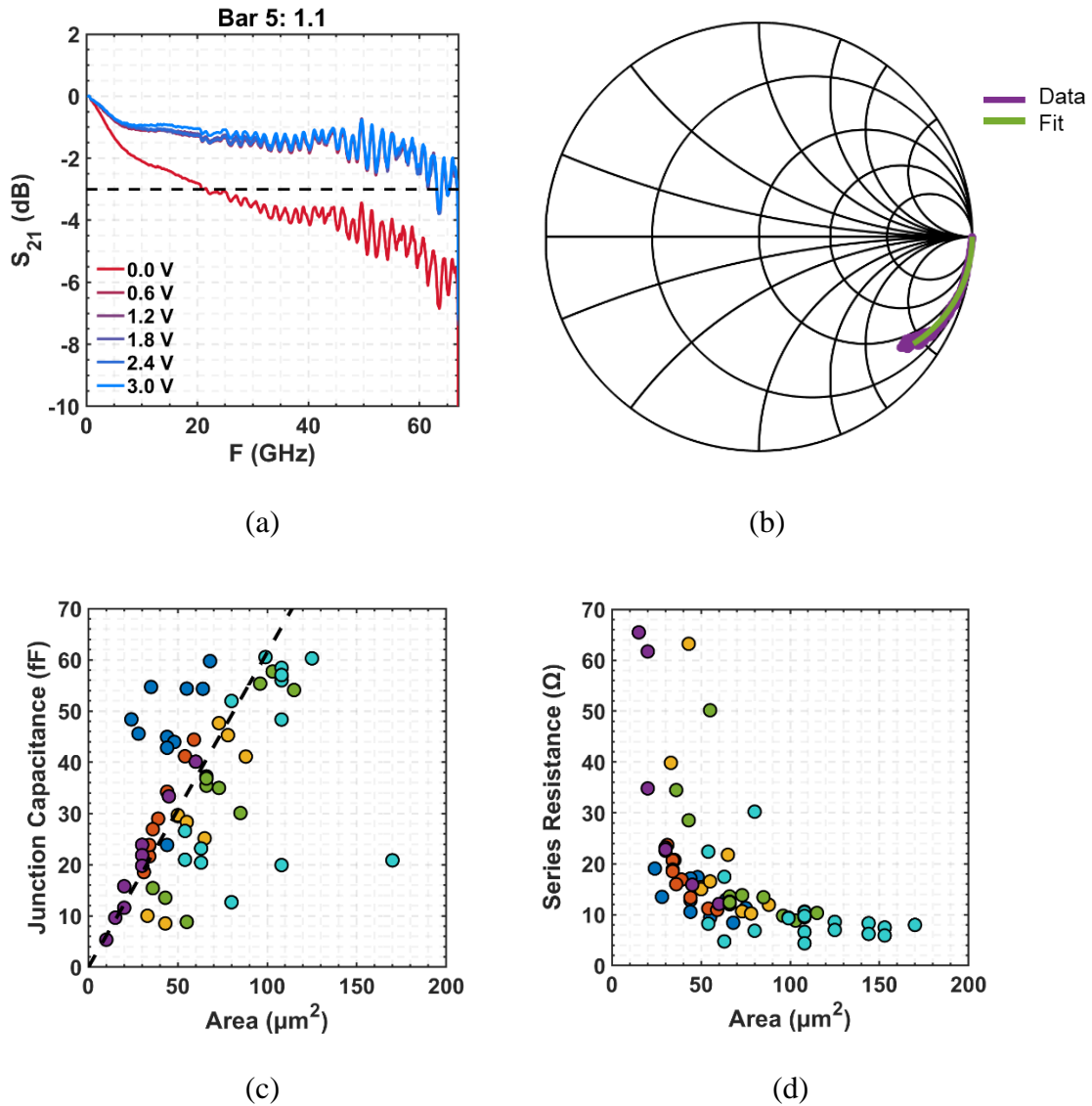


Figure 5 - 5 (a) Frequency response of 2  $\mu\text{m}$  wide ridge device with total area of 23  $\mu\text{m}^2$  under varying reverse bias voltages. The 3-dB bandwidth is over 67 GHz. (b)  $S_{11}$  of same devicice under reverse bias of 3 V. The fitted series resistance and junction capacitance are 35  $\Omega$  and 20 fF respectively. (c) Calculated junction capacitance from  $S_{11}$  fitting for various devices on a single die. (d) Calculated series resistance from  $S_{11}$  fitting for various devices on a single die. The  $S_{11}$  data was fit to the circuit model shown in Figure 4 - 4.

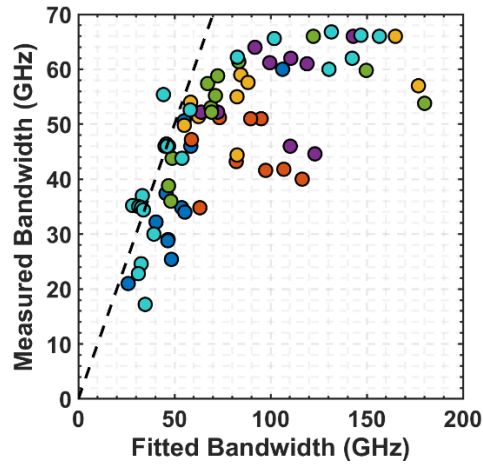


Figure 5 - 6 Comparison of the fitted bandwidth from the series resistance and junction capacitance calculated from S11 measurements to the measured bandwidth.

bandwidth limitation of these devices. Based on the results shown in Table 2, the bandwidth could be increased by roughly 60% by reducing the series resistance down to values around 10  $\Omega$ . This can be achieved by using a more highly doped InGaAs contact layer using carbon as the dopant [2].

**Table 7 Comparison of fitted series resistance under forward and reverse bias**

Bias (V)	Series Resistance ( $\Omega$ )
+1	45
-2	5.2

RF output power is another quantity measured for these devices. At frequencies below 60 GHz, this can be achieved using modulator. The result at 8 GHz is shown in Figure 5 -7 demonstrating up to 6 dBm output power at 20 mA.

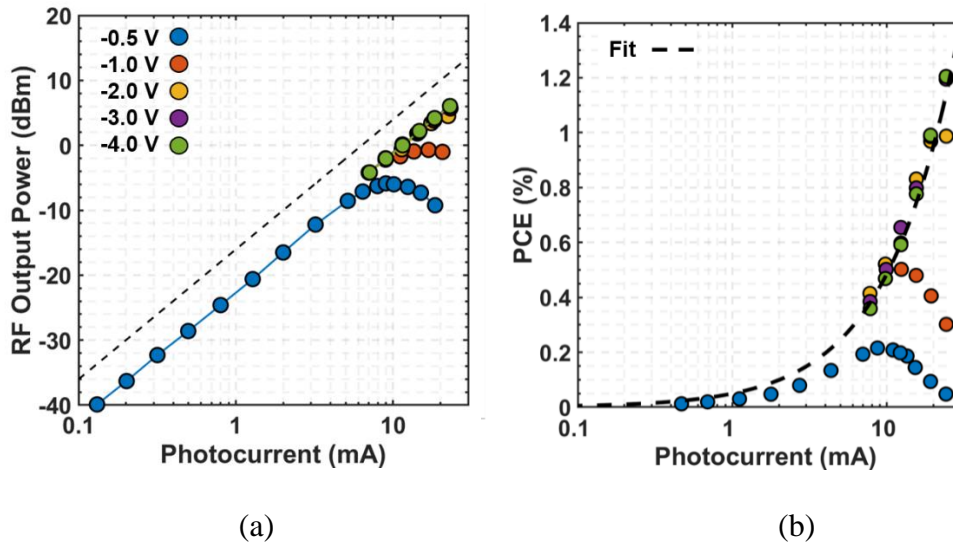


Figure 5 - 7 (a) RF output power as a function of photocurrent for increases reverse bias. (b) Calculated power conversion efficiency from the data in (a) showing good agreement with the model discussed earlier.

One device was selected to characterize more extensively to provide a better understanding of the dependence of the frequency response following a similar method as in Ref. [3]. Both S21 and S11 were taken up to 67 GHz for bias voltage between 0 and -2 V, and photocurrents from 200  $\mu$ A up to 6 mA. Figure 5 – 7a shows S21 for both high and low photocurrent at -2 V bias demonstrating both the increase in the 3-dB bandwidth and improved response at lower photocurrent. This is due to the space-charge reducing the electric field of the depletion region to increase the velocity of the carriers. Additionally, the increased response starting at low frequencies may be attributed to trap states that become saturated at photocurrents. The 3-dB bandwidth as a function of reverse bias and photocurrent is shown in Figure 5 - 7b and c, with c showing selective curves and b showing all curves offset for clarity. Increased bias required to obtain the same 3-dB bandwidth as a function of photocurrent is evident from this figure. In the context of power conversion efficiency discussed in Ch. 3 this illustrates the space-charge effect contribution to the required bias

voltage. The additional bias required can be quantified into an effective resistance by plotting the RF power compression of the S21 measurements as a function of photocurrent as shown in Figure 5 – 8d and e. The 1-dB compression photocurrent can then be plotted for each bias voltage to obtain a total series resistance that contributes to the power conversion efficiency formula introduced in Ch. 2. This is shown in Figure 5 – 8f. Using the value of the series resistance obtained from this measurement, the limiting efficiency of this device is 4%.

### **Third generation**

The third generation of devices incorporated the mode converter to optimize coupling to the Triplex SiN platform. However, the mode converter also improved the reliability of coupling from fiber due to the proper formation of a passive input waveguide. As shown in Figure 5 – 9, the responsivity of the PDs did not improve relative to the case without spot size converters, however, the distribution of the responsivity improved compared to devices without the spot size converter. Furthermore, for the chips measured from the third generation of devices, the cleave between bars was roughly half way between adjacent bars at the red arrow of Figure 5 - 4, while for the second generation, the cleave was typically done as close to the active device as possible. Frequency response measurements also demonstrated that devices also maintained high bandwidth as shown in Figure 5 – 10.

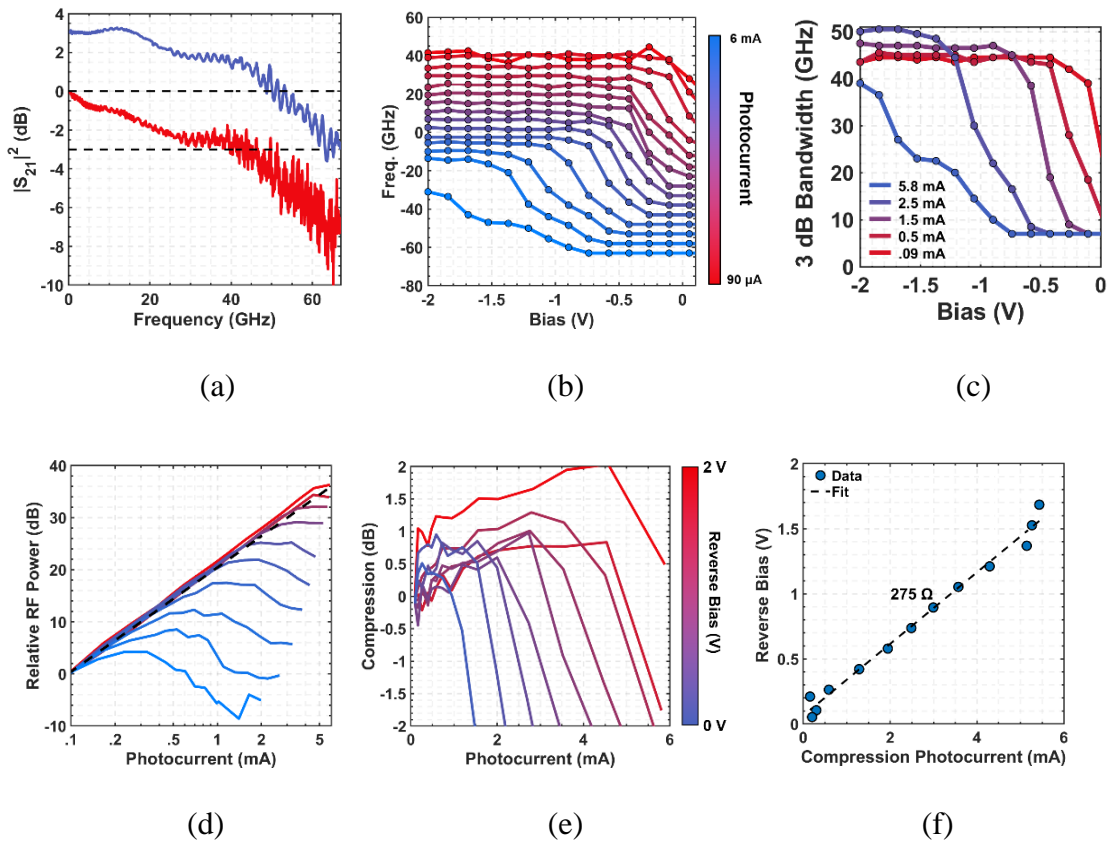


Figure 5 - 8 (a) Frequency response at -2 V bias for device with 3  $\mu\text{m}$  ridge width and 16  $\mu\text{m}^2$  total area under both high,  $\sim 5\text{mA}$ , (blue) and low,  $\sim 100\ \mu\text{A}$  (red) photocurrents. (b) 3-dB bandwidth frequency for various input photocurrents as a function of reverse bias. The curves are offset by 5 GHz for clarity. (c) Select 3-dB bandwidths curves from (b) without 5 GHz offset. (d) Relative RF power received in the LCA for the device at 60 GHz as a function of photocurrent for various reverse bias values. (e) Compression of RF power in (d) as a function of photocurrent for the various reverse bias values. (f) 1-dB compression photocurrent for each of the reverse bias measurements. Fitting this line gives an effective resistance that can be used to correlate the bias required to avoid RF output power compression for high input optical powers.

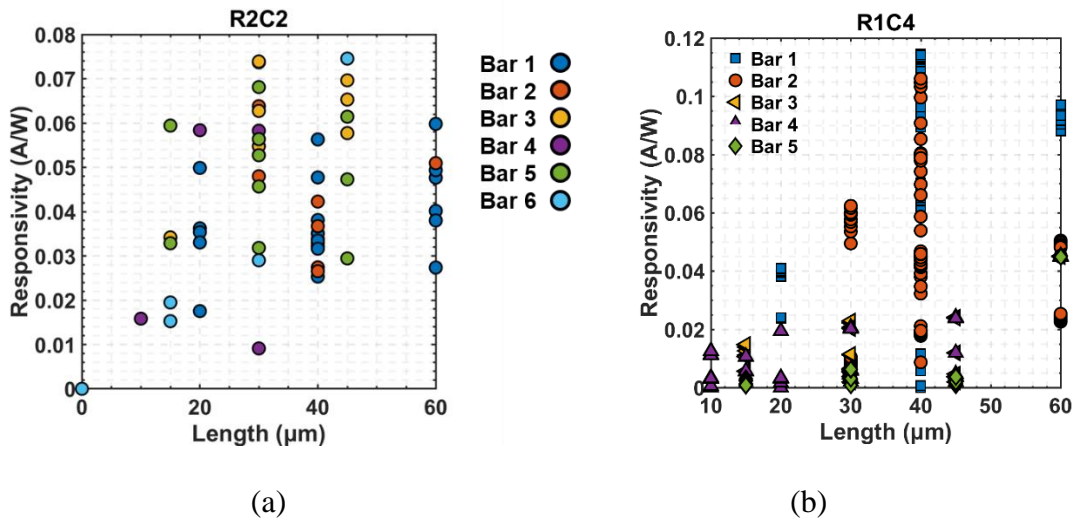


Figure 5 - 9 Responsivity for various devices from third generation with spot size converter (a) and from the second generation without a spot size converter (b).

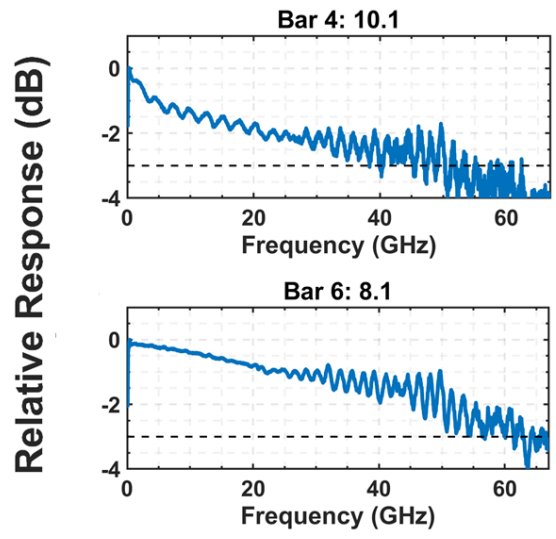


Figure 5 - 10 Frequency response of third generation devices showing grating than 50 and 60 GHz bandwidth.

## Conclusion

In this chapter, the results of the design and fabrication development from the previous chapter were discussed. The first generation of devices served to illustrate many of the challenges that needed to be solved to successfully fabricate the designed devices. The second generation of devices served to demonstrate the design potential to achieve greater than 67 GHz bandwidth by sacrificing responsivity to gain a simpler fabrication process. The third generation of devices combined the waveguide UTC-PDs with integrated spot sized converters were demonstrated with up to 60 GHz bandwidth, and  $\sim 0.1$  A/W responsivity.

## References

- [1] Z. Zhang *et al.*, “Compact Modeling for Silicon Photonic Heterogeneously Integrated Circuits,” *J. Light. Technol.*, vol. 35, no. 14, pp. 2973–2980, 2017.
- [2] A. Baraskar, “Development of Ultra-Low Resistance Ohmic Contacts for InGaAs / InP HBTs,” University of California Santa Barbara, 2011.
- [3] M. A. Hollis, “Space-charge impedance in photodiodes,” *IEEE Photonics Technol. Lett.*, vol. 23, no. 18, pp. 1307–1309, 2011.

## Chapter 6

# Photonic Integrated Circuit Components and Fabrication

### Photonic Integrated Circuit for FMCW LIDAR

The components of the PIC consist of two type of PN-junctions: one containing quantum wells offset from the waveguide layer, which we refer to as the active sections, and a second without the quantum wells, which we refer to as the passive sections [1]. The mirrors and phase tuning sections of the PIC consists of passive PN-junctions. As described in Ch 4, carrier injection is used to change index of refraction of the material which tunes the phase of the light. The active sections of the PIC, the laser gain section, semiconductor optical amplifier, and photodiodes, consist of PN junction with embedded QWs that are tailored to provide gain (positive or negative) for the 1530 nm to 1580 nm operating wavelength. In this case, forward biasing or injecting carriers into the PN junction, net positive gain can be achieved, while reverse biasing enhances the negative gain by sweeping the carriers out of the depletion region before the can recombine.

#### ***SGDBR Laser***

A standard Distributed Bragg Reflector (DBR) laser is a three or four section laser that uses a Bragg grating for at least one of the mirrors that form the laser cavity. A sampled grating

DBR, removes a portion of the grating at some period and duty cycle. The periods of the sampling are set at different values which gives rise to the Vernier effect. Figure 6 - 6 shows the reflection spectrum for two sampled gratings. The individual reflection spectra can be shift by thermal or electrical methods to obtain wide tunability due to the Vernier effect [2].

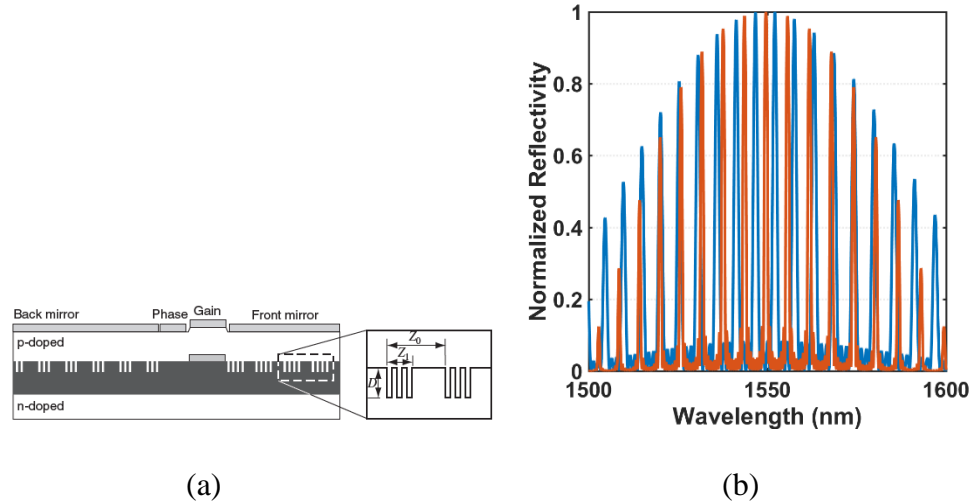


Figure 6 - 6 (a) Device diagram for SGDBR laser. The components are the front and back mirror, phase section, and gain section. (b) The reflection spectrums of the front (red) and back mirror (blue) showing the Vernier effect that arises from the sampled gratings.

## PIC Transceiver Fabrication

### *Active/Passive Definition*

The fabrication of the PIC transceiver is based off an offset quantum well technology developed previous at UCSB. The base epitaxial material is grown through the waveguide layer, multiple quantum wells, and capped with InP. The InP and QW layers are selectively removed by wet chemical etches using HCl:H<sub>3</sub>PO<sub>4</sub> and H<sub>2</sub>SO<sub>4</sub>:H<sub>2</sub>O<sub>2</sub>:DI respectively [3], [4].

Figure 6 - 7a shows the patterns of the active regions after etching. The interface along with the waveguide ridge passes is angled to reduce reflection due to abrupt index changes.

### ***Grating***

The gratings are patterned using electron beam lithography to achieve the 20 nm resolution required. After patterning the resist, the SiN hard mask is etched using ICP 2. After stripping the resist, AFM is used to ensure proper spacing, determine the exact SiN thickness, and check for surface roughness. Figure 6 - 7c shows the grating AFM after ICP 2 etching. The SiN the acts as a mask in RIE-2 to etch the gratings into the semiconductor [4]–[6]. The etch depth target is 80 nm into the waveguide layer, with an additional 20 nm InP cap layer. After etching, the gratings are again characterized by AFM to check for surface roughness. Figure 6 - 7b shows the optical plan view image after the RIE-2 etch.

### ***Regrowth***

The process for regrowth on the PIC transceiver is somewhat complicated by the RIE etch which generates some surface damage in the gratings. In order to clean the surface, a pure H<sub>2</sub>SO<sub>4</sub> etch is performed followed by DI rinse and drying in N<sub>2</sub>. The SiN hard mask is removed with BHF and the sample is loaded into the UV-O<sub>2</sub> reactor for 1 hour. Immediately before regrowth, a final 30 second BHF etch is performed followed by rinsing in DI and drying in N<sub>2</sub>. The regrowth consists of an p-InP cladding layer, highly doped p-InGaAs, and an InP cap layer.

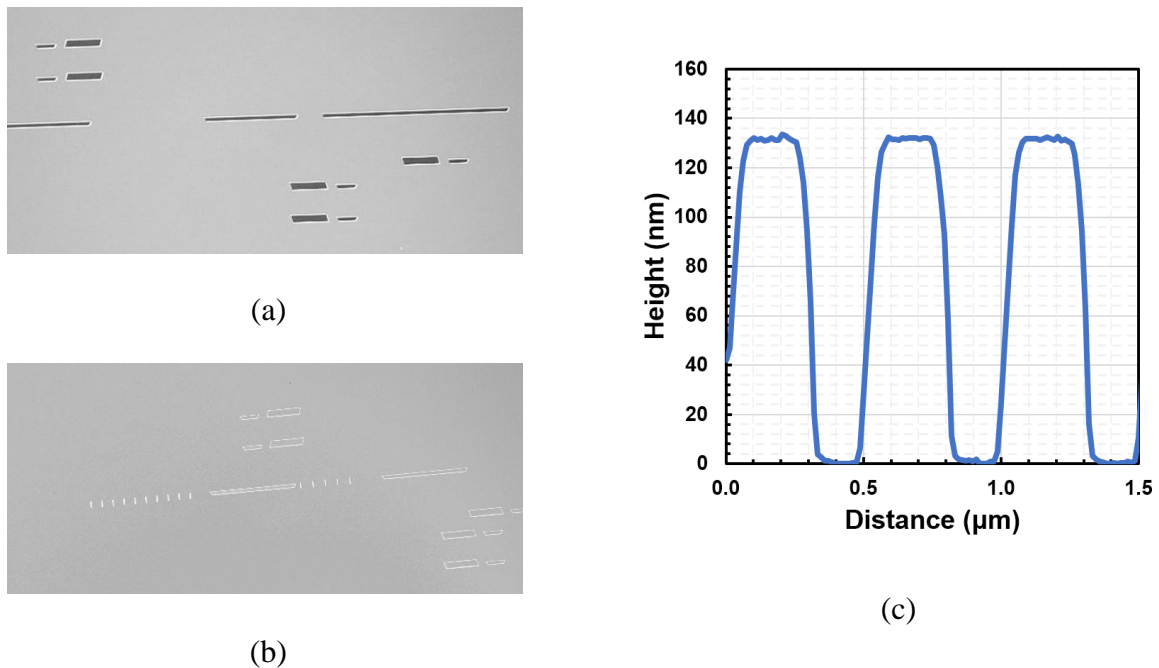


Figure 6 - 7 (a) Optical micrograph after the active regions were selectively removed from the wafer. (b) Optical micrograph after the gratings were dry etched. (c) Atomic force micrograph of the second order grating test structure. The etch depth is around 80 nm with a pitch of 500 nm and 40% duty cycle.

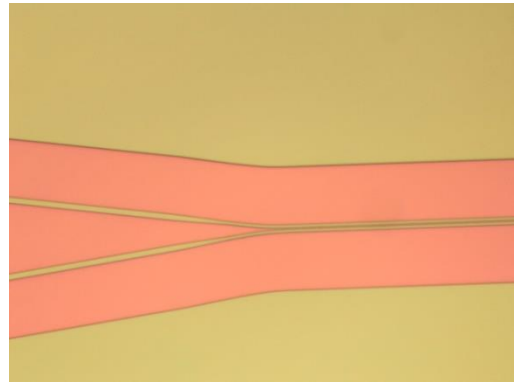
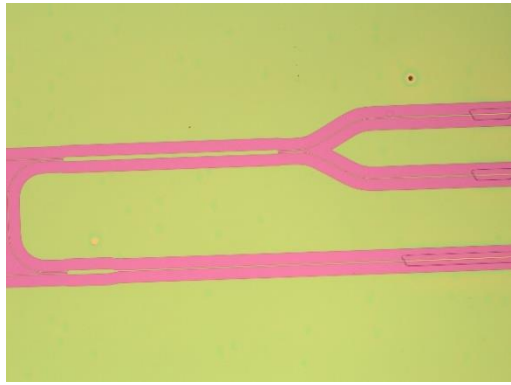
### ***Waveguide Definition***

After regrowth, the waveguide layers are patterned. Due to the presence of both surface and deep ridge waveguides, three lithography steps are required to define the circuit with various in-process steps shown in Figure 6 - 8. The first waveguide definition step is a dry etch of all the waveguide regions about 1 μm deep. The goal is to stop close to the InGaAsP waveguide layer, without etching into it. The second lithography step acts to mask the deep ridge waveguide sections. These sections contain waveguides that are not aligned along the  $110$  crystal plane and result in  $[111]$  facets forming and defects along the sidewalls as shown in Figure 4 – 19 [7], [8]. The regions that are aligned along the  $110$  crystal plane are wet etched

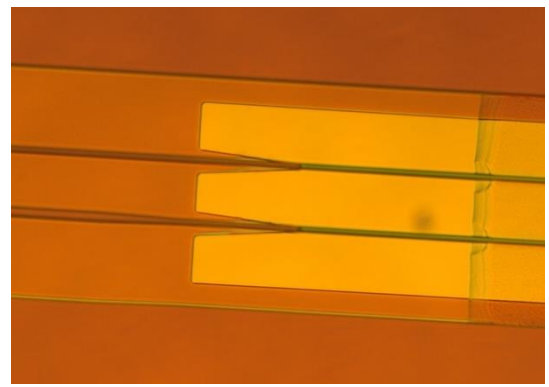
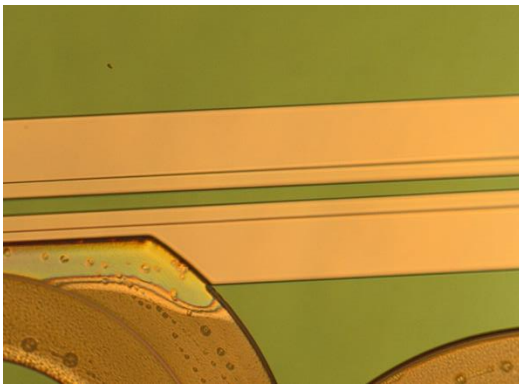
using HCl:H<sub>3</sub>PO<sub>4</sub> which stops abruptly on the InGaAsP waveguide layer and QW layers and gives smooth, low defect sidewalls. The third and final lithography step for waveguide definition is a lift off mask that covers the previously wet etched regions. SiO<sub>2</sub> is deposited using an electron beam evaporator and the photoresist is removed. This leaves behind a SiO<sub>2</sub> hard mask over the waveguide regions that are meant to remain surface ridge waveguides, while exposes the deep ridge section. This concept is more clearly shown in Figure 6 - 9 (Adapted from [9]). The deep ridge waveguide sections can then be etched using the RIE-2 or ICP-Unaxis tool [4], [6], [10], [11].

One issues that was commonly encountered in the waveguide definition step, was a partial etch of the InGaAs P-contact layer during the initial dry etch step. The sidewall roughness during the initial etch of the InP cap allows the subsequent wet etch step to undercut the SiN hard mask. This leads to degradation of the InGaAs P-contact as the processing continues as it is partially exposed as shown in Figure 6 - 10a. This can be overcome by using a spacer process. SiN is deposited by PECVD followed by a blanket etch in ICP-2. Due to the conformal nature of PECVD deposition and the highly direction nature of ICP-2 etching, the result is a layer of SiN on the sidewall of the waveguide as shown in Figure 6 - 10b. This serves to protect the InGaAs and InP cap layer.

A second issue encountered is a shadowing of the SiO<sub>2</sub> electron beam deposition by the surface ridge waveguide. Due to the slight off-centering of the sample during SiO<sub>2</sub> evaporation, one side of the surface ridge waveguide is shadowed making the deposition SiO<sub>2</sub> thinner than desired. The result is that during the etching of the deep ridge waveguides a small region adjacent to the surface ridge is etched causing additional passive loss as shown in

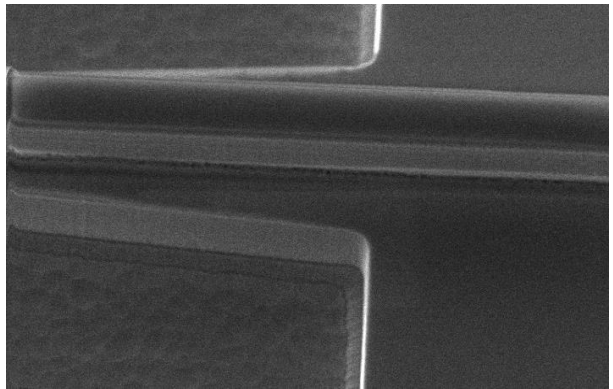
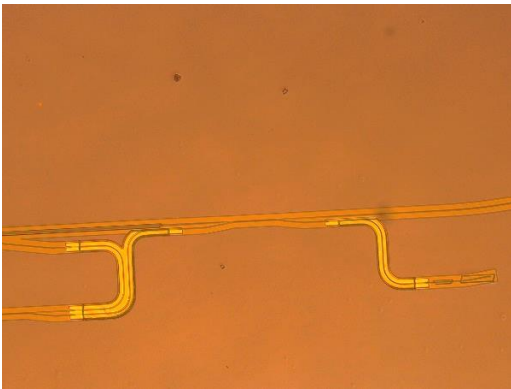


(a)



(b)

(c)



(d)

(e)

Figure 6 - 8 (a) Optical micrograph of the a-MZI and directional coupler section of the PIC following the initial waveguide (WG)-1 layer which consisted of a dry etch (b) Image of SOA following WG-2 wet etch process. (c) Image of the deep-to-shallow transition after exposure and development of the photoresist during the WG-3 process. (d) Image of waveguides shows the regions where the deep ridge waveguides are formed (curved section) (e) SEM of the the deep-to-shallow transition.

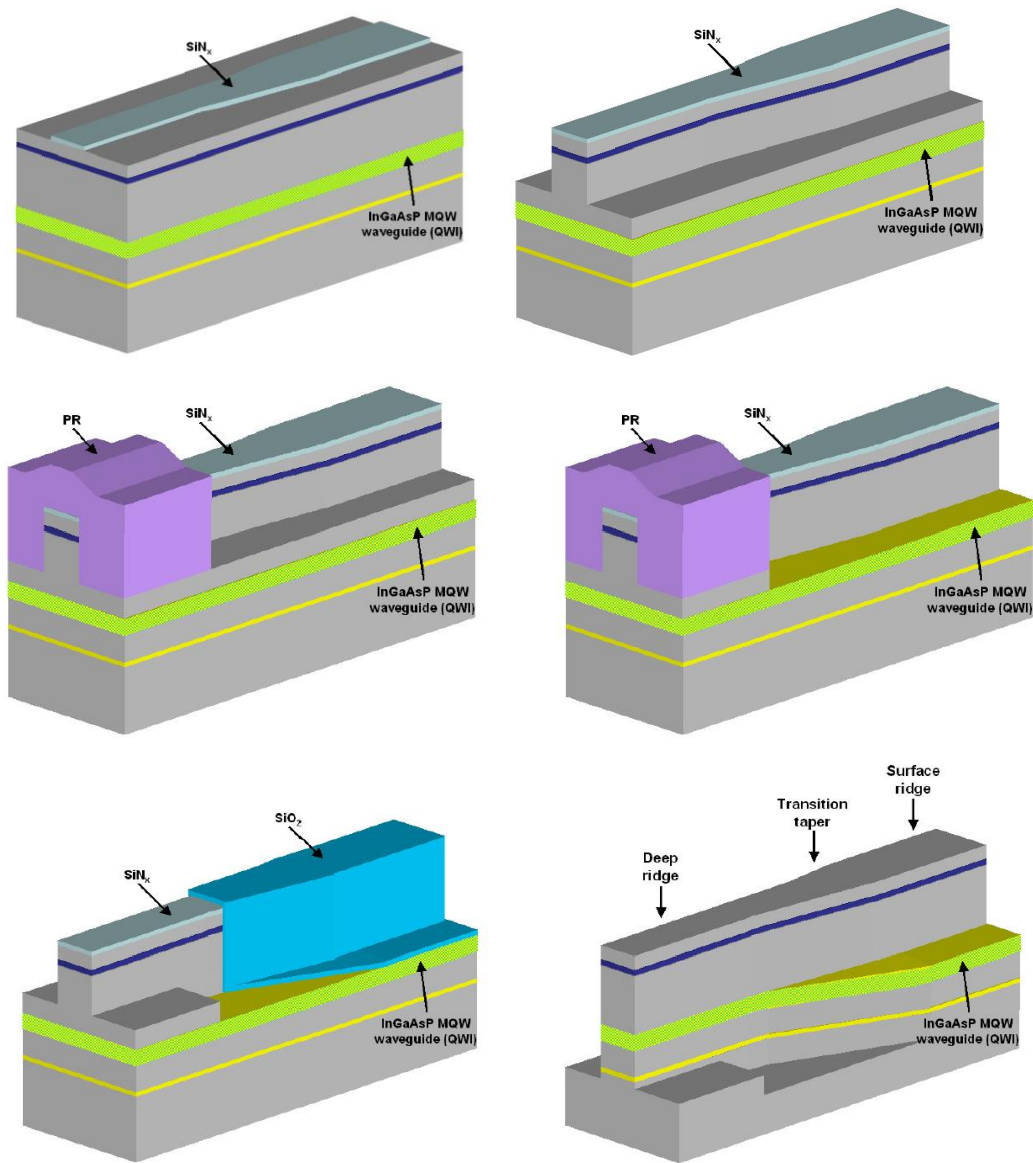
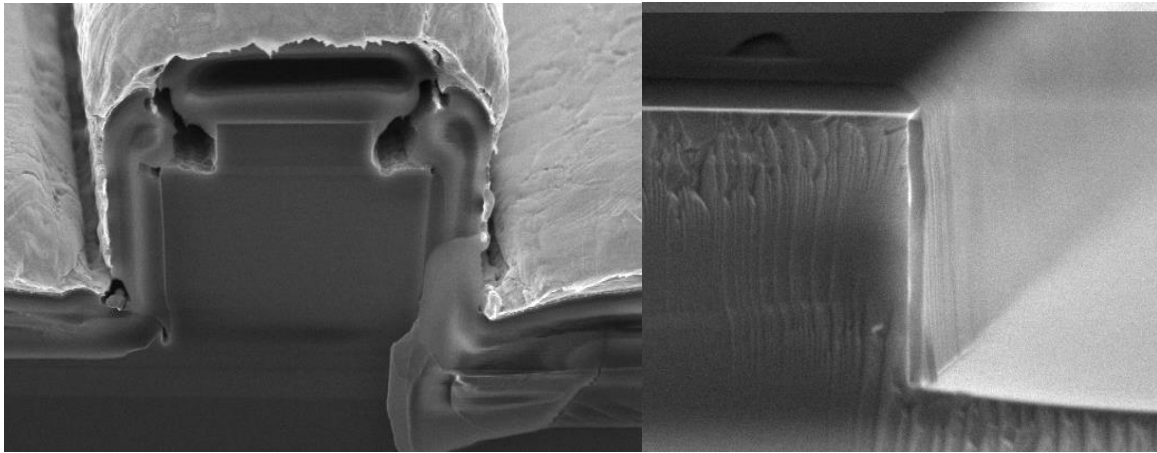


Figure 6 - 9 Diagram illustrating the process to create both the surface ridge and deep ridge waveguides using a three step lithography process and both wet and dry chemical etching. First a mask is put down for the entire PIC including both the deep and surface ridge waveguides (first panel). All sections are then dry etched using this mask to create the ridge (second panel). The regions that create the deep ridge waveguides are then covered in photoresist (third panel), a selective wet etch is used to etch the remaining InP and stop on the InGaAsP waveguide layer to create the surface ridge waveguide (fourth panel). SiO<sub>2</sub> is the deposited by E-beam evaporator, and lifted off to create the mark for the WG-3 layer (fifth panel). The deep ridge waveguides are then formed by dry etching the exposed regions (sixth panel). Figure adapted from Ref. [9]



(a)

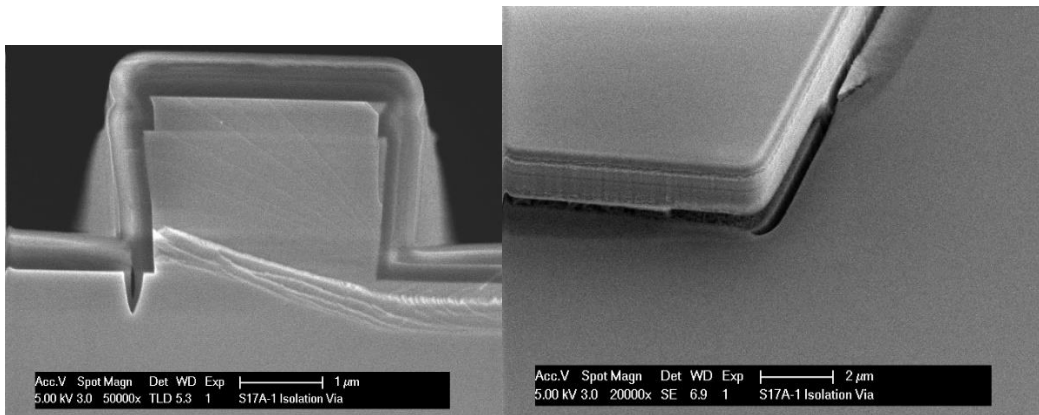
(b)

Figure 6 - 10 (a) SEM cross section of the surface ridge waveguide showing the degradation of the top InP cap and underlying InGaAs p-contact layer. (b) SEM of the spacer process in which dielectric ( $\text{SiO}_2$  or  $\text{SiN}$ ) is deposited by PECVD and then a timed blanket ICP etch (no mask layer) is completed to etch away to dielectric. Because the ICP etch is strongly anisotropic (primarily etching vertical), the dielectric is left on the side wall of ridges which protects the sidewalls of the ridge from subsequent process steps.

Figure 6 - 11. In the case of samples using directional couplers, this is also severely affected the coupling between the two waveguides and very little optical power was delivered to the receiver.

### ***Semi-Self-Align Process***

The next two steps in the fabrication process use a semi self-align (SSA) technique. In this technique, a standard lithography process is followed except the resist is under exposed and developed. This creates a depression in the exposed region but does not expose material underneath the photoresist. The sample is then etched in a  $\text{O}_2$  plasma for short periods of two



(a)

(b)

Figure 6 - 11 (a) SEM cross section of the surface ridge waveguide after the WG-3 dry etch process, showing section next to the ridge that was etched due to shadowing during the SiO<sub>2</sub> E-beam evaporation. It is believe this led to poor coupling between the directional coupler. (b) Second SEM showing this etched region from a plan view.

minutes to five minutes until only the top surface of the waveguide ridges are exposed. Figure 6 - 12 shows how a microscope can be used to tell if the top is exposed or has residual photoresist. The next step is to etch the dielectric mask to expose the underlying semiconductor. It is critical that the bottom parts of the ridge are not exposed during the semi-self-align process as this leads to large dark currents as a result of poor sidewall passivation and metal shorting the PN-junction. After exposing the underlying semiconductor, the desired layers are wet etched. For the first SSA step, the goal is to isolation the contacts between devices as best possible so both the InP and InGaAs layer are removed to eliminate the high conductivity path between each device. In the second SSA process, only the InP cap layer is removed, leaving the InGaAs layer for creating the p-contact.

A key challenge in implementing this process is the existence of significant topographical variation. The SSA process relies on the thickness of the photoresist being similar over the various regions that are trying to be opened. In the initial design of the PIC, deep holes were etched to the substrate for thermal management reasons. These deep holes led to variable photoresist thicknesses around the waveguides. As a result, contacts and isolation regions on different parts of the circuit were opened quickly while others did not fully open until the waveguide below the ridge had been opened in other parts as shown in Figure 6 - 12. This led to metal shorting the PN-junction and causing large leakage currents in devices. The solution to this was removal of the thermal pads and buffering the space around the SSA regions to create as uniform of photoresist across the circuit. Alternatively, the planarization process described above would likely alleviate this issue, however, it was not developed in time to be applied to this process.

### ***Pad Metal Deposition and PIC Singulation***

Deposition of the pad metal is the same as described for the UTC-PD with the exception that the metal stack is Ti/Pt/Au. The wafers are thinned using a mechanical lapping process and Ti/Pt/Au contacts are uniformly deposited on the back side of the wafer. Finally, individual PICs are cleaved from the wafer for testing. Figure 6 - 13 shows the completed PIC and the PIC mounted on the carrier with the electronic control circuits.

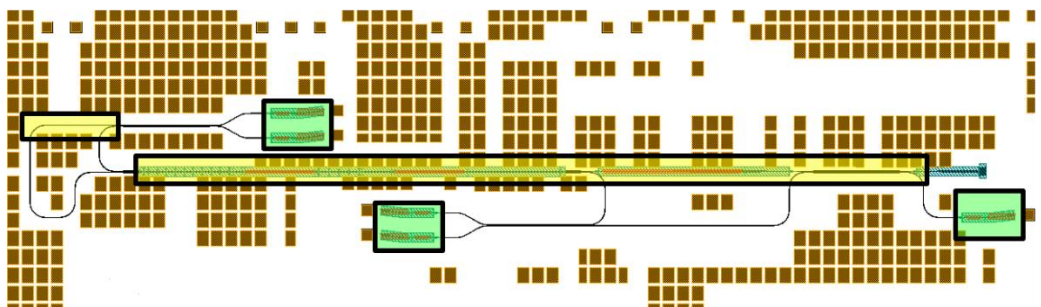
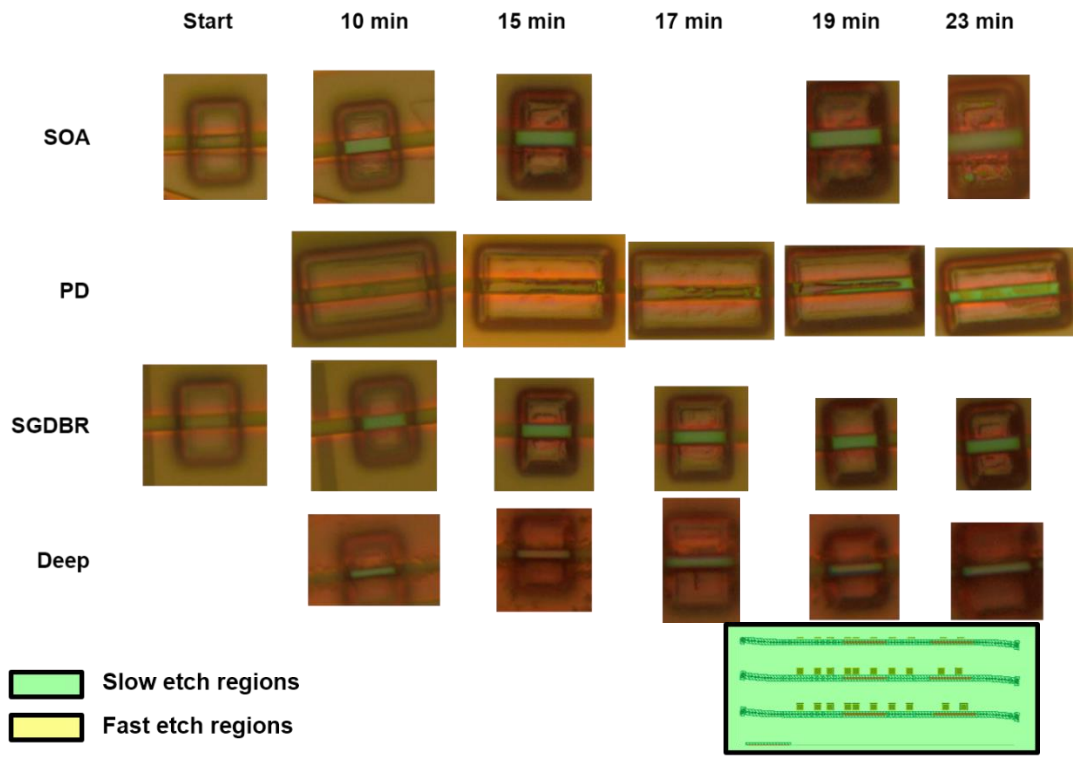


Figure 6 - 12 Tracking of the photoresist etch over various ridge sections as a function of time. As seen from the top section, the top of the SGDBR components, SOAs, and deep ridge section were exposed after about 10 minutes of O<sub>2</sub> plasma etching. The PDs took over 23 minutes of O<sub>2</sub> etching to completely expose the top of the ridges. At this point the photoresist by the other sections had been completely etched down to the waveguide layer, which would cause shorting of the PN junction if the P-contact metal had been deposited. By highlighting which regions had exposed after 10 minutes compared to 23 minutes, it was deduced that the thermal vias were causing the photoresist to be thinner over the fast etch regions. By removing the thermal vias, the process was reproducible over the entire PIC.

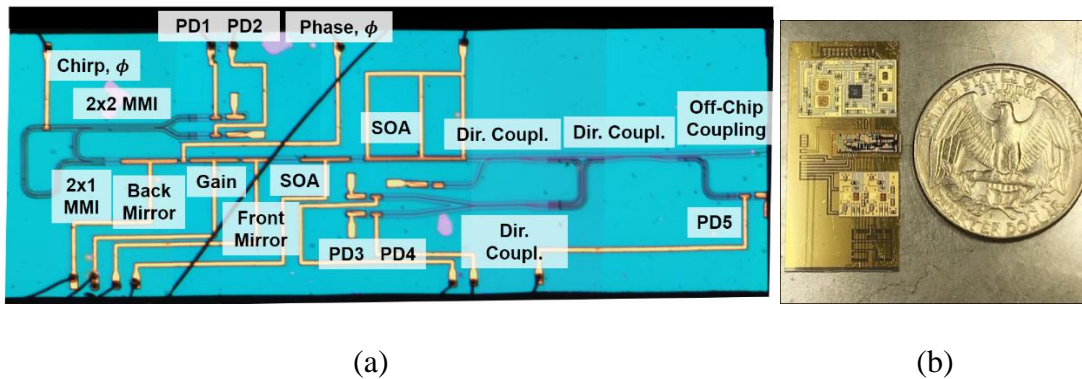


Figure 6 - 13 (a) Optical image showing the completed PIC and the components. (b) optical image of the PIC on the carrier with the receiver and locking circuit board with a quarter for scale.

## References

- [1] A. Sivananthan, "Integrated Linewidth Reduction of Rapidly Tunable Semiconductor Lasers," 2013.
- [2] V. Jayaraman, Z. M. Chuang, and L. A. Coldren, "Theory, Design, and Performance of Extended Tuning Range Semiconductor Lasers with Sampled Gratings," *IEEE J. Quantum Electron.*, vol. 29, no. 6, pp. 1824–1834, 1993.
- [3] M. Tacano, K. Oigawa, and S. Uekusa, "Preferential etching of InP for submicron fabrication with HCl/H<sub>3</sub>PO<sub>4</sub> solution," *J. Electrochem. Soc.*, vol. 132, no. 3, pp. 671–673, 1985.
- [4] L. A. Coldren, K. Furuya, B. I. Miller, and J. A. Rentschler, "Combined dry and wet etching techniques to form planar (011) facets in GaInAsP/InP double heterostructures," *Electron. Lett.*, vol. 18, no. 5, pp. 235–237, 1982.
- [5] J. E. Schramm, "Highly selective reactive ion etch process for InP-based device fabrication using methane/hydrogen/argon," *J. Vac. Sci. Technol. B Microelectron. Nanom. Struct.*, vol. 11, no. 6, p. 2280, 1993.
- [6] J. E. Schramm, D. I. Babic, E. L. Hu, J. E. Bowers, and J. L. Merz, "Anisotropy control in the reactive ion etching of InP using oxygen in methane/hydrogen/argon," *Conf. Proc. - Int. Conf. Indium Phosphide Relat. Mater.*, pp. 383–386, 1994.

- [7] J. A. Summers, “Monolithic Multi-Stage Wavelength Converters for Wavelength-Agile Photonic Integration,” University of California Santa Barbara, 2007.
- [8] S. Adachi and H. Kawaguchi, “Chemical Etching Characteristics of (001)InP,” *J. Electrochem. Soc.*, vol. 128, no. 6, pp. 1342–1349, 1981.
- [9] J. Klamkin, “Coherent Integrated Receiver for Highly Linear Microwave Photonic Links,” University of California Santa Barbara, 2008.
- [10] J. S. Parker, E. J. Norberg, R. S. Guzzon, S. C. Nicholes, and L. A. Coldren, “High verticality InP/InGaAsP etching in Cl<sub>2</sub>/H<sub>2</sub>/Ar inductively coupled plasma for photonic integrated circuits,” *J. Vac. Sci. Technol. B, Nanotechnol. Microelectron. Mater. Process. Meas. Phenom.*, vol. 29, no. 1, p. 011016, 2011.
- [11] F. Karouta, B. Docter, A. A. M. Kok, E. J. Geluk, J. J. G. M. van der Tol, and M. K. Smit, “High aspect ratio etching and application in InP-based photonic integrated circuits,” in *Electrochemical Society*, 2007, vol. 24, no. 1, p. 2006.

# Chapter 7

## Experimental Results on Transceiver PIC for LIDAR

Characterization of the transceiver PIC consisted of the following: Current-Voltage measurements on the all diodes, Light-Current-Voltage (LIV) measurements of gain section using reverse biased SOA and PDs to measure optical power, SGDBR spectrum mapping using the front and back mirrors, LI measurements of the discriminator PDs as the phase and chirp sections are tuned, and frequency chirp control. In the following sections, results from the SGDBR laser are shown, followed by demonstration of the frequency and filter tuning effects on the output of the a-MZI, and finally the receiver characterization.

### SGDBR Laser Performance

Characterization of the SGDBR laser amounts to measuring the light output and voltage drop as the current is increased, measuring the wavelength tuning as current is injected into the phase section, and wavelength mapping as current is injected into the front and back mirrors. The measured light-current-voltage (LIV) of the SGDBR laser is shown in Figure 7 - 1a demonstrating a threshold current around 45 mA. The laser output achieves around 15 mW at 100 mA current injection. Tuning the current in the phase section of the SGDBR laser at fixed mirror and gain regions current tunes the laser wavelength over a range of 0.3 nm or 24 GHz

as shown in Figure 7 - 1b. Tuning the front and back mirror by sweeping the current injection from 0 mA to 20 and 25 mA respectively generates the tuning map in Figure 7 - 2b with 40 nm of available tuning. Figure 7 - 2a shows discrete points of wavelength tuning from 1530 nm to 1570 nm and demonstrates that side mode suppression ratio greater than 37 dB is achieved over the tuning range. In practice, the tuning map provides a look-up table to tune the laser frequency and sample a discrete set of angular point using an OPA for the desired FMCW application. The output during the transient stabilization can be suppressed by reducing the gain of the on-chip SOAs. Identical SGDBR lasers have been characterized by our group showing free-running linewidths of 6 MHz [1].

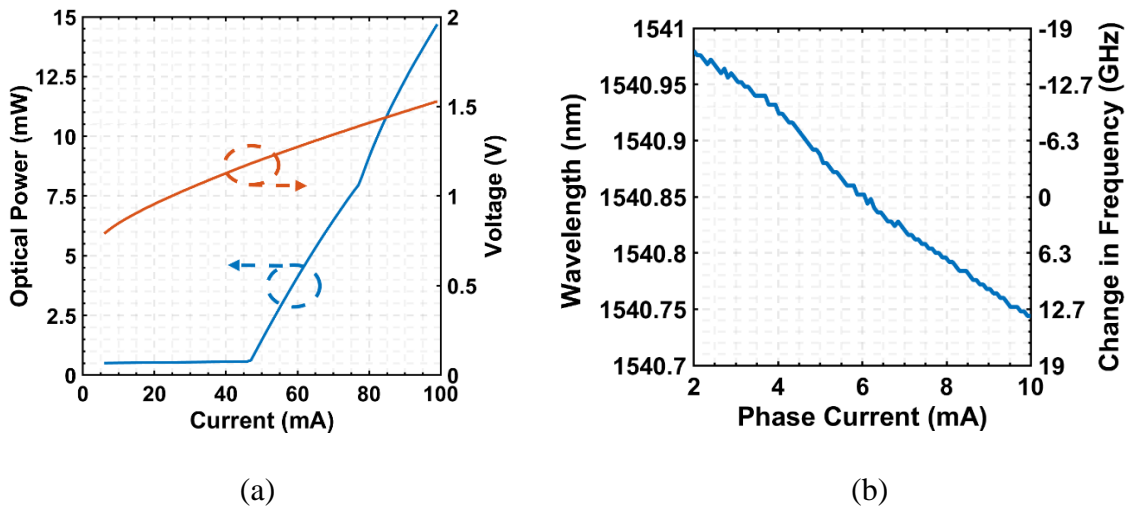


Figure 7 - 1 (a) Light current voltage measurement of SGDBR laser demonstrating threshold current of ~45 mA and output power of 15 mW at 100 mA. The phase and mirror pads are floating. (b) Lasing frequency tuning as a function of current injection into the phase section demonstrating ~30 GHz (0.25 nm) of tuning over 10 mA.

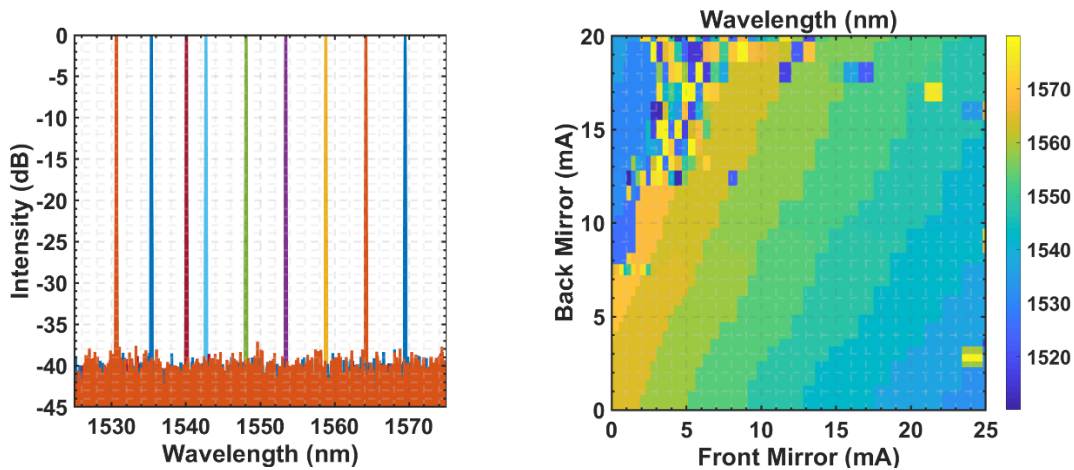


Figure 7 - 2 (a) Course frequency tuning of the SGDBR laser over 40 nm by tuning the front and back mirror currents. The gain section is biased to 100 mA, the phase section is floating, and the SOAs are biased to around 10 mA to minimize reflections from the chip facet back to the laser cavity (see appendix A for additional details). (b) Tuning map of the SGDBR laser under the same conditions as in (a).

## Frequency Discriminator Response

Characterization of the frequency discriminator consists of first determining the power reaching the PDs, then tuning the lasing wavelength by using the phase shifter in the SGDBR cavity, followed by tuning of the filter spectral location using the chirp section in the a-MZI. The photocurrent detected by the discriminator PDs was measured alongside the SOA photocurrent as shown in Figure 7 - 3a. The SOA measures the power from the front mirror, while the two discriminator PDs measure the power from the back mirror. As mentioned above, a front to back splitting ratio of 7:1 was expected from the front and back mirror designs. However, lower power was detected at the discriminator PDs, which we attribute to passive optical loss in the deep ridge waveguide of the a-MZI. The photocurrent in each detector as a function of phase current is shown in Figure 7 - 3b. Current injection into the

phase section of the SGDBR provides fine tuning of the laser frequency, which is measured on an Optical Spectrum Analyzer and shown on the top x-axis of Figure 7 - 3b. As discussed in Section II, the a-MZI was designed to have an FSR of 60 GHz. Figure 7 - 3b shows that the filter passes through half of a cycle in 30 GHz of frequency tuning. Lastly, the filter quadrature location is tuned using the chirp section in the a-MZI as shown in Figure 7 - 3c.

The external locking circuits operates by injecting current into the phase section of the SGDBR such that the lasing frequency is located at the quadrature point of the a-MZI and equal power is distributed to the two PDs. By tuning the current injected into the chirp section, the quadrature frequency is changed, and the output of the feedback circuit changes to maintain the locking condition. Figure 7 - 3d shows the offset lasing frequency tuning over 30 GHz as the chirp phase shifter current is tuned between 0 mA to 10 mA. By imparting a triangular waveform with a current modulation range of 10 mA, the frequency of the laser can be modulated continuously over 30 GHz with a tuning efficiency of 3 GHz/mA.

## **Receiver**

The receiver consists of two PDs and a 2x2 MMI. One input consists of the reference signal from the SGDBR laser and the second is the echo signal. Figure 7 - 4 shows the measured photocurrent in each PD as the phase section of the SGDBR laser is tuned with no intentional reflection. With an intentional reflection present, this would undergo a similar beating response as seen in Figure 7 - 3b. As shown in Figure 7 - 4, the reference signal provides greater than 1 mW of input power into the receiver. This falls into the regime of shot noise limited operation making the minimum detectable echo signal power around 1 nW [2].

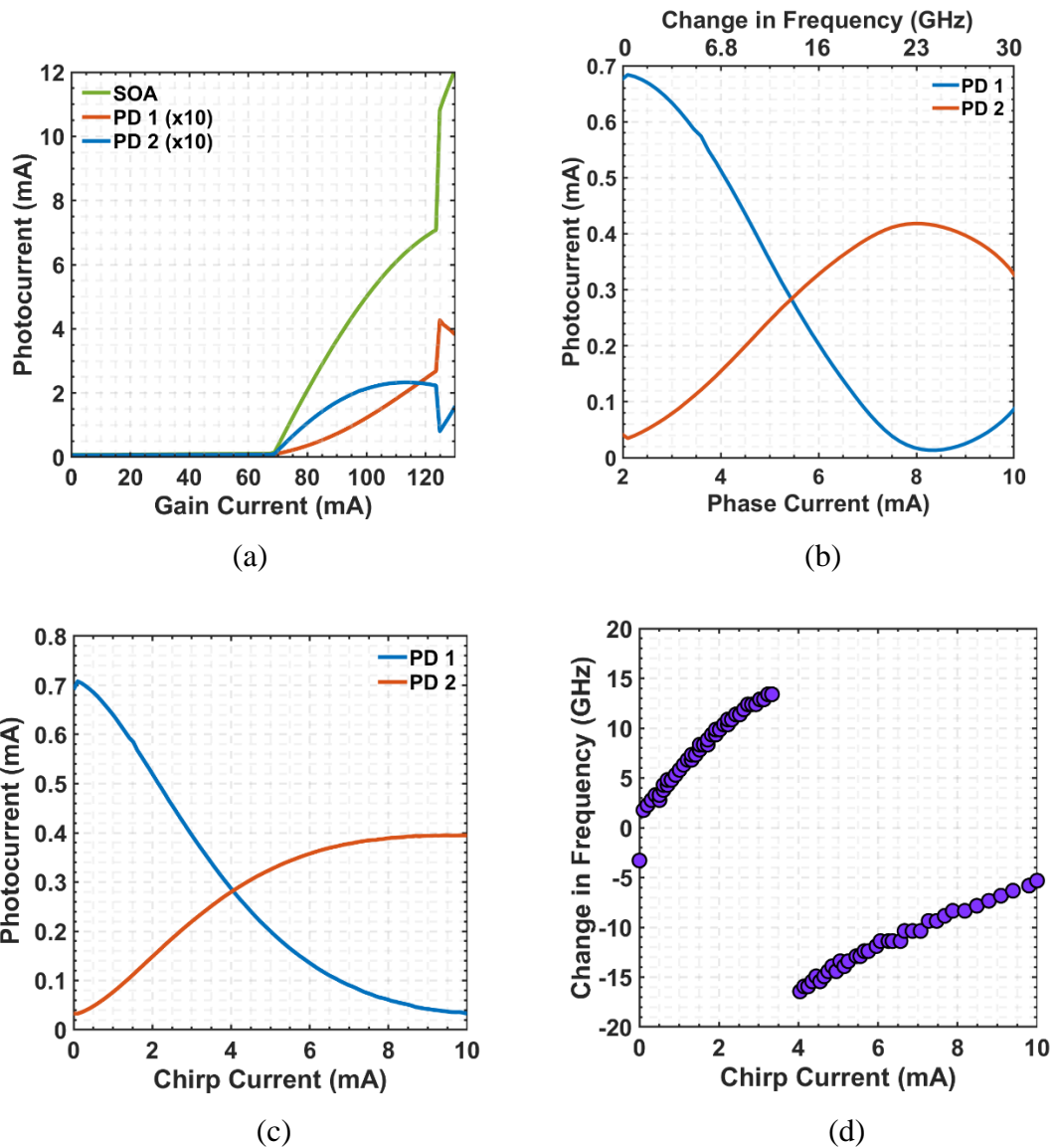


Figure 7 - 3 (a) Reponse of the PDs at the output of the A-MZI and SOA after the front mirror the SGDBR laser as the gain current is swept. The front to back power splitting ratio is found from this measurement to be around 20, due to larger than expected passive waveguide loss in the deep ridge waveguides. (b) Reponse of the A-MZI PDs are current is injected into the phase section. This in turn tunes the frequency of the laser as shown on the top x-axis. The phase current vs frequency of the laser is taken from Fig. 7.1. (c) Response of the A-MZI PDs are current is injected into the chirp section of the A-MZI. This effectively tunes the length imbalance of the A-MZI, which in turn changes the null point in the output PDs. (d) Locking frequency vs. chirp current. At a given chirp current, and SGDBR configuration (gain, front and back mirror currents fixed) the feedback circuit will pull the current injected into the phase section such that the PD currents are balanced. This fixes the frequency of the laser.

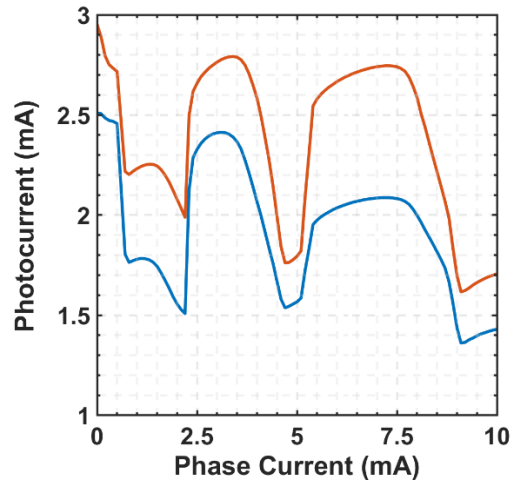


Figure 7 - 4 Response of the PD at the output of the receiver as the phase current (laser output frequency) is changed. The large hops are due to mode hops of the laser. The large common mode current is likely due to the large reference power relative to the small unintentional reflection from the chip facet.

## Conclusion

A PIC transceiver consisting of an SGDBR laser with an on-chip frequency discriminator for frequency locking and modulation for LiDAR applications was demonstrated. The components of the PIC were characterized to demonstrate functionality and the operating principles of the transceiver.

## References

- [1] H. Zhao *et al.*, “Indium Phosphide Photonic Integrated Circuits for Free Space Optical Links,” *IEEE J. Sel. Top. Quantum Electron.*, vol. 24, no. 6, pp. 1–6, 2018.
- [2] K. Kikuchi and S. Tsukamoto, “Evaluation of sensitivity of the digital coherent receiver,” *J. Light. Technol.*, vol. 26, no. 13, pp. 1817–1822, 2008.

# Chapter 8

## Conclusion and Future Works

In this work, high-speed photodiodes were designed and fabricated with the goal of making an ultra-wideband optical-to-electrical converter for the mmW generation for next generation free space communication and mobile networks. A waveguide design was chosen to enable additional design freedom compared to surface illuminated devices. Furthermore, with the goal of OBFNs in mind, the waveguide UTC-PD was integrated with a spot size converter for more efficient optical coupling to PLC platforms, in particular the Triplex platform from Lionix, and fiber [1]. In addition to this, a compact PIC transceiver that integrates a frequency locked widely tunable semiconductor diode laser and coherent detector was fabricated and characterized demonstrating the potential for free space sensing and LIDAR. The PIC integrated multiple PDs, SOAs, phase shifters, an SGDBR laser, and passive elements such as MZIs, directional couplers, and MMI couplers [2].

### **Waveguide Uni-Traveling-Carrier Photodiode**

#### ***Summary of Accomplishments***

The photodiodes in this work were designed using Lumerical optical and electrical simulation packages MODE, DEVICE, and FDTD. In the design process, the absorber and

depletion region were optimized for high transit time limited bandwidth by accounting for the nonlinear transit velocity of electrons in InP and InGaAs. A doping grade was included to increase the transit velocity, results in a transit time limited bandwidth over 300 GHz according to simulations. Furthermore, the InGaAs and InP interface between the depletion region and absorber were graded to eliminate interfacial discontinuity in the band alignments which can lead to additional virtual parasitic capacitance effects [3]. Furthermore, the modified UTC variant was employed to increase the electric field adjacent the absorber to increase maximum achievable RF output power [4]. The optical simulations performed illustrated that by tapering the waveguide, the optical absorption profile, and the resulting photogenerated carrier density, could be engineered to minimize the peak carrier density, which also helps to increase the maximum RF output power attainable. For ridge widths between 0.6  $\mu\text{m}$  and 2  $\mu\text{m}$  the mode overlap with the absorbing region can be increased from less than 1% to around 16%. From this, the mask layout included multiple geometries including ridge width from 1  $\mu\text{m}$  to 3  $\mu\text{m}$  and various taper lengths.

The fabrication of these devices required process development and optimization to enable high resolution i-line lithography on high aspect ratio surface topographies. The developed process used PMGI series as a reflow layer which reduced the surface topography seen by the high-resolution photoresists typically used in the i-line stepper at UCSB. This developed process can also benefit the semi self-align process used for laser and PIC processing to make p-contacts to regrown ridges.

The successful fabrication of the waveguide UTC-PDs was completed by eliminating the regrowth and hence some of the surface topography that led to challenging lithography. The

epi design was verified to demonstrate greater than 67 GHz bandwidth after completing the fabrication without the spot size converter. The sacrifice due to this, is the responsivity was a strong function of the distance of the cleave location from the start of the active mesa. By completing the fabrication with the spot size converter, the sensitivity of the responsivity was reduced. These devices also demonstrated up to 60 GHz bandwidth. Furthermore, the devices demonstrated up to 6 dBm of RF output power at 8 GHz [5].

In addition to designing, fabricating, and characterizing high speed photodiodes, the limitations to the power conversion efficiency was explored using a simple model. By collecting data from the literature, a strong dependence on operating frequency was found, with higher frequencies having lower power conversion efficiency. One device was characterized to understand the limiting component to the power conversion efficiency but measure the relative RF response as a function of the bias and average photocurrent. A high effective resistance was found which limited the power conversion efficiency to around 4% [6].

### ***Future Works***

The integration of the photodiode with a spot size converter enables coupling to other PIC platforms for various microwave photonic applications. In particular, Yuan Liu demonstrated a SiN based OBFN with both true time delay based on optical ring resonators and switched delay lines. By using an interposer and flip chip bonding, these two optimized photonic platforms can be hybrid integrated to create an optically driven phased array antenna for next generation mobile communication links at frequencies up to 100 GHz.

Simultaneously, efforts to integrate these devices with broadband antennas in the W-band can be pursued. The challenge of integrating W-band antennas on semiconductor photonics technologies stems from the wavelength at W-band being comparable to the device bar length, width, and substrate thickness. The result is radiation patterns are sensitive to fabrication variability and small changes in the geometry. Nevertheless, combining an OBFN PIC with an array of high-speed photodiodes and planar antennas would be a major technical achievement in microwave photonics.

Finally, it was demonstrated that the space charge resistance is a limiting factor in the performance of high-speed photodiodes for mmW generation, particularly with regard to efficiency. One benefit of the waveguide approach is the ability to engineer the absorption profile to minimize the peak photocurrent which causes the high space charge impedance. A useful study would correlate simulated absorption profiles with measured space charge impedance.

## **InP PIC Transceiver.**

### ***Summary of Accomplishments***

The PIC transceiver in this work followed up on work done previously in the group on frequency locked lasers for free space optical communication and sensing. By integrating a control knob to chirp the filter and hence the laser frequency, the transmit portion of the PIC enable simultaneous frequency modulation and frequency locking for FMCW LIDAR. Furthermore, the PIC integrating the transmitter with coherent balanced receiver completing the transceiver components necessary for a compact transmitter to enable optical phased array

based FMCW LIDAR. The fabricated PIC demonstrated wavelength tuning over 40 nm with greater than 37 dB side mode suppression. The filter tuning was demonstrated along with fine tuning on the lasing frequency to allow for 2 GHz/mA tuning efficiency.

### ***Future Works***

While the components of the transceiver PIC were demonstrated, frequency locking and chirping of the laser frequency was not demonstrated due to control circuit issues. Future work to demonstrate the simultaneous reduction in laser linewidth with frequency modulation is in progress. Following this demonstration, the PIC can be fiber coupler to a directional coupler with the two outputs of the directional coupler connected directly or with a fiber delay line in the path. This sets up a perfect reflector, to enable measurements of the RF beat node produced by reflections at various distances from the receiver.

Following the demonstration of 1D ranging measurements, the PIC can be either butt coupled or flip chip bonded with a total internal reflection turning to a 2D optical phased array. The system can then be used for full 3D mapping of simple retroreflector setups.

### **References**

- [1] C. G. H. Roeloffzen *et al.*, “Silicon nitride microwave photonic circuits,” *Opt. Express*, vol. 21, no. 19, pp. 22937–22961, 2013.
- [2] B. J. Isaac, B. Song, S. Pinna, L. A. Coldren, and J. Klamkin, “Indium Phosphide Photonic Integrated Circuit Transceiver for FMCW LiDAR,” *IEEE J. Sel. Top. Quantum Electron.*, vol. 25, no. 6, 2019.
- [3] M. Natrella *et al.*, “Accurate equivalent circuit model for millimetre-wave UTC

- photodiodes,” *Opt. Express*, vol. 24, no. 5, p. 4698, 2016.
- [4] M. Chtioui *et al.*, “High responsivity and high power UTC and MUTC GaInAs-InP photodiodes,” *IEEE Photonics Technol. Lett.*, vol. 24, no. 4, pp. 318–320, 2012.
- [5] B. Isaac, S. Pinna, Y. Liu, and J. Klamkin, “Efficiency of Waveguide Uni-Traveling-Carrier Photodiodes for Microwave Signal Generation,” in *2019 Optical Fiber Communications Conference and Exhibition, OFC 2019 - Proceedings*, 2019.
- [6] B. Isaac, Y. Liu, S. Pinna, and J. Klamkin, “Limitations to Power Conversion Efficiency of InP Based Uni-traveling-carrier Photodiodes Due to Space Charge Resistance,” in *2019 Compound Semiconductor Week, CSW 2019 - Proceedings*, 2019.